

Atomistic Simulations of Nickel-Titanium Shape-Memory Alloys

Srinivasan, Prashanth

DOI

[10.4233/uuid:2f6f7731-fdb3-4a90-b1ba-5d275b1979d3](https://doi.org/10.4233/uuid:2f6f7731-fdb3-4a90-b1ba-5d275b1979d3)

Publication date

2020

Document Version

Final published version

Citation (APA)

Srinivasan, P. (2020). *Atomistic Simulations of Nickel-Titanium Shape-Memory Alloys*. [Dissertation (TU Delft), Delft University of Technology]. <https://doi.org/10.4233/uuid:2f6f7731-fdb3-4a90-b1ba-5d275b1979d3>

Important note

To cite this publication, please use the final published version (if applicable). Please check the document version above.

Copyright

Other than for strictly personal use, it is not permitted to download, forward or distribute the text or part of it, without the consent of the author(s) and/or copyright holder(s), unless the work is under an open content license such as Creative Commons.

Takedown policy

Please contact us and provide details if you believe this document breaches copyrights. We will remove access to the work immediately and investigate your claim.

**ATOMISTIC SIMULATIONS OF
NICKEL-TITANIUM SHAPE-MEMORY ALLOYS**

ATOMISTIC SIMULATIONS OF NICKEL-TITANIUM SHAPE-MEMORY ALLOYS

Proefschrift

ter verkrijging van de graad van doctor
aan de Technische Universiteit Delft,
op gezag van de Rector Magnificus prof. dr. ir. T.H.J.J. van der Hagen,
voorzitter van het College voor Promoties,
in het openbaar te verdedigen op
donderdag 5 maart 2020 om 12:30 uur

door

Prashanth SRINIVASAN

Master of Technology in Civil Engineering and Applied Mechanics,
Indian Institute of Technology Madras, India
geboren te Chennai, India.

This dissertation has been approved by the promotor.

Composition of the doctoral committee:

Rector Magnificus,	chairperson
Prof. dr. ir. L. J. Sluys	Delft University of Technology, promotor
Prof. dr. ir. L. Nicola	Delft University of Technology, promotor
Prof. dr. ir. A. Simone	University of Padova, Italy, promotor

Independent members:

Prof. dr. B. Grabowski	University of Stuttgart, Germany
Prof. dr. M. J. Santofimia Navarro	Delft University of Technology
Prof. dr. ir. T. J. H. Vlugt	Delft University of Technology
Dr. M. Amirthalingam	Indian Institute of Technology Madras, India



Keywords: shape memory alloys, molecular dynamics, interatomic potential fitting, martensitic transformation.

Printed by: Ipskamp Printing

Cover: An OVITO image of a martensitic structure colored according to a local order parameter. Color code: red and blue - different variants of martensite; green - untransformed austenite.

Copyright © 2020 by P. Srinivasan.

ISBN 978-94-6384-106-1

An electronic version of this dissertation is available at
<http://repository.tudelft.nl/>.

To Amma and Appa

CONTENTS

Summary	xi
Samenvatting	xiii
1 Introduction	1
1.1 General Introduction.	2
1.2 Objective and Outline of the Thesis.	4
References	7
2 Modeling Pseudo-elasticity: MEAM vs EAM	9
2.1 Introduction	10
2.2 Method	11
2.3 Results.	14
2.4 Lattice Deformation Model	18
2.5 Concluding remarks	20
References	26
3 Orientation-dependent Pseudo-elasticity	29
3.1 Introduction	30
3.2 Methodology	31
3.3 Results.	33
3.3.1 Loading in $\langle 110 \rangle$ -direction	33
3.3.2 Loading in $\langle 111 \rangle$ -direction	38
3.3.3 Loading in $\langle 100 \rangle$ -direction	41
3.3.4 Discussion	42
3.3.5 Validation of MD results	45
3.3.6 Effect of temperature.	47
3.4 Nano-wires under bending	48
3.5 Conclusions.	52
References	54

4	A new Potential for Nickel-Titanium	59
4.1	Introduction	60
4.2	Methodology	62
4.2.1	The RF-MEAM potential	62
4.2.2	Fitting methodology including stress tensors	63
4.3	A new RF-MEAM for NiTi	64
4.3.1	Constructing the DFT database	64
4.3.2	Optimization of the RF-MEAM parameters.	65
4.3.3	Performance of the RF-MEAM potential	65
4.4	A RF-MEAM potential for the NbMoTaW high-entropy alloy	71
4.5	Concluding remarks	73
	Appendix	74
4.A	Using RF-MEAM in LAMMPS	74
4.A.1	Improvements to <i>MEAMfit</i>	74
4.A.2	LAMMPS implementation of the RF-MEAM potential.	74
4.B	Benefits of stress tensor fitting: Example using B2 NiTi	74
4.C	NiTi RF-MEAM potential parameters	79
	References	81
5	Influence of Defects on Phase Transformation	85
5.1	Introduction	86
5.2	Modeling details	88
5.3	Results and Discussion.	89
5.3.1	Transformation in perfect NiTi	89
5.3.2	Influence of anti-site defects.	90
5.3.3	Influence of Ni content.	91
5.3.4	Influence of vacancies	94
5.3.5	Simulating bi-crystal behavior.	96
5.3.6	Transformation in cylindrical NiTi nano-wires	98
5.4	Conclusion	100
	References	102
6	Conclusions	105
6.1	Outlook	108
	Acknowledgements	111
	Curriculum Vitæ	113

List of Publications

115

SUMMARY

Shape-memory Alloys (SMAs) exhibit tremendous mechanical properties owing to their reversible phase transformation between the austenitic and the martensitic phase. Out of these, equi-atomic nickel-titanium (NiTi) alloys are the most widely used SMAs for various applications since the transformation occurs close to room temperature. Advances in SMA engineering can be propelled by understanding the fundamental behavior of these materials. Atomistic scale computational techniques provide an efficient way of doing this. The accuracy of such techniques is based on the underlying model that is used in these simulations. With advancements in computational power, the scope for building more accurate material models and simulating bigger and more realistic systems have increased. This thesis is focused on understanding NiTi behavior at an atomistic scale using such accurate models. The work done as a part of this thesis is two-fold. Firstly, previously existing interatomic potential models are used to perform molecular dynamics (MD) simulations to describe various phase transformation phenomena in NiTi SMAs including pseudo-elasticity and shape-memory effect, thereby comparing the performance of these existing models. Secondly, a new NiTi interatomic potential is developed, using a database generated by performing Density Functional Theory (DFT) calculations, the performance of which is better than existing models.

In **Chapter 2**, a comparison of two existing interatomic potentials, the embedded-atom method (EAM) and the second nearest neighbor modified embedded-atom method (2NN-MEAM) potential, is made by performing MD simulations of uniaxial tensile and compressive loading of a single crystal NiTi along a particular orientation. It is observed that, although the EAM predicts a phase transformation, the transformation strains and the Young's modulus of the two phases are inaccurately estimated. The same simulations, when performed with a 2NN-MEAM potential, yield more accurate results in comparison to experimental and theoretical values. The results indicate the superior performance and predictive capabilities of the 2NN-MEAM, thereby validating its usage for further calculations.

The 2NN-MEAM is then used to analyze orientation-dependent behavior in these NiTi alloys. In particular, **Chapter 3** discusses the orientation-dependent

pseudo-elasticity in single crystals. Three different initial orientations are chosen and uniaxial loading is applied to model the martensitic transformation in these single crystals. Given the predictive capacity of the 2NN-MEAM, it captures accurate transformation strains in comparison to *ab initio* calculations. The MD simulations also reveal differences in the martensitic transformation mechanism along different orientations.

Although the 2NN-MEAM outperforms earlier potentials and can capture transformation strains along multiple orientations, some of the elastic constants of the martensitic phase and the transformation temperatures are still incorrectly predicted in comparison to *ab initio* and experimental values. Keeping this in mind, a new reference-free form of the MEAM potential (RF-MEAM) is developed and optimized for NiTi as described in **Chapter 4**. *Ab initio* MD runs are performed for both the austenitic and martensitic phase at different temperatures to generate configurations for the fitting of the RF-MEAM potential. Stress tensors of various configurations are also added to the fitting set, in addition to the energies and atomic forces. The new potential predicts elastic constants and the transformation temperatures more accurately than existing interatomic models, making it more suitable for performing MD simulations on generic NiTi systems.

Chapter 5 demonstrates the predictive power of the RF-MEAM potential. Although the fitting database during the optimization consisted only of equiatomic defect-free configurations, the potential captures the effect of various defects on the phase transformation in single-crystal NiTi as well. Presence of point defects reduces the austenitic transformation temperature drastically, getting it further close to experimentally known values. Grain boundaries and free surfaces in NiTi systems act as a nucleation site for the austenitic transformation, thereby reducing the forward transformation temperature.

To summarize, the interatomic potential is the most critical part of any MD simulation. The validity of the potential for a particular application needs to be verified before drawing conclusions based on the MD results. Here, this is demonstrated for the NiTi SMA, and the reader is given a newly developed potential that can be used to generate results for fine-tuning the engineering of NiTi devices for various applications.

SAMENVATTING

Geheugenmetalen (GM) vertonen geweldige mechanische eigenschappen die te danken zijn aan hun omkeerbare fase-transformatie tussen de austenitische en martensitische fasen. Van deze legeringen zijn nikkel-titaan (NiTi) legeringen met evenveel Ni als Ti de meest gebruikte GM voor verschillende toepassingen aangezien de transformatie dicht bij kamertemperatuur plaats vindt. Vooruitgang in GM kan worden bewerkstelligd door begrip van het fundamentele gedrag van deze materialen. Rekentechnieken op atomistische schaal bieden een efficiënte manier om dit te doen. De nauwkeurigheid van dergelijke technieken is gebaseerd op het onderliggende model dat in deze simulaties wordt gebruikt. Met de vooruitgang in rekenkracht zijn de mogelijkheden voor het bouwen van nauwkeurigere materiaalmodellen en het simuleren van grotere en meer realistische systemen toegenomen. Deze dissertatie is erop gericht het gedrag van NiTi op een atomistische schaal te begrijpen met behulp van dergelijke nauwkeurige modellen. Het werk dat voor dit proefschrift is gedaan bestaat uit twee delen. Als eerste worden al bestaande interatomaire potentiaalmodellen gebruikt om moleculaire dynamica (MD) simulaties uit te voeren om verschillende fase-transformatieverschijnselen in NiTi GM te beschrijven, waaronder pseudo-elasticiteit en het vorm-geheugen effect. Daarbij wordt het presteren van deze bestaande modellen vergeleken. Als tweede wordt een nieuwe NiTi interatomaire potentiaal ontwikkeld, gebruik makend van een database gegenereerd d.m.v. Density Functional Theory (DFT) berekeningen. DFT berekeningen presteren beter dan de bestaande modellen.

In **Hoofdstuk 2** wordt een vergelijking gemaakt tussen twee bestaande interatomaire potentialen, de embedded-atom-methode (EAM) en de een-na-naaste buur gemodificeerde embedded-atom-methode (2NN-MEAM) potentiaal. Dit wordt gedaan door het uitvoeren van MD-simulaties waarin uniaxiale trek- en drukbelasting langs een bepaalde oriëntatie wordt opgelegd aan een NiTi éénkristal. Er wordt waargenomen dat, hoewel de EAM een fase-transformatie voorspelt, de transformatierekken en de E-modulus van de twee fasen onnauwkeurig worden voorspeld. Wanneer dezelfde simulaties worden uitgevoerd met een 2NN-MEAM potentiaal, zijn de resultaten nauwer in overeenstemming met experimentele en theoretische waarden. De resultaten

geven aan dat de 2NN-MEAM beter presteert en betere voorspellingen doet, wat het gebruik ervan voor verdere berekeningen rechtvaardigt.

De 2NN-MEAM wordt vervolgens gebruikt om oriëntatie-afhankelijk gedrag in deze NiTi legeringen te analyseren. **Hoofdstuk 3** bespreekt met name de oriëntatie-afhankelijke pseudo-elasticiteit in eenkristallen. Drie verschillende initiële oriëntaties zijn gekozen en er wordt een eenassige belasting toegepast om de martensitische transformatie in deze eenkristallen te modelleren. Gezien het voorspellend vermogen van de 2NN-MEAM, produceert deze nauwkeurig transformatierekken in vergelijking met *ab initio* berekeningen. De MD simulaties tonen ook verschillen in het martensitische transformatiemechanisme in verschillende oriëntaties.

Hoewel de 2NN-MEAM beter presteert dan eerdere potentialen en de transformatierekken in meerdere richtingen kan reproduceren, worden sommige van de elastische constanten van de martensitische fase en de transformatietemperaturen nog steeds verkeerd voorspeld vergeleken met *ab initio* en experimentele waarden. Met dit in het achterhoofd wordt een nieuwe referentie-vrije vorm van de MEAM-potentiaal (RF-MEAM) ontwikkeld en geoptimaliseerd voor NiTi, zoals beschreven in **hoofdstuk 4**. *Ab initio* MD runs worden uitgevoerd voor zowel de austenitische als martensitische fasen bij verschillende temperaturen om configuraties te genereren voor het fitten van het RF-MEAM-potentiaal. Naast de energieën en atoomkrachten worden ook spanningssensoren van verschillende configuraties aan de fittingset toegevoegd. De nieuwe potentiaal voorspelt elastische constanten en de transformatietemperaturen nauwkeuriger dan bestaande interatomaire modellen, waardoor deze beter geschikt is voor het uitvoeren van MD-simulaties op generieke NiTi-systemen.

Hoofdstuk 5 toont de voorspellende kracht van de RF-MEAM-potentiaal. Hoewel de fitting-database tijdens de optimalisatie alleen bestond uit defectvrije configuraties met evenveel Ni als Ti, reproduceert de potentiaal ook het effect van defecten op de fase-transformatie in een NiTi eenkristal. De aanwezigheid van puntdefecten verlaagt de austenitische transformatietemperatuur drastisch, waardoor deze dichterbij de buurt komt van experimenteel bekende waarden. Korrelgrenzen en vrije oppervlakken in NiTi-systemen fungeren als een nucleatieplaats voor de austenitische transformatie, waardoor de voorwaartse transformatietemperatuur wordt verlaagd.

Samengevat is de interatomaire potentiaal het meest kritische onderdeel van elke MD-simulatie. De validiteit van de potentiaal voor een bepaalde toepassing moet worden geverifieerd alvorens conclusies te trekken op basis van de MD-resultaten. Hier wordt dit gedemonstreerd voor NiTi GM, en de lezer krijgt een

nieuw ontwikkelde potentiaal die gebruikt kan worden om resultaten te genereren voor het fine-tunen van NiTi-apparaten voor verschillende toepassingen.

1

INTRODUCTION

கற்க கசடறக் கற்பவை கற்றபின்
நிற்க அதற்குத் தக.
திருக்குறள், குறள் 391

*Learn without flaws what is worthy of being learned, and
live by it.*

Thirukkural, Kural 391

1.1. GENERAL INTRODUCTION

Shape-memory alloys (SMAs) are a unique class of metal alloys that show interesting deformation behavior. They can undergo large deformations in the order of 10% that can be recovered upon heating above a particular temperature. This leads to some fascinating phenomena such as the one-way and two-way shape-memory effects and pseudo/super-elasticity. Hence these materials have found widespread applications. Among the various shape-memory alloys that have been discovered so far, the equi-atomic nickel-titanium (NiTi) SMA, also known as Nitinol, has been the most widely used for different practical applications owing to their superior mechanical behavior, corrosion resistance, and the ability to recover its original shape close to room temperature [1].

The shape-memory, or the ability to exist in two different shapes, arises due to a reversible phase transformation between two crystalline phases of NiTi. The parent phase, known as austenite, has a B2 (body centered cubic) crystal structure with Ni atoms at the corner and Ti atoms at the center of the cube and vice-versa. Upon cooling, or under the application of stress (or strain), the parent phase transforms into the product martensite phase which has a monoclinic B19' crystal structure with a monoclinic angle close to 97.7°. The martensitic distortion of the B2 to the B19' is schematically represented in Fig. 1.1. The figure on the left hand side shows four cubic B2 cells in black, with Ni atoms at the corner (blue colored balls) and Ti atoms at the center (red colored balls) of the cube. Upon a $(110)[\bar{1}\bar{1}0]_{B2}$ basal shear and a $(001)[1\bar{1}0]_{B2}$ non-basal shear, the B2 structure transforms into the B19' structure. The B19' crystal structure is shown with respect to the B2 crystal in Fig. 1.1(b). During a thermal or a loading cycle, NiTi transforms between these two crystal structures leading to its unique properties.

Although NiTi SMAs have been extensively used in the industry, there are still a number of fundamental ambiguities over the past couple of decades that have interested researchers. For instance, the crystal structure of the martensitic B19' phase was not unambiguously established until 2003, when Huang *et al.* [3] performed *ab initio* studies to obtain a stable B19' crystal structure in their calculations. More recently, development of nano-crystalline NiTi alloys have attracted a lot of attention. Their excellent strength and thermo-mechanical behavior at the nano-scale have led to a number of ongoing experimental research on the nano-scale phase transformation mechanism and the differences with respect to their bulk counterparts. Another area of ambiguity is the formation and role of martensitic twins during temperature- and stress-induced phase transformation. Performing such transformation experiments on nano-crystalline or single-

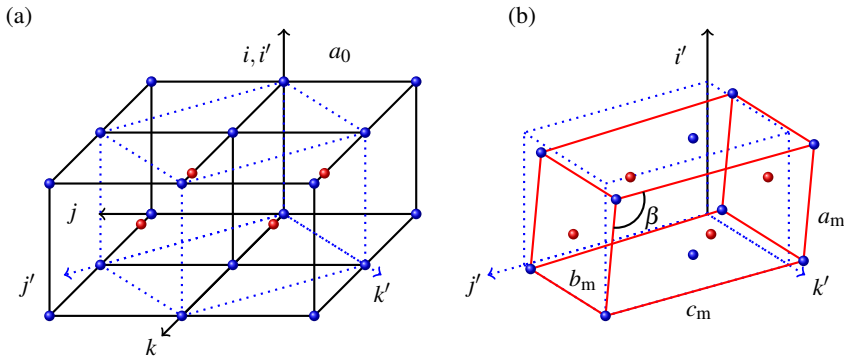


Figure 1.1: Schematic of the B2-B19' lattice deformation in NiTi [2]: (a) Ni atoms are represented by blue colored balls and Ti atoms are represented by red colored balls; (i, j, k) represent the B2 reference frame; i', j' and k' lie along the $[001]$, $[110]$ and $[\bar{1}10]$ direction of the reference frame; B2 is represented by blue dotted lines viewed in the (i', j', k') reference frame; (b) distortion of B2 (blue dotted lattice) to B19' (red lattice); the lattice constant of B2 is a_0 and the lattice constants of B19' are a_m , b_m , c_m and β .

crystal SMAs is also challenging due to the difficulty involved in processing them.

In this regard, a theoretical approach towards studying and analyzing SMA behavior is useful in overcoming such ambiguities and supplementing experimental results. Computational simulation techniques including density functional theory (DFT) and molecular dynamics (MD) provide a fundamental understanding of the various mechanisms during phase transformation in these alloys. Although DFT calculations are more accurate, they are limited by the length and time-scale of these simulations. MD simulations provide a faster approach towards modeling transformations in larger systems at a nano-scale. The accuracy of any MD simulation is based on the underlying interatomic potential that drives the motion of atoms in the system. The interatomic potential is an analytical expression describing the energy of two interacting particles. In general, the interatomic potentials are parametrized using a database of energies and atomic forces in various configurations generated from *ab initio* calculations. To model the phase transformations in NiTi, a number of interatomic potential models have been developed and parametrized in literature. As global computational power increases, more complex potentials are being optimized with a growing database, and the accuracy of the models is always increasing.

For instance, the first potentials that were developed were simple Lennard-

Jones type potentials that were built to qualitatively model the square-tetragonal transformation in a model 2-D NiTi structure [4, 5]. In 2010, [Zhong *et al.* \[6\]](#) and [Mutter and Nielaba \[7\]](#) independently obtained parameters for an embedded-atom method (EAM) potential that predicted temperature- and stress-induced phase transformations in single-crystal NiTi nano-wires and bulk oriented along a particular direction. A more recent and accurate parametrization of the EAM was obtained by [Ren and Sehitoglu \[8\]](#) to model the B2-B19' transformation. More recently, a second nearest neighbor modified embedded-atom method (2NN-MEAM) potential was parametrized by [Ko *et al.* \[9\]](#), which included three-body terms and accounted for the directionality of bonds in NiTi. The MEAM potential was able to predict phase transformation mechanisms in poly-crystal NiTi and free-standing NiTi nano-particles [10, 11]. Each of these potentials has their own merits and demerits and are restricted simultaneously in terms of accuracy and applicability. Since the interatomic potential is the most critical aspect of the MD simulations, their validity and applicability needs to be tested before drawing any conclusions from the MD results. With increasing computing power and advent of new fitting techniques, there is always scope to build better-tailored potentials by varying the underlying dataset used for optimization. Keeping this in mind, this thesis focuses on two aspects of MD simulations of NiTi SMAs. MD runs are performed using existing potentials to describe interesting shape-memory phenomena and to draw comparisons between different potentials and discuss their drawbacks. In addition, a new reference free formalism of the MEAM potential is developed for NiTi. This new potential outperforms existing interatomic potentials in predicting the deformation behavior of NiTi.

1.2. OBJECTIVE AND OUTLINE OF THE THESIS

The main objective of the thesis is to perform MD simulations on various NiTi systems and develop an interatomic potential that predicts thermo-mechanical behavior that closely resembles experimental data. By doing so, the potential can be used to run MD simulations whose results would help in optimizing the production of SMA devices for certain applications. To this end, a reference-free version of the MEAM potential, called RF-MEAM potential, is developed for NiTi.

The thesis begins with a comparison of the performance of two existing interatomic potentials, the EAM-Finnis-Sinclair potential and the 2NN MEAM potential, in predicting SMA behavior. Chapter 2 discusses why the MEAM outperforms the EAM potential by demonstrating a simple uni-axial loading simulation of a NiTi single crystal along a particular orientation. Although both interatomic

potentials predict the stress-induced martensitic transformation, the deformation properties (Young's modulus of both phases and the transformation strain) are wrongly predicted by the EAM potential. The results are compared to those calculated using a single cell lattice deformation model (LDM) [12]. The reason for the superior performance of the MEAM potential is attributed to the inaccurate lattice and elastic constants of both phases predicted by the EAM in comparison to the MEAM potential. The predictive power of the MEAM potential is expressed in Chapter 3 in which MD results describing the orientation-dependent pseudo-elastic behavior of NiTi single-crystals are shown. Strain-controlled loading simulations are performed to predict phase transformation mechanisms along various directions. The effect of temperature on the stress-induced transformation behavior is also analyzed. The consequence of orientation dependence and tension-compression asymmetry on deformation of NiTi single-crystal systems is also demonstrated by performing bending simulations of three differently oriented nano-wires.

While performing stress-induced transformation simulations along different orientations, it is noticed that, although the MEAM potential is quite suitable to model NiTi behavior, there are still differences in certain properties with respect to experimental results. For instance, the predicted values of the transformation temperatures and the hysteresis during the cooling-heating cycle, and some elastic constants of the martensitic phase, are inaccurate by more than 10% when compared to experimental values. In view of this, Chapter 4 discusses the development of a new interatomic potential for NiTi, named the reference-free MEAM (RF-MEAM) potential. The primary advantage of this potential formalism is that the dependency of the pair potential part of the MEAM formalism on the reference structure is completely removed by also defining the pair potential part as an analytical function. Besides this, the potential is also fit to stress tensors of different martensitic and austenitic configurations, in addition to energies and atomic forces. The result is a new parametrization for NiTi, whose predictive performance of the thermo-mechanical properties is better than that of the MEAM potential. A section towards the end of this chapter also describes, as a proof-of-concept, the extension of the RF-MEAM fitting and MD simulation methodology to a multi-component (four component) high entropy alloy. In Chapter 5, the robustness of the new NiTi RF-MEAM potential is demonstrated by performing MD simulations on defective NiTi systems. The effect of point defects like anti-sites, vacancies and compositional defects, and the effect of grain boundaries and free surfaces on the phase transformation behavior is studied. MD simulations using the RF-MEAM potential predict that the presence of such defects

drastically reduces the austenitic transformation temperature, bringing it closer to experimentally observed values. Grain boundaries and free surfaces act as a nucleation site for the forward transformation to the austenitic phase. While only ideal defect-free single crystals are a part of the fitting database, the quality of these results demonstrates the predictive power of the newly developed potential.

REFERENCES

- [1] K. Otsuka and C. Wayman, *Shape Memory Materials* (Oxford University Press, 1999).
- [2] S. Mao, J. Luo, Z. Zhang, M. Wu, Y. Liu, and X. Han, *EBSD studies of the stress-induced B2-B19' martensitic transformation in NiTi tubes under uniaxial tension and compression*, *Acta Materialia* **58**, 3357 (2010).
- [3] X. Huang, G. J. Ackland, and K. M. Rabe, *Crystal structures and shape-memory behaviour of NiTi*, *Nature Materials* **2**, 307 (2003).
- [4] O. Kastner, *Molecular-dynamics of a 2D model of the shape memory effect*, *Continuum Mechanics and Thermodynamics* **15**, 487 (2003).
- [5] O. Kastner, G. Eggeler, W. Weiss, and G. Ackland, *Molecular dynamics simulation study of microstructure evolution during cyclic martensitic transformations*, *Journal of the Mechanics and Physics of Solids* **59**, 1888 (2011).
- [6] Y. Zhong, K. Gall, and T. Zhu, *Atomistic study of nanotwins in NiTi shape memory alloys*, *Journal of Applied Physics* **110**, 033532 (2011).
- [7] D. Mutter and P. Nielaba, *Simulation of the shape memory effect in a NiTi nano model system*, *Condensed Matter and Materials Science* **577**, S83 (2013).
- [8] G. Ren and H. Sehitoglu, *Interatomic potential for the NiTi alloy and its application*, *Computational Materials Science* **123**, 19 (2016).
- [9] W.-S. Ko, B. Grabowski, and J. Neugebauer, *Development and application of a Ni-Ti interatomic potential with high predictive accuracy of the martensitic phase transition*, *Physical Review B* **92**, 134107 (2015).
- [10] W.-S. Ko, S. B. Maisel, B. Grabowski, J. B. Jeon, and J. Neugebauer, *Atomic scale processes of phase transformations in nanocrystalline NiTi shape-memory alloys*, *Acta Materialia* **123**, 90 (2017).
- [11] S. B. Maisel, W.-S. Ko, J. L. Zhang, B. Grabowski, and J. Neugebauer, *Thermo-mechanical response of NiTi shape-memory nanoprecipitates in TiV alloys*, *Physical Review Materials* **1**, 033610 (2017).
- [12] T. Saburi, M. Yoshida, and S. Nenno, *Deformation behaviour of shape memory TiNi crystals*, *Scripta Metallurgica* **18**, 363 (1984).

2

MODELING PSEUDO-ELASTICITY: MEAM vs EAM

A comparison of the EAM-Finnis-Sinclair and the MEAM potential, two of the recently developed potentials to model NiTi, is carried out. The potentials are compared by studying the pseudo-elastic behavior in bulk NiTi for one specific crystallographic orientation. To this end we perform, for the first time, simulations where the transformation occurs not only under compressive but also under tensile loading along $\langle 100 \rangle_{B2}$ using both potentials. Results indicate that in both cases the MEAM potential captures the pseudo-elastic behavior more accurately. By using a lattice deformation model, it is demonstrated that the inaccurate transformation strains predicted by the EAM-Finnis-Sinclair potential are a direct consequence of its inability to predict experimental values of the lattice constants. Similarly, it is shown that the more precise values of the Young's modulus of the initial austenitic and the final martensitic phase estimated by the MEAM potential are the result of its ability to predict elastic constants more accurately than the EAM-Finnis-Sinclair potential. As a result, it is concluded that the MEAM potential is better suited to study the overall pseudo-elastic behavior in NiTi.

2.1. INTRODUCTION

Pseudo-elasticity in nickel-titanium (NiTi) shape-memory alloys (SMAs) arises due to a reversible stress-induced phase transformation from the austenitic to the martensitic phase. Molecular dynamics (MD) simulations are employed to model this transformation. They can provide insights into changes in the nanostructure of the alloy that cannot be easily identified through experiments. In this work, we demonstrate the superior performance of the MEAM potential [2], compared to the EAM-Finnis-Sinclair (EAM-FS) potential [3, 4], to study pseudo-elastic behavior of bulk NiTi.

Actuation and damping devices made from SMAs rely on pseudo-elasticity of the alloy. During pseudo-elasticity, the alloy transforms into a monoclinic B19' martensitic phase from the austenitic B2 (BCC) phase. In general, pseudo-elasticity in NiTi single-crystals depends on the orientation of the crystal [5, 6]. In polycrystals, the effect of the distribution and orientation of the crystals on the mechanical behavior of the alloy becomes progressively more important as the specimen dimensions decrease and can be significant in micro and nano-scale devices [7–9] where the specific orientation of a few crystals determines the overall mechanical response. Hence it becomes important to describe the mechanical response of single crystals. In this respect, MD simulations constitute a versatile platform that allows, contrary to experiments, to load a single crystal with simple geometry along any crystallographic direction.

Two of the recently developed interatomic potentials to model NiTi are the embedded atom Method - Finnis-Sinclair (EAM-FS) potential [3, 4] and the Modified embedded atom Method (MEAM) potential [2], both described in Section 2.2. Ko *et al.* [2] showed that the MEAM potential accurately predicts pseudo-elastic behavior in $\langle 100 \rangle_{B2}$ oriented NiTi nano-pillars under compression. They obtained a transformation strain of 5% during the B2-B19' transformation, a value close to that obtained with the Lattice Deformation Model (LDM) proposed by Saburi and Nenno [10, 11]. This model, based on calculation of lattice distortion during the B2-B19' transformation of an isolated and unconstrained B2 lattice, predicts the final variant of martensite that is formed when austenite is loaded along a generic direction. From this, it is possible to calculate the transformation strain of a single B2 unit cell along a generic orientation. The results in this work, reported in Section 2.3, show that the simulation reported by Ko *et al.* [2], performed with the EAM-FS potential, does not predict the correct transformation behavior although the EAM-FS potential has been reported to predict pseudo-elasticity during compression along $\langle 110 \rangle_{B2}$ [3, 4]. Here, we have also performed, for the first time, simulations

of the tensile behavior of bulk NiTi along $\langle 100 \rangle_{B2}$ using both potentials. The MEAM potential appears to outperform the EAM-FS as it predicts the elastic deformation of the austenitic and martensitic phase, separated by a stress plateau under both tension and compression, and correct transformation strain values.

To validate the results obtained using the MEAM potential, the predicted transformation strain values are compared to those obtained with the LDM in Section 2.4. The coefficients of the elastic tensor of the initial B2 phase and the final B19' variants obtained under compressive and tensile loading are compared to those obtained with *ab initio* simulations. The results confirm that the MEAM potential is better suited to study the overall pseudo-elastic behavior in NiTi and also the mechanical behavior of the individual phases. The reason for the limitations of the EAM-FS potential and how the MEAM potential overcomes them are described in Section 2.5.

2.2. METHOD

There is general consensus that the most important aspect of any MD simulation is the choice of the interatomic potential. In the case of SMAs this is particularly challenging because the alloy has a different stable phase at high temperature and low temperature. The potential must predict accurate material properties for both phases, apart from predicting the phase transformation. Two of the recently developed interatomic potentials to model NiTi are employed in this work and their capability to predict pseudo-elastic behavior is assessed.

The EAM-FS potential originates from the second-moment approximation of the tight-binding model and was developed by [Finnis and Sinclair \[12\]](#). In the EAM-FS formulation, the total energy of the system is expressed as

$$E = \sum_i \left\{ A_{\alpha\beta} \exp \left[-p_{\alpha\beta} \left(\frac{r_{ij}}{d_{\alpha\beta}} - 1 \right) \right] - \sqrt{\sum_{j \neq i} F(r_{ij})} \right\}$$

with

$$F(r_{ij}) = \xi_{\alpha\beta}^2 \exp \left[-2q_{\alpha\beta} \left(\frac{r_{ij}}{d_{\alpha\beta}} - 1 \right) \right]$$

where r_{ij} denotes the distance between atoms i and j , and indices $\alpha\beta$ represent the different atomic interaction combinations Ni-Ni, Ni-Ti and Ti-Ti. The first term in the summation is a repulsion term and the second term represents metallic bonding. The 15 parameters for the binary NiTi alloy (ξ , p , d , A and

q for Ni-Ni, Ti-Ti and Ni-Ti interaction) were determined by Lai and Liu [13]. To reduce the computational effort, Mutter and Nielaba [3] and Zhong *et al.* [4] chose a cut-off radius of 4.2 Å disregarding weak long-range interactions. They also proposed, independently, a smooth cut-off function between 4 Å and 4.2 Å to avoid diverging forces at a distance corresponding to the cut-off radius.

More recently, Ko *et al.* [2] realized that the directionality in the metallic bonds could not be captured accurately by simple interatomic potential models whereas the MEAM potential, with implicit angle-dependent terms in its formulation, would be more suitable. They therefore developed parameters for a MEAM potential to describe the NiTi phase transformation. The strong directionality of the bonds in the martensitic crystal stems from the position of Ni and Ti atoms on the faces of the monoclinic unit cell. According to the MEAM formulation, the total energy, also a summation of an embedding energy term and a pairwise repulsion term, is approximated as

$$E = \sum_i \left[F_i(\bar{\rho}_i) + \frac{1}{2} \sum_{j(\neq i)} S_{ij} \phi_{ij}(R_{ij}) \right],$$

where F_i is the embedding energy function of the electron density ρ_i , ϕ_{ij} is the pair interaction between atoms i and j at distance R_{ij} , and S_{ij} is the screening function. While the EAM-FS potential contains only spherically averaged atomic electron densities, the MEAM potential introduces additional angular terms in the embedding energy term. For the calculation of F_i , the functional form of the background electron density is computed by combining several partial electron densities $\rho^{a(h)}$, with h in the range from 0 to 4, expressed as

$$\rho^{a(h)}(R) = \rho_0 \exp \left[-\beta^{(h)} (R/r_e - 1) \right],$$

where ρ_0 , the atomic electron density scaling factor, and $\beta^{(h)}$, the decay lengths, are adjustable parameters, and r_e is the nearest-neighbor distance in the reference structure. At variance with the EAM formulation, the pair interaction $\phi_{ij}(R_{ij})$ is computed from a known value of the total energy and the embedding function for an atom in an equilibrium reference structure in the MEAM formulation. The total energy per atom is obtained from the universal equation of state [14]

$$E^u(R) = -E_c \left(1 + a^* + da^{*3} \right) e^{-a^*},$$

with

$$a^* = \alpha (R/r_e - 1) \quad \text{and} \quad \alpha = \left(\frac{9B\Omega}{E_c} \right)^{1/2},$$

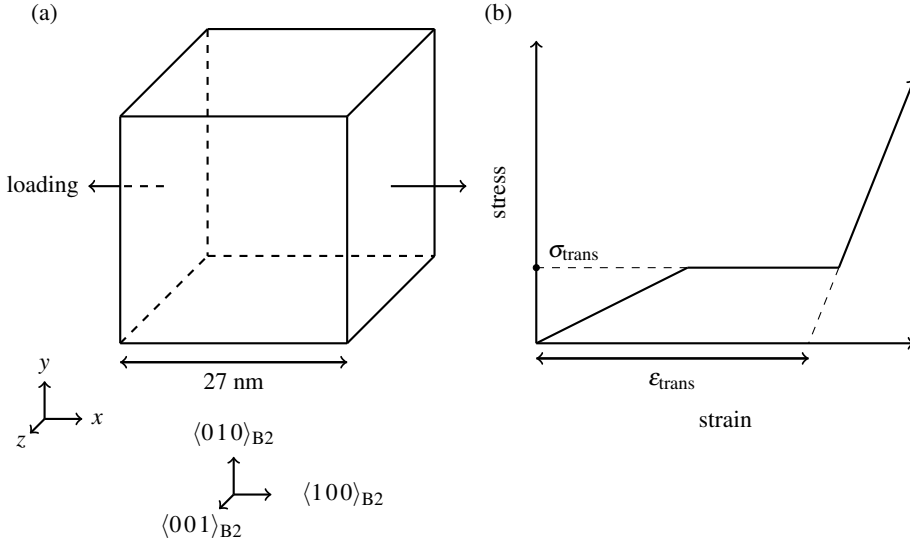


Figure 2.1: (a) Schematic representation of the $\langle 100 \rangle_{B2}$ oriented initial bulk NiTi crystal, periodic in all directions. (b) Representation of the theoretical austenite-martensite deformation behavior. The transformation strain and stress are indicated as ϵ_{trans} and σ_{trans} .

where d is an adjustable parameter, E_c is the cohesive energy, B is the bulk modulus, and Ω is the equilibrium atomic volume of the reference structure. A complete formulation of the MEAM potential is available in the literature [15, 16]. Additional details about the parameters for the NiTi system can be found in the work of Ko *et al.* [2].

MD simulations are performed starting from a fully periodic $27 \times 27 \times 27 \text{ nm}^3$ simulation box. Atoms are placed according to the B2 crystal structure with the basis vectors along $\langle 100 \rangle_{B2}$, $\langle 010 \rangle_{B2}$ and $\langle 001 \rangle_{B2}$ as shown in Fig. 2.1(a). After an energy minimization, the B2 structure is thermally equilibrated at 325 K, yielding a configuration on which strain-controlled and stress-controlled isothermal tensile and compressive loading simulations are performed with both interatomic potentials. In the strain-controlled simulations, all atoms are moved in the x -direction ($\langle 100 \rangle_{B2}$), the system is equilibrated at every time step, and the corresponding stress σ_{xx} is calculated. The deformation is applied at a strain rate of 10^6 s^{-1} at 325 K and the pressure on the other faces is maintained at 0 Pa. In the stress-controlled simulations, the stress σ_{xx} is increased by 0.01 MPa every time step and the corresponding strain is calculated after equilibration. The pressure on the other faces is maintained at 0 Pa. The simulations are performed using

LAMMPS [17]. A constant timestep (0.5 fs) is used. Temperature and pressure are controlled using a Langevin thermostat [18] and a Berendsen barostat [19], respectively. The deformation behavior is described by plotting the virial stress [20] on the x -plane in the x -direction against the corresponding engineering strain component.

The theoretical stress-strain response of the alloy under stress-controlled loading is schematically shown in Fig. 2.1(b). Here it is assumed that during transformation all austenite transforms into martensite, and this happens at constant stress σ_{trans} . The stress at which the behavior of the initial austenitic phase deviates from elasticity is defined as the transformation stress σ_{trans} . When the fully martensitic elastic loading part of the curve is extended to a null stress level, the corresponding strain is defined as the transformation strain ϵ_{trans} .

In a strain-controlled simulation, when the atoms are displaced such that the resulting strain is more than the strain corresponding to σ_{trans} , the response is characterized by a combination of stress increase due to the elastic loading of untransformed austenite, stress increase due to the elastic loading of transformed martensite, and stress drop caused by the transformation, until the entire crystal is transformed. Hence a perfect plateau cannot be achieved in a strain-controlled phase transformation simulation. The lack of a perfect stress plateau has also been observed in strain-controlled experiments [21] and earlier MD simulation results [22]. This is also reflected in the MD results described next.

2.3. RESULTS

Figures 2.2(a) and 2.2(b) show the stress-strain curve when the B2 phase is loaded along $\langle 100 \rangle_{\text{B2}}$ in tension and compression using the MEAM and the EAM-FS potential during stress-controlled loading. Figures 2.2(c) and 2.2(d) show the stress-strain curve obtained during a strain-controlled loading of the B2 phase along the same direction.

As expected, stress-controlled loading (Figs. 2.2(a) and 2.2(b)) leads to the formation of a stress plateau during phase transformation. When the stress crosses point C in compression or point A in tension, the strain jumps immediately to point D or point B, respectively, thereby leading to a perfect stress plateau. A small kink is observed at points B and D in Fig. 2.2(a) and at point G' in Fig. 2.2(b). These are the points corresponding to the end of the transformation. Due to the inevitable high loading rates in MD, the system completely transforms from austenite to martensite almost instantaneously leading to the kink in the stress-strain curve.

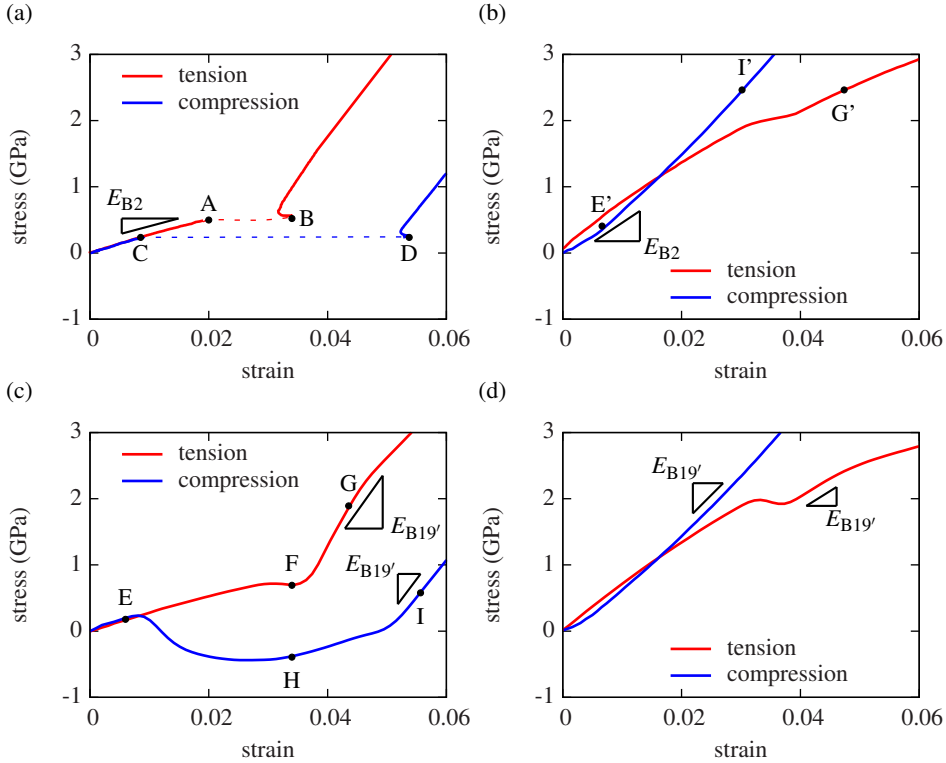


Figure 2.2: Isothermal stress-strain behavior of bulk NiTi under stress-controlled (top) and strain-controlled (bottom) tensile and compressive loading along the $\langle 100 \rangle_{B2}$ direction at $T = 325$ K simulated using the MEAM (left) and the EAM-FS (right) interatomic potential.

In strain-controlled loading, a plateau is never observed. The transformation starts when the transformation stress is reached. Because of heterogeneities due to randomness in position and velocity of the atoms, the stress level is not uniform within the system and only some parts of the bulk transform into a $B19'$ phase. Since the $B19'$ phase offers less resistance to deformation compared to an equally strained $B2$ phase, the $B2$ - $B19'$ transformation causes a stress drop. The remaining bulk material that does not transform continues to elastically deform. Similarly, the bulk that was already transformed into $B19'$ deforms elastically but with a different slope. Hence during a strain-controlled loading, the stress in the intermediate region is caused by an interplay of stress drops due to the $B2$ - $B19'$ transformation and stress increase due to the elastic deformation, yielding an overall non-linear behavior. In general, the former effect is prevalent in the early

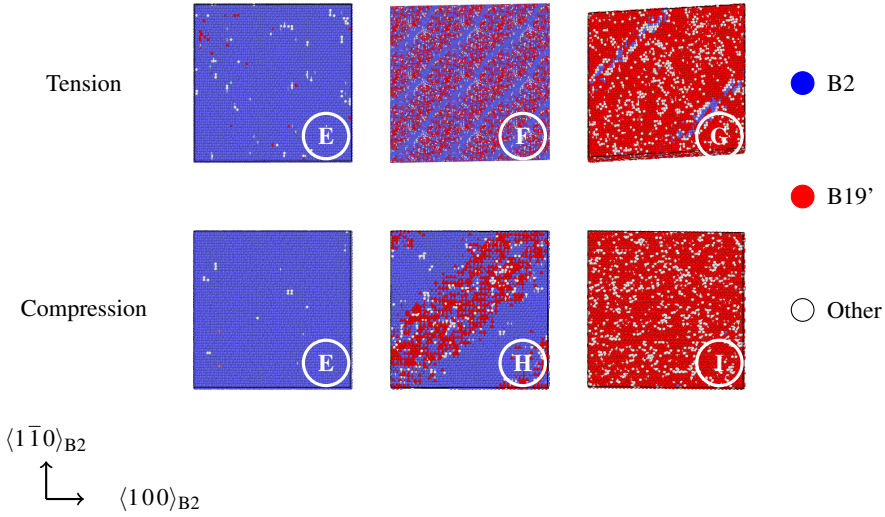


Figure 2.3: Sectional view of NiTi bulk cut along the $\langle 1\bar{1}0 \rangle_{B2}$ plane colored according to the common neighbor analysis (CNA) pattern. Blue atoms represent B2, red atoms represent B19' and white atoms represent those that are neither B2 nor B19'. The simulation is performed under strain control with the MEAM potential. Refer to Fig. 2.2(c) for the labels E to I. The austenite transforms into martensite through the formation of Lüders-like bands.

stages of the phase transformation and causes a stress drop; the stress however gradually increases towards the end of the intermediate region since the effect of elastic deformation becomes more dominant as more atoms have already transformed into the B19' phase.

Most importantly, comparison of the left and the right hand side of Fig. 2.2 shows that a clear phase transformation is observed under tension and compression only using the MEAM potential. On the contrary, when NiTi is modeled using the EAM-FS potential, an intermediate plateau-like region is not observed at all in compression and is almost negligible in tension although the crystal transforms from the B2 to the B19' phase.

However, the elastic slopes of the B2 and the B19' phase along the $\langle 100 \rangle_{B2}$ are differently predicted by the two potentials. From Fig. 2.2(a) (or Fig. 2.2(c)) and with the MEAM potential, the Young's modulus of the B2 phase is 31 GPa and that of B19' phase formed under tensile (compressive) loading is 122 (113) GPa. The Young's modulus of the martensitic phase is different under tension and compression because a different variant of martensite is formed under tension and compression as shown in Fig. 2.4. From Fig. 2.2(b) (or Fig. 2.2(d)) and with

Table 2.1: MD simulation results of transformation strain in tension and compression, Young's modulus of the B2 phase, and Young's modulus of the tensile and compressive B19' variant at 325 K using the MEAM and EAM-FS potential compared to transformation strains obtained from the LDM [10, 11] and B2 and B19' Young's moduli calculated from *ab initio* elastic constants [23].

	$\epsilon_{\text{trans}}^{\text{tens}}$ (%)	$\epsilon_{\text{trans}}^{\text{comp}}$ (%)	E_{B2} (GPa)	$E_{\text{B19}'}^{\text{tens}}$ (GPa)	$E_{\text{B19}'}^{\text{comp}}$ (GPa)
LDM	2.662	4.201			
<i>ab initio</i> (0 K)			43	180	115
MEAM (325 K)	3.104	5.011	31	122	113
EAM-FS (325 K)	0.122	0	80	88	84

the EAM-FS potential, it is observed that the Young's modulus of the B2 phase is 80 GPa and that of the tensile (compressive) B19' variant is 88 (84.4) GPa.

The strain-controlled loading simulation allows to fully characterize nano-structural changes during phase transformation. Figure 2.3 shows a sectional view of the bulk corresponding to points E, F and G along the tensile curve and E, H and I along the compressive curve in Fig. 2.2(c). The atoms are colored according to the common neighbor analysis (CNA) pattern [24] with B2 phase atoms in blue and B19' phase atoms in red. The transformation progresses through the formation of Lüders-like bands in both tension and compression. This nano-structural analysis cannot be performed in a stress-controlled loading simulation because the system jumps from point A to point B and from point C to point D, and the response in the intermediate region cannot be analyzed. The response during the other stages of loading is identical in both stress- and strain-controlled loading. Notice also that in a stress-controlled loading simulation when the atoms of the crystal obtained using the EAM-FS potential are colored according to the CNA pattern, a fully B2 crystal (corresponding to point E' which is identical to E) becomes a fully B19' crystal (corresponding to G' and I' which are identical to G and I, respectively) in tension and compression almost instantaneously. Hence separate images using the EAM-FS potential are not shown here.

Although the phase transformation is predicted also by the EAM-FS potential, the transformation strains are inaccurate. Since the plateau region is absent in compression and very small in tension, refer to the right column of Fig. 2.2, the nano-structural changes that are characterized using the MEAM potential (points F and H in Fig. 2.3) during the phase transformation cannot be predicted by the EAM-FS potential irrespective of whether a strain-controlled or a stress-controlled loading simulation is performed.

The results obtained from MD simulations using both interatomic potentials

at 325 K are summarized in Table 2.1 and are compared to transformation strain values obtained from the lattice deformation model (LDM) [10, 11] described in detail in the next section and 0 K Young's modulus calculated from *ab initio* values of the elastic constants [23]. Table 2.1 shows that the LDM transformation strain of 2.662% (4.201%) during tension (compression) is not predicted by the EAM-FS potential (0.12% and 0% in tension and compression, respectively). The EAM-FS potential also predicts a stiffer initial B2 phase and less stiff B19' variants than those calculated from *ab initio* elastic constants. The reason for the difference is further discussed in the next section.

2.4. LATTICE DEFORMATION MODEL

During a stress-induced phase transformation, the symmetric B2 austenite crystal transforms into a monoclinic B19' crystal. The B19' crystal can be oriented in different ways with respect to the initial B2 crystal. Hence a phase transformation from B2 to B19' can lead to any of the 12 equivalent lattice corresponding martensite variant pairs (CVP), which differ in orientation with respect to the parent B2 crystal. The Lattice Deformation Model (LDM) [10, 11] allows to identify the B19' variant that forms at the end of the stress-induced transformation. According to the LDM, the variant of B19' that forms when B2 is loaded in any arbitrary direction is the one that produces the maximum strain along that particular loading direction. By applying LDM, the variant that is formed and the transformation strains have been calculated for all loading directions for a single B2 crystal in [11, 25, 26]. The calculations have been experimentally validated through various single crystal uniaxial loading experiments in [11, 27, 28]. For the current study, where B2 is loaded along the $\langle 100 \rangle_{B2}$ direction, Fig. 2.4 shows the initial B2 crystal (dotted blue lines) and the B19' variant (solid red lines) that forms according to the LDM under compression and tension.

The transformation strain values for the two B19' variants shown in Fig. 2.4 are calculated from the experimentally known lattice constants of B2 and B19' listed in Table 2.2 using the LDM. When B2 is loaded in compression along $\langle 100 \rangle_{B2}$, the B19' variant (Fig. 2.4(a)) that forms is oriented in a way that the side corresponding to the lattice constant a_m of B19' falls along the loading axis. The LDM transformation strain in a single crystal corresponding to this transformation is

$$\epsilon_{\text{trans}}^{\text{comp}} = \frac{a_m - a_0}{a_0} = 4.201\%. \quad (2.1)$$

Likewise, the B19' variant that forms under tension is shown in Fig. 2.4(b), and

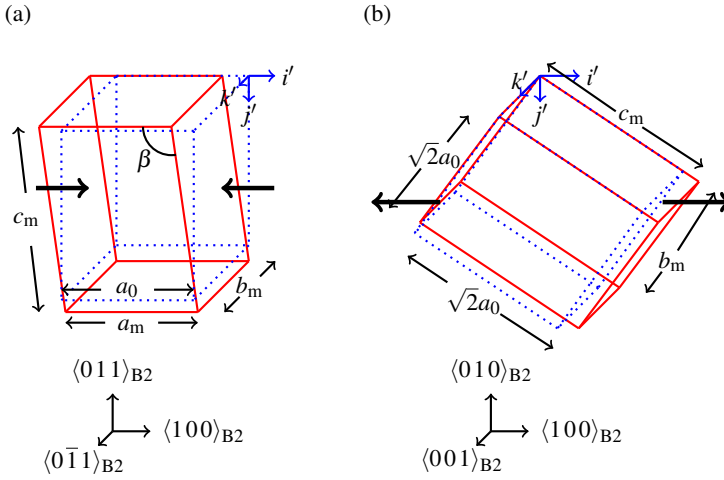


Figure 2.4: Schematic representation of the B2 (blue dotted) - B19' (red solid) deformation during (a) compressive and (b) tensile loading along the $\langle 100 \rangle_{B2}$ direction as predicted by LDM. The lattice constants a_m , b_m , c_m and the angle β are associated with B19' while a_0 is the lattice constant associated with B2. The reference frame (i', j', k') lies along the $\langle 100 \rangle_{B2}$, $\langle 0\bar{1}\bar{1} \rangle_{B2}$ and $\langle 0\bar{1}1 \rangle_{B2}$ direction, and $\langle 100 \rangle_{B2}$, $\langle 010 \rangle_{B2}$ and $\langle 001 \rangle_{B2}$ direction, respectively. The loading, represented by thick black lines, is along $\langle 100 \rangle_{B2}$. The orientation of the monoclinic B19' lattice with respect to the initial B2 lattice is different in compression and tension although the initial B2 lattice lies along the same direction (only represented along different basis vectors in (a) and (b)).

the corresponding transformation strain in a single crystal is

$$\epsilon_{\text{trans}}^{\text{tens}} = \frac{\sqrt{b_m^2 + c_m^2} - 2a_0}{2a_0} = 2.662\%. \quad (2.2)$$

These transformation strain values correspond to values reported in the literature (LDM [11, 29] and *ab initio* [23]). In addition to the transformation strain values, the Young's modulus of the initial B2 crystal loaded along $\langle 100 \rangle_{B2}$ and the tensile and compressive B19' variants can also be calculated from the corresponding elastic constants. The values of the three elastic constants associated with the cubic B2 structure and the 13 elastic constants associated with the monoclinic B19' structure at 0 K obtained from *ab initio* simulations are listed in Tables 2.3 and 2.4, respectively. From the values in Table 2.3, the Young's modulus of the B2 crystal along the $\langle 100 \rangle_{B2}$ direction can be related to the elastic constants by [30]

$$E_{B2} = \left(\frac{2}{3(C_{11} - C_{12})} + \frac{1}{3(C_{11} + 2C_{12})} \right)^{-1} = 43 \text{ GPa.} \quad (2.3)$$

For the monoclinic B19' crystal, the Young's modulus along the direction normal to any (hkl) plane can be calculated as [31, 32]

$$\begin{aligned} \left(E_{B19'}^{hkl} \right)^{-1} &= n_1^4 S_{11} + 2n_1^2 n_2^2 S_{12} + 2n_1^2 n_3^2 S_{13} + 2n_1^3 n_3 S_{15} \\ &+ n_2^4 S_{22} + 2n_2^2 n_3^2 S_{23} + 2n_1 n_2^2 n_3 S_{25} + n_3^4 S_{33} + 2n_1 n_3^3 S_{35} \\ &+ n_2^2 n_3^2 S_{44} + 2n_1 n_2^2 n_3 S_{46} + n_1^2 n_3^2 S_{55} + n_1^2 n_2^2 S_{66}, \quad (2.4) \end{aligned}$$

where n_1 , n_2 and n_3 are the direction cosines between the normal to the (hkl) plane and the lattice vectors (a , b and c) of B19', and S_{ij} are the components of the compliance matrix. Further details regarding notations and conventions associated with the B19' structure can be found in [23, 32]. By using this formula and from the values shown in Table 2.4, the Young's modulus of the tensile (compressive) B19' variant (Fig. 2.4) is equal to 180 (115) GPa. The accuracy of the values of the elastic constants predicted by MEAM and EAM-FS in Tables 2.3 and 2.4 (columns 3 and 4) will be discussed in the following section.

2.5. CONCLUDING REMARKS

In the previous section we have discussed how the transformation strain and the Young's modulus along any arbitrary direction, two properties that describe accurate pseudo-elastic behavior, can be calculated from the lattice constants and elastic constants, respectively, once the B19' variant is known. The MD simulations in this study predict the same B19' variant (Fig. 2.5) irrespective of the potential used. The stress-strain behavior is however different (Fig. 2.2). Hence we here again apply the LDM for the B2-B19' transformation, but this time with the lattice constants predicted by the two interatomic potentials (Table 2.2) instead of the experimental lattice constants. The calculated transformation strains under compression and tension along $\langle 100 \rangle_{B2}$ are listed in the third and fourth row of Table 2.5. These values are similar to those obtained by performing MD simulations (Table 2.1). The small differences arise because of the simulations being performed at 325 K and fluctuations associated with the effect of temperature, whereas the calculations are made on 0 K MEAM and EAM-FS lattice constant values. Even though both potentials predict the correct B19' variant, the MEAM potential is more accurate in the estimation of the transformation strains in tension and compression because of its ability to predict more accurate lattice constants.

Table 2.2: Lattice constants of B2 and B19' and monoclinic angle β together with the corresponding percentage errors for the values predicted by the interatomic potentials with respect to experimental lattice constants and monoclinic angle.

Lattice constants	Type	a_0 (nm)	a_m (nm)	b_m (nm)	c_m (nm)	β (°)
experiment [33]	B2	0.3015				
	B19'		0.2889	0.4120	0.4621	96.80
MEAM [2]	B2	0.2999 (0.51%)				
	B19'		0.2878 (0.38%)	0.4129 (0.22%)	0.4659 (0.84%)	99.01 (2.27%)
EAM-FS [4]	B2	0.3008 (0.23%)				
	B19'		0.3005 (4.01%)	0.4022 (2.38%)	0.4466 (3.33%)	98.08 (1.32%)

Table 2.3: Elastic constants of B2 from *ab initio* calculations, MEAM and the EAM-FS potential at 0 K and the corresponding percentage errors for the values predicted by the interatomic potentials with respect to the values from *ab initio* calculations.

Elastic constants (GPa)	<i>ab initio</i> calculations [23]	MEAM	EAM-FS
C_{11}	169	145 (14%)	206 (22%)
C_{12}	138	128 (7%)	136 (1%)
C_{44}	40	78 (95%)	47 (18%)

Table 2.4: Elastic constants of B19' from *ab initio* calculations, MEAM and the EAM-FS potential at 0 K and the corresponding percentage errors for the values predicted by the interatomic potentials with respect to the values from *ab initio* calculations.

Elastic constants (GPa)	<i>ab initio</i> calculations [23]	MEAM	EAM-FS
C_{11}	223	211 (5%)	299 (34%)
C_{12}	129	64 (50%)	223 (73%)
C_{13}	99	101 (2%)	340 (243%)
C_{15}	27	50 (85%)	165 (511%)
C_{22}	241	235 (3%)	1087 (351%)
C_{23}	125	108 (14%)	420 (236%)
C_{25}	-9	-17 (89%)	116 (1388%)
C_{33}	200	194 (3%)	620 (210%)
C_{35}	4	17 (325%)	310 (7650%)
C_{44}	76	93 (22%)	260 (242%)
C_{46}	-4	-16 (300%)	-131 (3175%)
C_{55}	21	50 (138%)	204 (871%)
C_{66}	77	20 (74%)	85 (10%)

From Eq. (2.1) it can be observed that, under compression along $\langle 100 \rangle_{B2}$, the error in the transformation strain predicted by the MEAM and the EAM-FS potential is a direct consequence of the errors in a_m and a_0 predicted by both potentials. Similarly, Eq. (2.2) suggests that the error in the transformation strain under tension along $\langle 100 \rangle_{B2}$ depends on the errors in b_m , c_m , and a_0 . Table 2.2 lists the percentage error in the lattice constants predicted by both potentials. Although the EAM-FS potential predicts a slightly more accurate value of the constant a_0 , the errors associated with the B19' lattice constants a_m , b_m and c_m are significantly higher than those related to the MEAM potential. Hence this leads to more accurate predictions of the transformation strains with the MEAM potential. Apart from the above-mentioned lattice constants associated with B19', the other noticeable difference from Table 2.2 is that the monoclinic angle β of B19' is less accurately predicted by the MEAM potential. For the $\langle 100 \rangle_{B2}$ orientation chosen for this study, Eqs. (2.1) and (2.2) show that the transformation

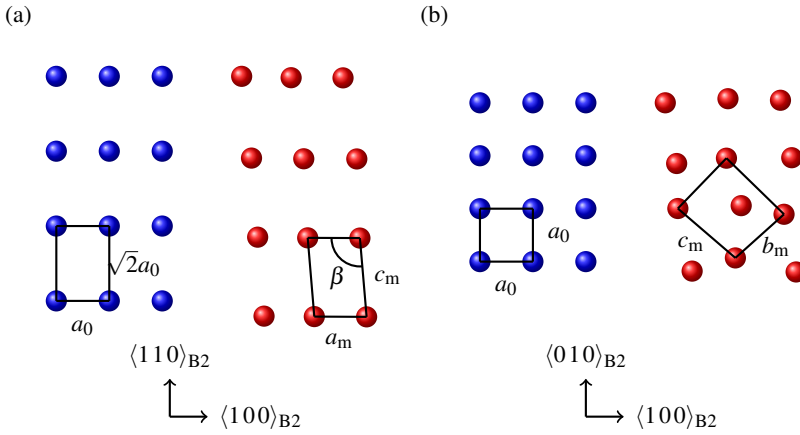


Figure 2.5: Visualization of the B19' structure obtained from MD simulations of B2 under uniaxial (a) compression and (b) tension along the $\langle 100 \rangle_{B2}$ direction using the MEAM potential. Only a few Ni atoms are shown for clarity. The blue dots represent Ni atoms in the initial B2 structure and the red dots represent Ni atoms in the B19' structure obtained upon loading B2. The same B19' crystal is also formed using EAM but with different a_m , b_m , c_m and β corresponding to that potential (shown in Table 2.2).

strains are independent of β . Therefore, the effect of the predicted value of β on the pseudo-elastic behavior along a generic loading direction cannot be assessed by performing simulations only along $\langle 100 \rangle_{B2}$. This will be discussed in further detail in a future work. The reason behind the better performance of the MEAM potential in predicting the transformation strains is therefore attributable to the better prediction of the lattice constants.

An analogous argument holds for the calculation of the Young's modulus of the initial B2 phase along the $\langle 100 \rangle$ direction and the Young's modulus of the tensile and compressive B19' variants that are formed. Table 2.5 (fourth, fifth and sixth columns) lists these values computed using *ab initio* values of the elastic constants and the elastic constants predicted by the MEAM and the EAM-FS potential listed in Tables 2.3 and 2.4. The Young's modulus values of the B2 and B19' phases previously computed using MD simulations with the MEAM and EAM-FS potential in Table 2.1 are similar to the values obtained from the elastic constants predicted by both interatomic potentials. The differences arise because of the

Table 2.5: Transformation strains calculated by applying the LDM (Eqs. (2.2), (2.1)) to experimental lattice constants (first row) and to the lattice constants predicted by the MEAM and the EAM-FS potential (third and fourth row); Young's modulus of the B2 phase and the B19' variants (Eqs. (2.3) and (2.4)) calculated using elastic constants from *ab initio* simulations and those predicted by the MEAM and the EAM-FS potential.

	$\epsilon_{\text{trans}}^{\text{tens}}$ (%)	$\epsilon_{\text{trans}}^{\text{comp}}$ (%)	E_{B2} (GPa)	$E_{\text{B19}'}^{\text{tens}}$ (GPa)	$E_{\text{B19}'}^{\text{comp}}$ (GPa)
experiments	2.662	4.201			
<i>ab initio</i> simulations			43	180	115
MEAM potential	3.514	4.032	25	141	122
EAM-FS potential	0	0.001	94	101	95

different temperature, as explained above. From Table 2.1 it can be concluded that the initial B2 Young's modulus along the $\langle 100 \rangle_{\text{B2}}$ direction and the Young's modulus of the B19' variants that are formed under tension and compression are also more accurately predicted by the MEAM potential. By arguments similar to those used for the transformation strain, the ability of the MEAM potential to predict elastic constants more accurately than the EAM-FS potential makes it more suited to the estimation of the Young's modulus for the B2 and B19' phases along any other orientation.

We have demonstrated that the better prediction capabilities of the MEAM potential for the transformation strain and Young's modulus, key aspects of the pseudo-elastic behavior, are due to the lower percentage errors in the estimation of the lattice and elastic constants compared to the EAM-FS potential as indicated in Tables 2.2, 2.3 and 2.4. While our discussion focused on the study of pseudo-elasticity along one particular orientation, the observation about the differences in the lattice and elastic constants has direct implications for all the other orientations. Despite the MEAM prediction of lattice and elastic constants is in average more accurate, some of these values are quite inaccurate and might lead to incorrect results along some orientations. Nevertheless, the MEAM potential appears to be the most suited potential for a study of pseudo-elasticity in NiTi. This is fundamentally important for modeling pseudo-elasticity in polycrystalline NiTi SMAs where the behavior along different orientations dictates the overall mechanical response.

As a final remark, it is worth noting that the phase transformation behavior is affected by the temperature at which the loading simulations are performed. In fact, the initial B2 phase softens as the temperature decreases whereas the final B19' phase softens as the temperature increases. Apart from the modulus, the transformation stress is higher and the transformation strain lower when

the loading simulation is performed at a higher temperature. Although not addressed in this study, the influence of temperature is captured accurately in the MD simulations and will be discussed in a forthcoming publication.

REFERENCES

- [1] P. Srinivasan, L. Nicola, and A. Simone, *Modeling pseudo-elasticity in NiTi: Why the MEAM potential outperforms the EAM-FS potential*, Computational Materials Science **134**, 145 (2017).
- [2] W.-S. Ko, B. Grabowski, and J. Neugebauer, *Development and application of a Ni-Ti interatomic potential with high predictive accuracy of the martensitic phase transition*, Physical Review B **92**, 134107 (2015).
- [3] D. Mutter and P. Nielaba, *Simulation of the shape memory effect in a NiTi nano model system*, Condensed Matter and Materials Science **577**, S83 (2013).
- [4] Y. Zhong, K. Gall, and T. Zhu, *Atomistic study of nanotwins in NiTi shape memory alloys*, Journal of Applied Physics **110**, 033532 (2011).
- [5] C. Frick, S. Orso, and E. Arzt, *Loss of pseudoelasticity in nickel-titanium sub-micron compression pillars*, Acta Materialia **55**, 3845 (2007).
- [6] J. Ye, R. K. Mishra, A. R. Pelton, and A. M. Minor, *Direct observation of the NiTi martensitic phase transformation in nanoscale volumes*, Acta Materialia **58**, 490 (2010).
- [7] J. S. Juan, M. L. No, and C. A. Schuh, *Nanoscale shape-memory alloys for ultrahigh mechanical damping*, Nature Nanotechnology **4**, 415 (2009).
- [8] K. Bhattacharya and R. D. James, *The material is the machine*, Science **307**, 53 (2005).
- [9] M. Kohl, *Shape Memory Microactuators* (Springer, 2004).
- [10] T. Saburi and S. Nenno, *The shape memory effect and related phenomena*, Proceedings of the International Conference on Solid-Solid Phase Transformations, 1455 (1981).
- [11] T. E. Buchheit and J. A. Wert, *Predicting the orientation-dependent stress-induced transformation and detwinning response of shape memory alloy single crystals*, Metallurgical and Materials transactions A **27A**, 269 (1996).
- [12] M. Finnis and J. Sinclair, *A simple empirical n-body potential for transition metals*, Philosophical Magazine A **50**, 45 (1984).

- [13] W. Lai and B. Liu, *Lattice stability of some NiTi alloy phases versus their chemical composition and disordering*, Journal of Physics: Condensed Matter **12**, L53 (2000).
- [14] J. H. Rose, J. R. Smith, F. Guinea, and J. Ferrante, *Universal features of the equation of state of metals*, Physical Review B **29**, 2963 (1984).
- [15] Y.-M. Kim, B.-J. Lee, and M. I. Baskes, *Modified embedded-atom method interatomic potentials for Ti and Zr*, Physical Review B **74**, 014101 (2006).
- [16] B.-J. Lee, *A modified embedded-atom method interatomic potential for the Fe-C system*, Acta Materialia **54**, 701 (2006).
- [17] S. J. Plimpton, *Fast parallel algorithms for short-range molecular dynamics*, Journal of Computer Physics **117**, 1 (1995).
- [18] T. Schneider and E. Stoll, *Molecular-dynamics study of a three-dimensional one-component model for distortive phase transitions*, Physical Review B **17** (1978).
- [19] H. Berendsen, J. Postma, W. van Gunsteren, A. DiNola, and J. Haak, *Molecular-dynamics with coupling to an external bath*, Journal of Chemical Physics **81** (1984).
- [20] D. H. Tsai, *The virial theorem and stress calculation in molecular dynamics*, Journal of Chemical Physics **70**, 1375 (1979).
- [21] L. Brinson, I. Schmidt, and R. Lammering, *Stress-induced transformation behavior of a polycrystalline NiTi shape memory alloy: Micro and macro-mechanical investigations via in situ optical microscopy*, Journal of Mechanics and Physics of Solids **52**, 1549 (2004).
- [22] Y. Zhong, K. Gall, and T. Zhu, *Atomistic characterization of pseudoelasticity and shape memory in NiTi nanopillars*, Acta Materialia **60**, 6301 (2012).
- [23] M. F.-X. Wagner and W. Windl, *Lattice stability, elastic constants and macroscopic moduli of NiTi martensites from first principles*, Acta Materialia **56**, 6232 (2008).
- [24] J. D. Honeycutt and H. C. Andersen, *Molecular dynamics study of melting and freezing of small Lennard-Jones clusters*, Journal of Physical Chemistry **91**, 4950 (1987).

- [25] K. Gall, H. Sehitoglu, R. Anderson, I. Karaman, Y. I. Chumlyakov, and I. V. Kireeva, *On the mechanical behavior of single crystal NiTi shape memory alloys and related polycrystalline phenomenon*, Materials Science and Engineering **317**, 85 (2001).
- [26] S. Mao, J. Luo, Z. Zhang, M. Wu, Y. Liu, and X. Han, *EBSDB studies of the stress-induced B2-B19' martensitic transformation in NiTi tubes under uniaxial tension and compression*, Acta Materialia **58**, 3357 (2010).
- [27] H. Sehitoglu, R. Hamilton, D. Canadinc, X. Y. Zhang, K. Gall, I. Karaman, Y. Chumlykov, and H. J. Maier, *Detwinning in NiTi alloys*, Metallurgical and Materials transactions A **34A**, 5 (2003).
- [28] O. Matsumoto, S. Miyazaki, K. Otsuka, and H. Tamura, *Crystallography of martensitic transformation in TiNi single crystals*, Acta Materialia **35**, 2137 (1987).
- [29] T. Saburi, M. Yoshida, and S. Nenno, *Deformation behaviour of shape memory TiNi crystals*, Scripta Metallurgica **18**, 363 (1984).
- [30] J. Turley and G. Sines, *The anisotropy of Young's modulus, shear modulus and Poisson's ratio in cubic materials*, Journal of Physics D: Applied Physics **4**, 264 (1971).
- [31] S. Qiu, B. Clausen, S. A. P. II, R. D. Noebe, and R. Vaidyanathan, *On elastic moduli and elastic anisotropy in polycrystalline martensitic NiTi*, Acta Materialia **59**, 5055 (2011).
- [32] J. Wang and H. Sehitoglu, *Martensitic modulus dilemma in monoclinic NiTi-theory and experiments*, International Journal of Plasticity **61**, 17 (2014).
- [33] K. M. Knowles and D. A. Smith, *The crystallography of the martensitic transformation in equiatomic nickel-titanium*, Acta Metallurgica **29**, 101 (1981).

3

ORIENTATION-DEPENDENT PSEUDO-ELASTICITY

Pseudo-elasticity in NiTi shape-memory alloy single crystals depends on the loading direction. Here, we present a comprehensive study in which molecular dynamics simulations of austenitic bulk single crystals under strain-controlled tensile and compressive loading along the $\langle 110 \rangle$, $\langle 111 \rangle$, and $\langle 100 \rangle$ directions are performed, and the mechanical response of the crystals are contrasted. All simulations are performed using the MEAM interatomic potential proposed by Ko et al., 2015 [2]. The transformation strains and the Young's modulus of the initial austenitic and the final martensitic phases are compared with values obtained from the lattice deformation model and experimental results from the literature. Results show that depending on orientation the transformation occurs either through the formation of martensitic Lüders bands or through the transient formation of a multivariant martensite which, upon reorientation, becomes a dominant final single variant.

Simulations are also performed to assess the orientation-dependent behavior of nano-wires subjected to bending, since the flexibility of the wires is orientation dependent.

3.1. INTRODUCTION

A peculiarity of shape-memory alloy single crystals is their orientation-dependent pseudo-elastic behavior [3–6]. It is therefore crucial to be able to determine the best possible orientation for a specific application. Here, we perform MD simulations of tensile and compressive loading of three differently-oriented austenitic nickel-titanium (NiTi) shape-memory alloys (SMAs) at 350 K and assess their performance. We also perform bending simulations of NiTi nano-wires in the same orientations to assess the orientation dependence of the bending behavior.

Equi-atomic NiTi SMAs are increasingly being considered for use in actuation and mechanical damping in nano- and micro- devices [5–7] due to their pseudo/super-elastic behavior. This feature stems from the ability of the alloy to exist in more than one phase depending on temperature and stress. Austenite is the high-temperature parent phase and has a cubic B2-type crystal structure. When an external load is applied at a high temperature, above the martensitic start temperature, the B2 phase transforms into the monoclinic B19' martensitic phase, thereby accommodating deformations up to 10%. Upon removal of the external load, the material transforms back into the B2 phase and regains its initial shape manifesting its pseudo-elastic behavior.

This deformation behavior during a stress-induced martensitic transformation has been experimentally shown to depend on the orientation of the initial B2 crystal in micrometer size single-crystal specimens [8–12] and can be explained with the lattice deformation model (LDM) [13, 14]. The final variant of martensite formed upon loading depends on the loading direction with respect to the initial B2 crystal, thereby causing a difference in the deformation behavior. Single-crystal SMA devices at the nano- and micro-scale can benefit from the higher transformation strains along certain orientations of the alloy. Since the direction-dependent behavior for a single crystal can be easily determined through simulations, atomistic simulation techniques such as molecular dynamics (MD) can be used to optimize the design of SMA devices by predicting the best orientation of the crystal for a given application. Prior to doing this, it becomes necessary to analyze and validate the SMA pseudo-elastic behavior under tension and compression predicted by MD simulations along various orientations.

Nano-structural changes and deformation behavior during pseudo-elasticity along certain orientations in bulk and nano-size specimens have been already shown through atomistic simulations by different groups and using different potentials; a complete picture with the same system and potential is however missing and will be provided in this study. *Zhong et al.* [15] observed a reversible B2-

B19' transformation in $4.8 \text{ nm} \times 5 \text{ nm}$ sized NiTi nano-pillars using the Finnis-Sinclair interatomic potential [16]. Their study was restricted to the compressive behavior of a $\langle 110 \rangle$ oriented B2 nano-pillar. Wang *et al.* [17] also used the Finnis-Sinclair potential to simulate cyclic compressive loading on $\langle 110 \rangle$ oriented nano-pillars and observed changes in the mechanical response with increasing cycles. More recently, Ko *et al.* [2] simulated the compressive stress-induced B2-B19' transformation in a nano-pillar with a $10.7 \text{ nm} \times 10.7 \text{ nm}$ cross-section. The pillar was loaded along the $\langle 001 \rangle_{\text{B2}}$ direction at 450 K to validate their newly developed modified embedded-atom method (MEAM) interatomic potential. Wang *et al.* [18] also performed similar simulations under adiabatic condition using the MEAM potential to study super-elasticity under compressive loading along $\langle 001 \rangle_{\text{B2}}$. In these works, the analysis has been restricted only to compressive loading along one orientation of the initial B2 phase. The MEAM potential has also been used to demonstrate phase transformation in NiTi polycrystals subjected to a single compressive [19] and cyclic compressive [20] loading. In the previous chapter, we have shown [21] that the MEAM potential [2] is more suited than the Finnis-Sinclair [15, 22] to study pseudo-elasticity in single-crystal NiTi because of its ability to predict lattice and elastic constants more accurately. Hence, we use the MEAM potential to provide a comprehensive analysis of the elastic response of bulk NiTi under tensile and compressive loading before, during, and after phase transformation at different temperatures.

Three different initial orientations of bulk single-crystal austenite are considered in this contribution (Section 3.2) where tensile and compressive loading simulations are performed at 350 K. Results, shown in Section 3.3, indicate the directions along which the transformation strains are highest. The transformation strain values and the modulus of the initial and final phases are compared to experimentally known values and those obtained from the lattice deformation model [13, 14]. The effect of temperature on the transformation behavior is examined by performing the same set of simulations at 400 K and 450 K. To determine the effect of the orientation dependence on an ideal actuator device, MD simulations of bending of nano-wires are also carried out and discussed in Section 3.4.

3.2. METHODOLOGY

MD simulations of the stress-induced martensitic transformation in NiTi are carried out using the MEAM interatomic potential [2]. The MEAM potential, which also takes angular interactions into account, captures the directionality in the metallic bonds more effectively than other potentials, making it the

most suitable to predict phase transformation. The formulation of the MEAM potential and the parameters for NiTi can be found in the work of *Ko et al.* [2] and are not reported here. The potential predicts the martensitic start (M_s) and the austenitic finish (A_f) temperatures as 270 K and 490 K, respectively.

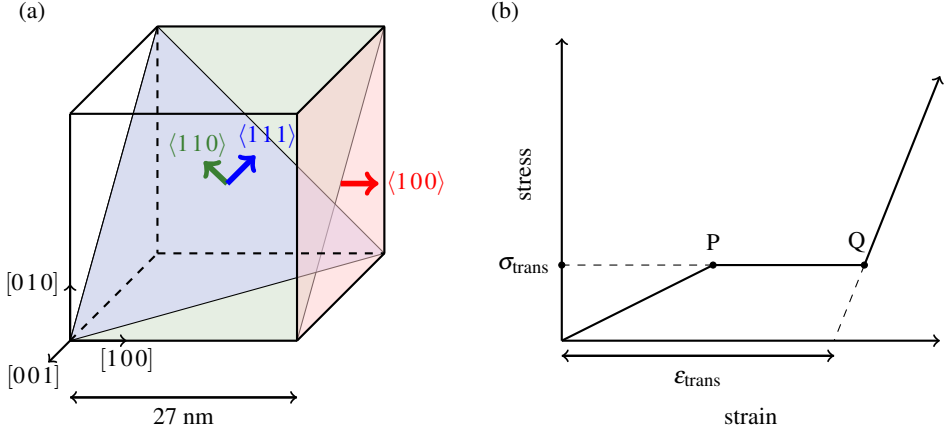


Figure 3.1: (a) Schematic representation of the austenite crystal; the arrows indicate the different loading directions chosen for this study. (b) Representation of the typical austenitic-to-martensitic deformation behavior. The transformation strain and stress are indicated by ϵ_{trans} and σ_{trans} , respectively. Point P (Q) denotes the beginning (end) of the martensitic transformation.

MD simulations of bulk NiTi are performed using LAMMPS [23] with the Nosé-Hoover [24] pressure and temperature control; the time integration is carried out using a velocity-Verlet algorithm [25] with a timestep of 0.5 fs. The initial structure is the ordered B2 phase, and three different loading directions are considered: $\langle 110 \rangle$, $\langle 111 \rangle$ and $\langle 100 \rangle$. Three periodic cubic simulation boxes, with faces normal to one of the loading directions are created and filled with atoms. Initially, an energy minimization run is performed using the conjugate gradient method to obtain the stress-free configuration of B2. Next, the simulation is run for 200,000 steps at zero stress and 350 K until the system is relaxed. This temperature is chosen since it is greater than the martensitic start temperature M_s , and B2 can therefore exist as the stable phase. Isothermal uniaxial displacement-controlled tension/compression is applied through a constant strain rate of 10^6 s^{-1} along the loading direction. During loading, the average stresses over other surfaces are maintained at 0 MPa to allow for the simulation box shape and size to change. The deformation behavior is described by plotting the virial stress [26] on the x -plane in the x -direction against the corresponding engineering strain component. The size of the simulation box is increased in

steps, and the above process is repeated for each box size until convergence of the stress-strain plot which is found to occur for a $27 \times 27 \times 27 \text{ nm}^3$ box. This size is therefore chosen as representative for bulk behavior and used to obtain the results discussed in the next section. A schematic representation of the initial system is shown in Fig. 3.1(a).

The mechanical behavior during a B2-B19' phase transformation is characterised by the moduli of the initial B2 phase and the final B19' phase and the corresponding transformation stresses and strains, as shown in Fig. 3.1(b). The stress at which the initial austenitic phase deviates from the initial linear elastic slope, denoted by point P in Fig. 3.1(b), is defined as the transformation stress σ_{trans} . The B2-B19' transformation progresses until the entire crystal is converted to the martensitic phase (point Q in Fig. 3.1(b)) and continues with its elastic deformation. When the martensitic elastic loading part of the curve is extended to the horizontal axis (null stress level), the corresponding strain is defined as the transformation strain ϵ_{trans} at that particular temperature. The difference in stress-strain behavior in the phase transformation region during strain-controlled and stress-controlled loading was discussed in the previous chapter. Here, we perform strain-controlled loading to study the nano-structural evolution during the B2-B19' transformation. A stress plateau is not expected during the transformation because the transformation is neither instantaneous nor complete at the transformation strain. The uniaxial loading simulations are repeated at 400 K and 450 K where the stress-induced transformation occurs. For each case, five different realizations with random initial atomic velocities are considered, and the stress and strain values are reported as average values.

3.3. RESULTS

3.3.1. LOADING IN $\langle 110 \rangle$ -DIRECTION

Here, MD results of tensile and compressive stress-induced transformation along $\langle 110 \rangle$ are shown for the first time using a MEAM interatomic potential. Figure 3.2 shows the stress-strain curves obtained by loading the B2 phase at 350 K along $\langle 110 \rangle$ in tension and compression. In both cases, the initial B2 structure deforms elastically until the transformation stress is reached, at points A' and D' in tension and compression, respectively, after which the B2-B19' transformation begins. The stress-strain behavior is observed to be different in tension and compression in the phase transformation region. In tension, a non-linear decrease in stress takes place from point A' till point B; this is followed by an increase to point B' after which there is another decrease in stress till point B'', followed by

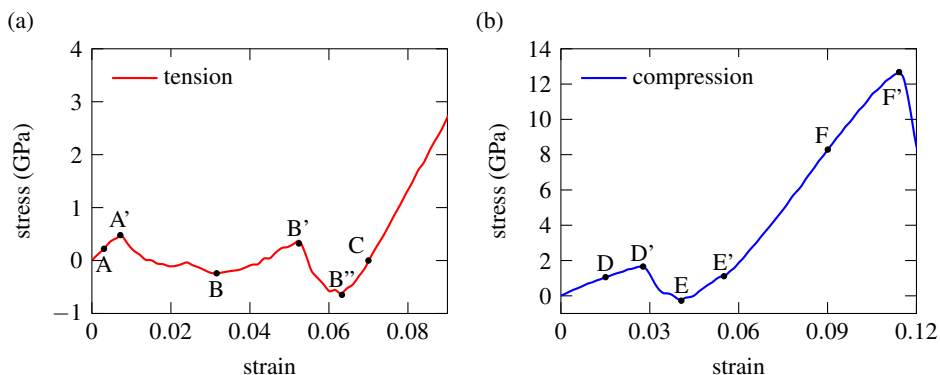


Figure 3.2: Isothermal stress-strain behavior of bulk NiTi under tensile (a) and compressive (b) loading along the $\langle 110 \rangle_{B2}$ direction at $T = 350 K$.

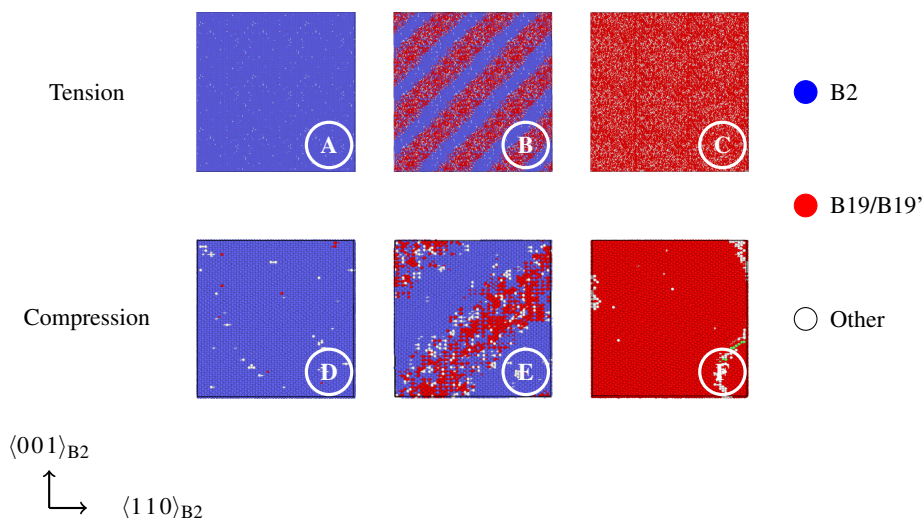


Figure 3.3: Sectional view of NiTi bulk cut along the $\langle 1\bar{1}0 \rangle_{B2}$ plane colored according to the common neighbor analysis (CNA) pattern. Blue atoms represent B2, red atoms represent B19/B19', and white atoms represent those that are neither B2 nor B19'. Refer to Fig. 3.2 for the labels A to F.

a linear increase in stress. Upon analyzing the structural changes in the crystal, it is observed that the first decrease in stress after A' occurs due to the transformation from B2 to an orthorhombic B19 intermediate phase. This intermediate B19 phase has also been observed by [Zhong et al. \[27\]](#) and [Ko et al. \[2\]](#) during MD simulations of stress-induced B2-B19' transformation. Notice that this is a displacement controlled simulation and, while the strain is increased, the over-

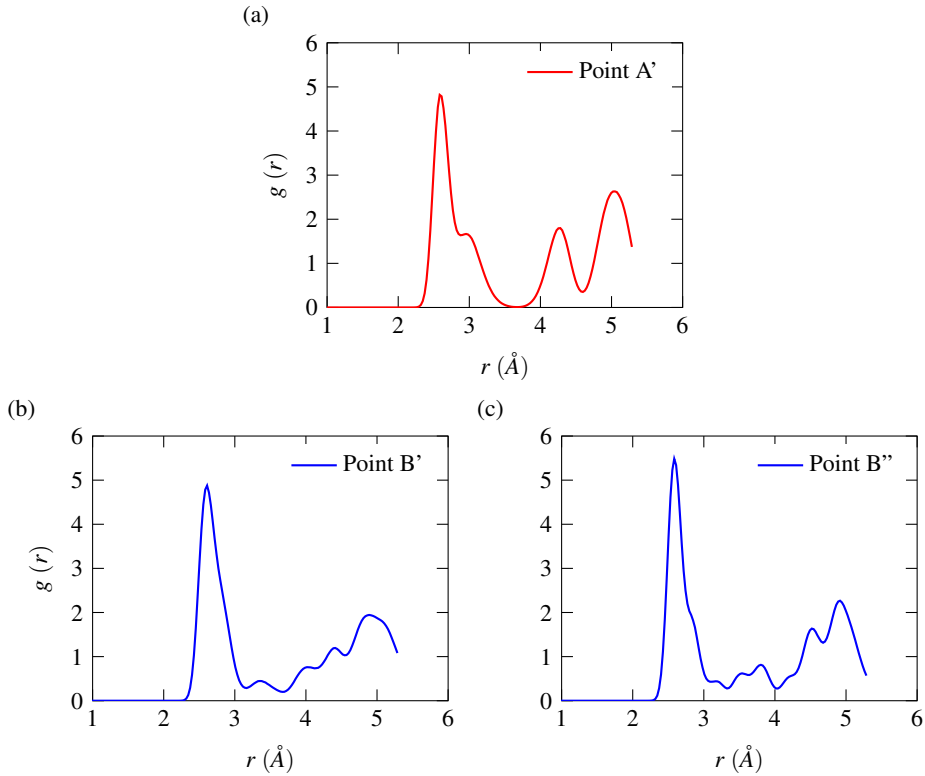


Figure 3.4: The radial distribution function (RDF) plots corresponding to points A', B' and B'' to differentiate between the B2, B19 and the B19' phases.

all state of tension in the crystal can revert to compression as a consequence of phase transformation. The applied strain until transformation is such that the crystal is under tension, but the elongation caused by the transformation would exceed (if unconstrained) the imposed elongation and, therefore, gives rise to a compressive stress state. The B19 that forms initially after point A is compressively strained in comparison to its relaxed structure, therefore there is a decrease in stress while more and more austenite transform into martensite. Up to point B, this decrease in stress due to the B2-B19 transformation is more pronounced than the increase in stress due to the loading of untransformed B2, thereby causing an overall non-linear decrease in stress. After point B, the increase in stress due to the loading of already transformed B19 becomes more pronounced than the decrease in stress due to the B2-B19 transformation. Upon further straining, the intermediate B19 phase transforms into the monoclinic B19' phase causing another decrease in stress till point B''. Again, although a tensile loading has led

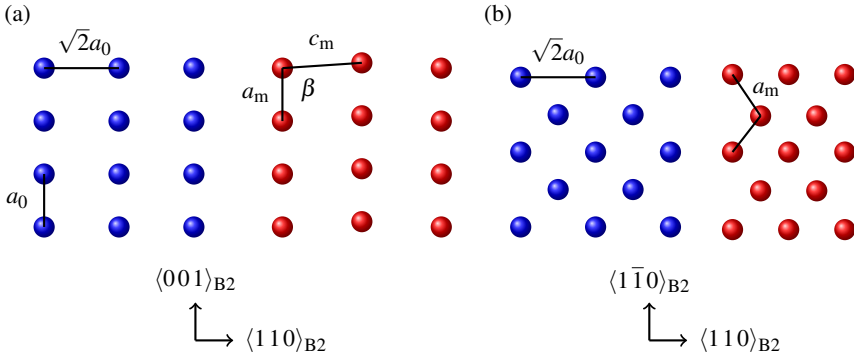


Figure 3.5: Visualisation of the B19' structure obtained from MD simulations of B2 under uniaxial (a) tension and (b) compression along the $\langle 110 \rangle_{B2}$ direction. Only a few Ni atoms are shown for clarity. The blue dots represent Ni atoms in B2 and red dots represent Ni atoms in the final B19' structure. The lattice parameters of the two phases are given by a_0 , a_m , b_m , c_m and β .

to the transformation of the B2 to the B19' phase, the martensite that is formed at point B'' is still compressively strained compared to its relaxed structure, thereby leading to an overall compressive stress. After point B'' the martensite deforms elastically, reaches a fully relaxed structure at point C, and continues to deform in the B19' phase. In contrast, compressive loading involves only one load decrease during the beginning of the transformation (at point D'). Here, the B2 phase directly transforms into the B19' phase. Hence, the transformation region is characterized by a combination of decrease in stress due to the B2-B19' transformation and increase in stress due to the elastic deformation of the untransformed B2 and the transformed B19'.

In both cases, at large strain levels and beyond the non-linear region, the B2-B19' transformation is complete (points B'' and E' in tension and compression, respectively) and is followed by the elastic deformation of B19'. This continues until a strain level of 14.5% (11.5%) in tension (compression). The transformation strain in tension is higher than in compression, whereas the transformation stress in compression is higher. The Young's modulus of the B2 and B19' phases along the $\langle 110 \rangle_{B2}$ direction can be obtained from the slopes of the elastic loading branches. Figure 3.2(b) shows that the Young's modulus of the B2 phase is 80.3 GPa and that of the B19' phase formed under tensile (compressive) loading is 132 (218) GPa. In comparison to the previous work by [Zhong et al. \[27\]](#), the Young's modulus values of the two phases and the transformation strain ob-

tained here are closer to experimentally known values, as discussed later. In addition, the asymmetry between tensile and compressive behavior is captured. Since the orientation of B19' with respect to the initial B2 structure is different under tension and compression, the Young's modulus is also different.

Figure 3.3 shows sectional views of the bulk, cut along the $\langle 1\bar{1}0 \rangle_{B2}$ plane, subject to tension and compression, with atoms depicted according to the common neighbor analysis (CNA) pattern. The CNA pattern differentiates the B2 and the B19' phases, but is not able to differentiate between the intermediate B19 and the B19' phases. Atoms with B2 structure are represented in blue and atoms with B19/B19' structure are represented in red. Points A, B and C along the tensile curve and points D, E and F along the compressive curve in Fig. 3.2 are chosen for representation: one along the initial linear elastic loading of B2, one along the B19' elastic loading, and one in between, where the transformation occurs. From Fig. 3.3, it is observed that MD simulations predict the B2-B19 transformation in tension and the B2-B19' transformation in compression to progress through the formation of Lüders-like bands along the $\langle 11\bar{2} \rangle_{B2}$ direction. The width of the bands increases with the strain until the entire bulk is transformed into B19 (B19') in tension (compression). Lüders-like bands have also been experimentally observed during stress-induced transformation in NiTi [28] and in previous MD simulations of stress-induced transformations in NiTi [22, 27]. To differentiate between B19 and B19' phases, three points along the tensile curve (points A', B' and B'') are chosen and the radial distribution function (RDF) at these points is depicted in Fig. 3.4. The peaks in Fig. 3.4(a) correspond to the peaks of the B2 phase (at point A'), which has a cubic structure. B2 (BCC) has fewer neighbor shells in comparison to the B19 or the B19' phase, and hence the RDF has fewer peaks as compared to the other two RDF's. By comparing Figs. 3.4(b) and 3.4(c), it is noted that the RDF corresponding to point B'' has additional peaks in between 3 Å and 4 Å. This arises due to the extra neighbor shells created due to an additional shear in the monoclinic B19' crystal structure (at point B'') in comparison to the orthorhombic B19 crystal structure (at point B'), thereby differentiating the two phases.

The B19' that forms at the end of the tensile and compressive loadings is oriented differently with respect to the initial B2 crystal, as shown in Fig. 3.5. Only few Ni atoms are visualized to clearly illustrate the difference in the final B19' variant. The difference in orientation of the monoclinic structure is what leads to the tension-compression asymmetry associated with the transformation. During loading of B2 along any particular orientation, the final martensite variant is formed in such a way that the transformation strain is highest along that partic-

ular orientation. For instance, in Fig. 3.5(a), the B19' variant that is formed produces the highest tensile transformation strain along $\langle 110 \rangle$. Similarly, the variant in Fig. 3.5(b) causes the highest compressive transformation strain. Since the MEAM potential is able to predict the correct variant, and also accurate lattice parameters, it naturally estimates transformation strain values close to experimentally known values along all orientations. This will be discussed later.

The stress decrease at the end of the elastic deformation of B19' in compression, denoted by F' in Fig. 3.2(b), occurs due to a B19'-BCO transformation. Although not shown in Fig. 3.2(a), this is also observed in tension at a strain level of 14.5%. BCO twins with a $\{001\}$ twin plane are formed in tension and twins with a $\{110\}$ twin plane are formed in compression. The increase in load makes the B19' phase unstable and leads to its transformation into the BCO phase, thereby releasing the accumulated strain energy. The BCO twins have indeed been theoretically proved to be the most energetically favourable at high strains in $\langle 110 \rangle_{B2}$ oriented NiTi [29]. Further discussion regarding the BCO phase is beyond the scope of this study.

Similar MD simulations of compressive stress-induced B2-B19' transformation along $\langle 110 \rangle$ have been performed earlier by Zhong *et al.* [27] with an EAM-Finnis-Sinclair type interatomic potential. They observe an intermediate B19 phase until a strain of 5.8%, and the B19-B19' transformation occurs till a strain of 6.6%, after which further loading leads to martensitic plasticity. The B19' phase existing over such a small strain range is unrealistic and the transformation strains are also not predicted accurately. The MEAM interatomic potential used in this study removes these drawbacks, in addition to predicting pseudo-elastic behavior along other orientations as well.

3.3.2. LOADING IN $\langle 111 \rangle$ -DIRECTION

The second orientation chosen for this study is $\langle 111 \rangle$. MD simulations of the stress-induced transformation of B2-B19' along this orientation have been performed for the first time. The B2-B19' transformation under tension occurs through a different mechanism in comparison to the other loading directions chosen for this study. Unlike the other cases, this tensile stress-induced transformation occurs through the formation of a multi-variant martensite followed by a martensitic reorientation within the structure leading to a dominant variant at the end of the transformation. Martensitic reorientation has been noticed earlier in experiments [30], but never observed numerically during a B2-B19' transformation of a single crystal. A more pronounced asymmetry between tensile and compressive behavior as compared to the other cases (see Fig. 3.6).

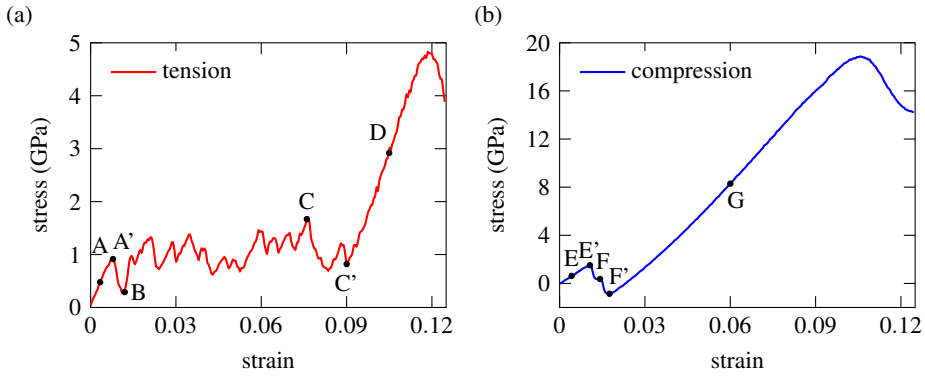


Figure 3.6: Isothermal stress-strain behavior of bulk NiTi under tensile (a) and compressive (b) loading along the $\langle 111 \rangle_{B2}$ direction at $T = 350 K$.

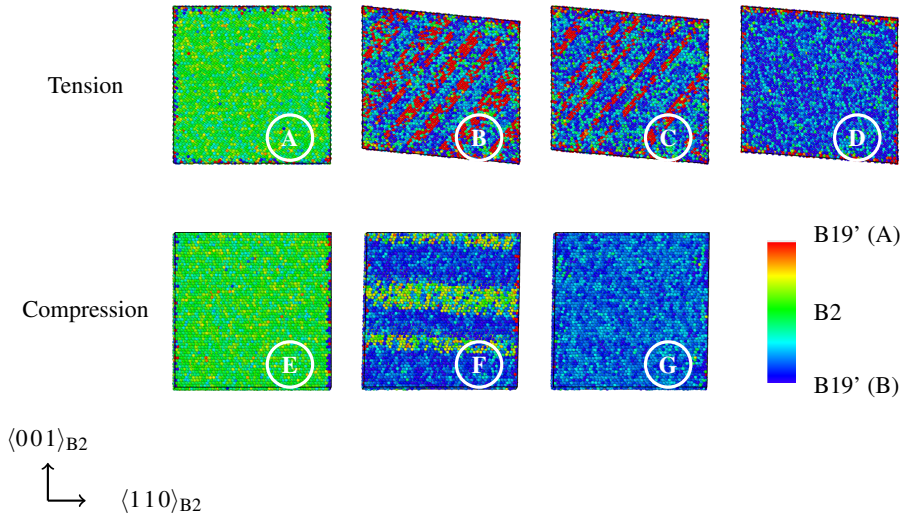


Figure 3.7: Sectional view of NiTi bulk cut along the $\langle 1\bar{1}0 \rangle_{B2}$ plane colored according to the local order parameter (bottom-right). Green atoms represent B2 and red and blue atoms represent different variants of B19'. Refer to Fig. 3.6 for labels A to G. Martensitic bands are observed only during tensile stress-induced transformation.

The modulus of the B2 phase along $\langle 111 \rangle_{B2}$ is estimated as 125 GPa, and the modulus of the final B19' variant in tension (compression) is 159.2 (242) GPa. The results also indicate that the transformation strain in tension is much higher than that in compression, and the transformation stress is smaller in tension. The region between points A' and C' corresponding to the tensile stress-induced

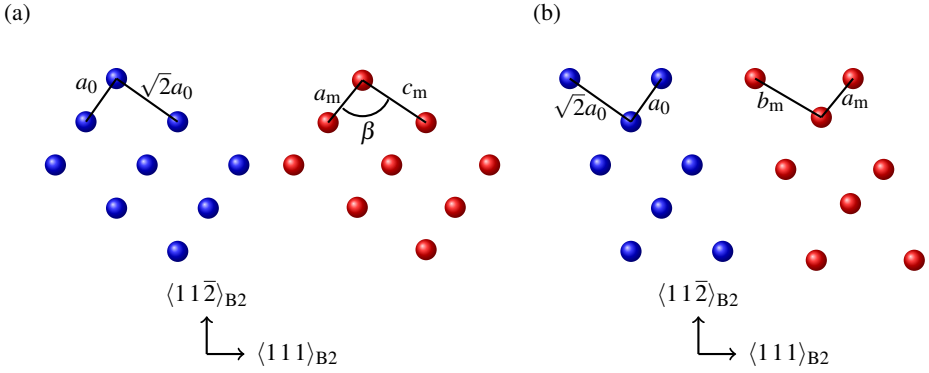


Figure 3.8: Visualisation of the B19' structure obtained from MD simulations of B2 under uniaxial (a) tension and (b) compression along the $\langle 111 \rangle_{B2}$ direction. Only a few select Ni atoms are shown for clarity. The blue dots represent Ni atoms in B2 and red dots represent Ni atoms in the final B19' structure. The lattice parameters of the two phases are given by a_0 , a_m , b_m , c_m and β .

phase transformation has a large number of fluctuations as compared to the $\langle 110 \rangle$ and $\langle 100 \rangle$ cases which arise due to the reorientation. In the other cases, a single variant pair of martensite grew through the initial B2 bulk during the transformation. When a tensile loading is applied along the $\langle 111 \rangle_{B2}$ orientation, MD predicts a different transformation mechanism of B2 to B19'. The initial elastic deformation of B2 is followed by a decrease in stress that corresponds to the B2-B19' transformation. At point B, a multi-variant B19' structure is formed. Upon further straining, martensitic reorientation occurs where one variant of martensite outgrows the other throughout the bulk until a single variant B19' is formed. During this stage, the stress-strain behavior is characterized by a combination of decrease in stress caused by one variant transforming into another, and stress increase due to the deformation of transformed B19', thereby leading to a number of kinks in the transformation region. This is followed by the elastic deformation of that favorable B19' single variant. Since the CNA pattern cannot differentiate between B19' variants, the sectional views of bulk NiTi cut along the $\langle 1\bar{1}0 \rangle_{B2}$ in Fig. 3.7 are depicted according to a per-atom local order parameter (LOP) that was developed by Mutter and Nielaba [31] to differentiate between B2 and B19' phases in NiTi. The color coding for the LOP is also shown in Fig. 3.7. Atoms colored in red and blue belong to two different B19' variants,

whereas atoms in green are in the B2 structure. Figure 3.7 shows that B2 is transformed into a multi-variant B19' at point B. The variant colored in blue grows throughout the entire bulk as the strain increases until it is completely transformed into a single-variant B19' as shown by the image depicting point D. This is not observed under compressive loading along $\langle 111 \rangle_{B2}$ where the initial B2 transforms into the final B19' variant through a band formation as seen in Fig. 3.7. The smaller transformation strain during compression, as compared to that during tension, does not allow for accommodation of multi-variant formation. Visualizing a few Ni atoms, Fig. 3.8 shows the different B19' variants formed under tension and compression and the difference across orientations. Again, these variants are formed in such a way that they produce the maximum transformation strain while loading B2 along $\langle 111 \rangle$. Similar to the $\langle 110 \rangle_{B2}$ case, the decrease in stress after the elastic deformation of B19' occurs due to a B19'-BCO transformation. Instead of BCO twins that were formed in the $\langle 110 \rangle_{B2}$ case, here a single variant BCO is formed.

3.3.3. LOADING IN $\langle 100 \rangle$ -DIRECTION

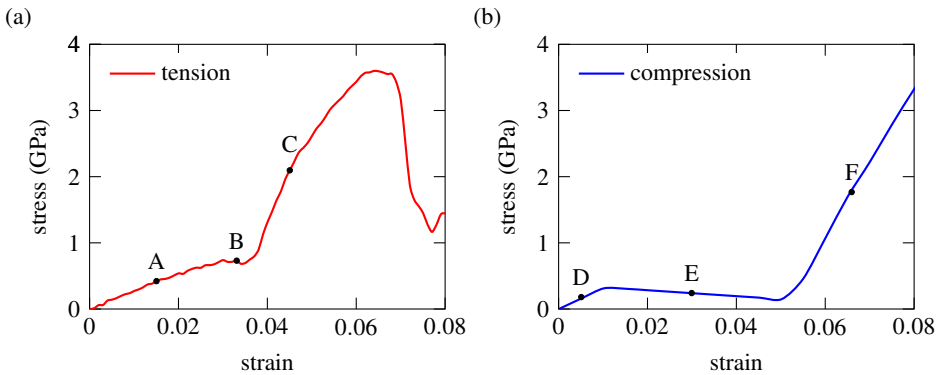


Figure 3.9: Isothermal stress-strain behavior of bulk NiTi under tensile (a) and compressive (b) loading along the $\langle 100 \rangle$ direction at $T = 350$ K.

The stress-induced martensitic transformation behavior when bulk B2 is loaded along $\langle 100 \rangle_{B2}$ has been discussed in the previous chapter where results along this particular orientation were used to reveal the better performance of the MEAM interatomic potential over the Finnis-Sinclair potential. The results have been reproduced here in order to compare them with the $\langle 110 \rangle$ and $\langle 111 \rangle$ cases. Figure 3.9 shows the stress-strain curve under tension and compression at 350 K. The strain gain obtained during the transformation, negligible under

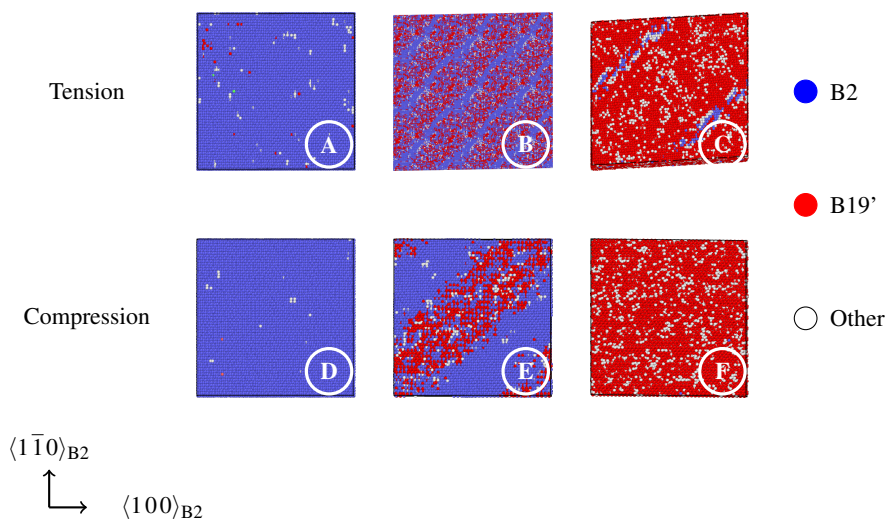


Figure 3.10: Sectional view of NiTi bulk cut along the $\langle 1\bar{1}0 \rangle_{B2}$ plane coloured according to the common neighbor analysis (CNA) pattern. Blue atoms represent B2, red atoms represent B19' and white atoms represent those that are neither B2 nor B19'. Refer to Fig. 3.9 for the labels A to F.

tension, is more significant under compression. Here, contrary to the previous case with loading direction $\langle 110 \rangle_{B2}$, the transformation strain is higher under compression, and the transformation stress is higher under tension. The Young's modulus of the B2 phase is different because the loading occurs along a different direction and the modulus of the B19' phase is also different because a different variant has formed.

Lüders-like bands are observed during the martensitic transformation also for this orientation, but along the $\langle 120 \rangle_{B2}$ plane in tension and in compression (see Fig. 3.10). Figure 3.11 shows some selected Ni atoms in the initial B2 and the final B19' variants. Further details regarding the transformation strains and the modulus of both phases can be found in the previous chapter. The dissimilarities seen in the mechanical behavior across these orientations are summarized and validated next.

3.3.4. DISCUSSION

MD simulations using the MEAM interatomic potential can numerically predict the deformation behavior before, during, and after the stress-induced martensitic phase transformation along three different loading directions of the initial austenitic single crystal. The strain-controlled nature of loading also helps identify the different transformation mechanisms along these loading directions. Fig-

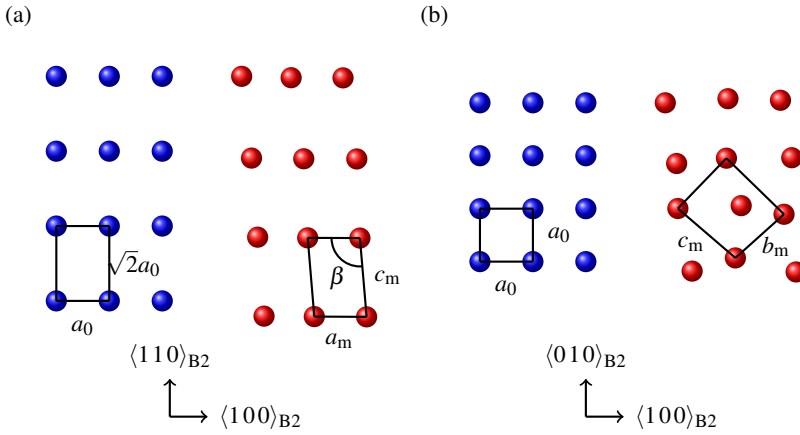


Figure 3.11: Visualisation of the B19' structure obtained from MD simulations of B2 under uniaxial (a) compression and (b) tension along the $\langle 100 \rangle_{B2}$ direction. Only a few Ni atoms are shown for clarity. The blue dots represent Ni atoms in the initial B2 structure and the red dots represent Ni atoms in the B19' structure obtained upon loading B2. The lattice parameters of the two phases are given by a_0 , a_m , b_m , c_m and β .

ure 3.12 directly compares the MD results of the stress-strain behavior under tension and compression along all the directions considered in this study. An orientation dependence is observed in the transformation stress, the transformation strain, and the elastic modulus of the B2 and the B19' phases. There is tension-compression asymmetry along all directions due to the different final martensite variant that forms under tension and under compression. To further compare the behavior across the three orientations, the values obtained from MD simulations at 350 K are listed in Tables 3.1 and 3.2 for tensile and compressive loading, respectively. For any application that exploits the pseudo-elastic property of NiTi, the transformation strain is a crucial aspect that needs to be considered. In this regard, the $\langle 111 \rangle$ orientation shows the highest transformation strain (8.6%) under tension among the orientations chosen for this study. Under compression, the $\langle 110 \rangle$ and $\langle 100 \rangle$ show higher transformation strain than the $\langle 111 \rangle$ orientation with almost similar values of 4.95% and 5.05%, respectively.

The Young's modulus of the B2 crystal computed from MD results ranges between 25 GPa and 125 GPa depending on the loading direction. These values

are slightly smaller than those obtained experimentally by Brill *et al.* [32] probably because the simulations are at 350 K, whereas the experiments were performed at 400 K, and B2 is known to soften upon cooling [33]. The austenitic phase B2, being a symmetric crystal, has the same Young's modulus in tension and compression; the same does not hold for B19', a monoclinic crystal that can exist in any of its 24 variants. This has led to difficulties in finding accurate experimentally-calculated values for martensite. Values in the literature range from 80 to 300 GPa [33–35]), which is the range the MD results of B19' modulus lie in.

A direct comparison of the MD simulations results to experimental values cannot be made here. The simulations are performed on single crystals at 350 K, whereas experimental data on mechanical properties during the B2-B19' phase transformation in single crystals are scarce and at different temperatures. Hence, in the next section, the numerical results of the transformation strain and modulus are compared and validated using values calculated from 0 K ab initio data.

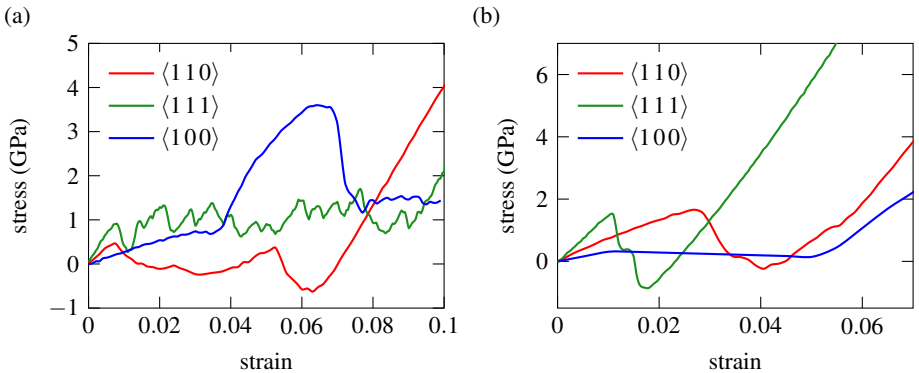


Figure 3.12: Isothermal stress-strain behavior of bulk NiTi under tensile (a) and compressive (b) loading along all the directions chosen for this study at $T = 350$ K.

Table 3.1: Comparison of the transformation stress, the transformation strain and the modulus of austenite and martensite phase obtained by performing MD simulations of uniaxial tensile stress-induced austenite-to-martensite transformation along the three orientations at 350 K.

	σ_{tr} (MPa)	ϵ_{tr}^{MD} (%)	E^{B2} (GPa)	$E^{B19'}$ (GPa)
$\langle 110 \rangle$	427	7.1	80.3	132
$\langle 111 \rangle$	760	8.6	125	159.2
$\langle 100 \rangle$	729	2.7	31.4	121.3

Table 3.2: Comparison of the transformation stress, the transformation strain and the modulus of austenite and martensite phase obtained by performing MD simulations of uniaxial compressive stress-induced austenite-to-martensite transformation along the three orientations at 350 K.

	σ_{tr} (MPa)	ϵ_{tr}^{MD} (%)	E^{B2} (GPa)	$E^{B19'}$ (GPa)
$\langle 110 \rangle$	1520	4.95	80.3	218
$\langle 111 \rangle$	1400	2.42	125	242
$\langle 100 \rangle$	330	5.05	31.4	111.3

3.3.5. VALIDATION OF MD RESULTS

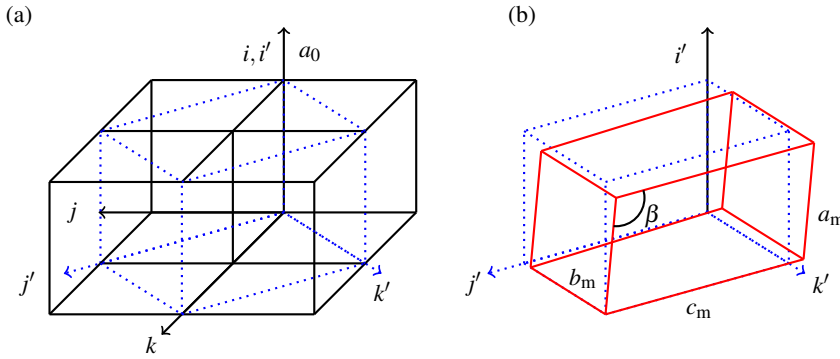


Figure 3.13: Schematic of the B2-B19' lattice deformation in NiTi [36]: (a) (i, j, k) represent the B2 reference frame; i', j' and k' lie along the $[001]$, $[110]$ and $[\bar{1}10]$ direction of the reference frame; B2 is represented by blue dotted lines viewed in the (i', j', k') reference frame; (b) distortion of B2 (blue dotted lattice) to B19' (red lattice); the lattice constant of B2 is a_0 and the lattice constants of B19' are a_m , b_m , c_m and β .

Orientation-dependent transformation strains have been calculated in literature for a single NiTi unit cell using the lattice deformation model proposed by Saburi *et al.* [13]. These theoretical values are calculated using 0 K lattice constants of B2 and B19'. Figure 3.13 shows a schematic of the B2-B19' lattice deformation with a_0 , a_m , b_m , c_m and β as the lattice parameters of the two phases.

Based on the loading direction, a symmetric B2 crystal can transform into any one of the 12 equivalent B19' corresponding variants. The LDM indicates that the variant that produces the maximum transformation strain along that particular direction forms at the end of a transformation. The corresponding transformation strain along that particular direction can be calculated from the

lattice constants of the two phases. The martensitic variants formed at the end of various single-crystal loading experiments have been compared to and validated with those predicted by the LDM [8, 14]. There are differences in the transformation strain values since these experiments are not performed at 0 K, whereas the transformation strains using the LDM are calculated from 0 K lattice parameters.

The final B19' variants predicted by the MD simulations in this study (Figs. 3.5, 3.11 and 3.8) are not only identical in structure to those predicted by the LDM, but they are also oriented along the same directions. In Table 3.3, a comparison is made between the transformation strains obtained from MD simulations with theoretically calculated LDM values for the three orientations. The MD results agree to a good extent, with less than 30% difference between the predicted and theoretically calculated values. Since the transformation strain is a function of the lattice constants of the two phases, the difference between the LDM and MD values can be attributed to two reasons: 1) the LDM values are calculated from 0 K lattice constants, whereas the B2 and B19' phases in the simulations are at 350 K; and 2) the lattice parameters of B2 and B19' (at 0 K) predicted by the MEAM interatomic potential are not exactly the same as the ab initio values used in the LDM. The consequence of the difference in lattice parameters on the transformation strains has been discussed in the previous chapter.

Table 3.3: Comparison of theoretical transformation strains with those obtained from MD simulations.

ϵ_{trans} (%)	Tension			Compression		
	$\langle 110 \rangle$	$\langle 111 \rangle$	$\langle 100 \rangle$	$\langle 110 \rangle$	$\langle 111 \rangle$	$\langle 100 \rangle$
LDM [37]	8.3	9.7	2.7	5.1	3.5	4.2
MD - MEAM	7.1	8.6	2.7	4.95	2.42	5.05

When the B2 loading direction and the corresponding final variant of B19' are known, the modulus of the two phases can be calculated from elastic constants according to [35, 38]

$$(E_{hkl}^{B2})^{-1} = S_{11} - 2 \left(S_{11} - S_{12} - \frac{1}{2} S_{14} \right) (n_1^2 n_2^2 + n_2^2 n_3^2 + n_1^2 n_3^2) \quad (3.1)$$

and

$$\begin{aligned} (E_{hkl}^{B19'})^{-1} = & n_1^4 S_{11} + 2n_1^2 n_2^2 S_{12} + 2n_1^2 n_3^2 S_{13} + 2n_1^3 n_3 S_{15} \\ & + n_2^4 S_{22} + 2n_2^2 n_3^2 S_{23} + 2n_1 n_2^2 n_3 S_{25} + n_3^4 S_{33} \\ & + 2n_1 n_3^3 S_{35} + n_2^2 n_3^2 S_{44} + 2n_1 n_2^2 n_3 S_{46} + n_1^2 n_3^2 S_{55} + n_1^2 n_2^2 S_{66}, \end{aligned} \quad (3.2)$$

where n_1 , n_2 and n_3 are cosines of the angles between the direction normal to the (hkl) plane and the lattice vectors of B2 and B19', respectively, and S_{ij} are the components of the compliance matrix. Wagner and Windl [34] have performed 0 K ab initio calculations and estimated the values of the three elastic constants of B2 and the 13 elastic constants of B19'. The modulus of B2 along $\langle 110 \rangle$, $\langle 100 \rangle$ and $\langle 111 \rangle$ and the six B19' structures (three in tension and three in compression) can hence be calculated using the values of elastic constants from Reference [34] in the above formulas. The modulus of the phases obtained from MD is compared with the theoretically calculated 0 K values in Table 3.4. The differences between the theoretical moduli and those obtained from MD simulations arise due to the same reasons discussed earlier for the differences in transformation strain values. The next section further describes the effect of temperature on the deformation behavior as predicted by MD simulations.

Table 3.4: Comparison of the 0 K theoretical modulus with those from MD simulations.

Modulus (GPa)	$\langle 110 \rangle$			$\langle 111 \rangle$			$\langle 100 \rangle$		
	E_{B2}	$E_{B19'}^{tens}$	$E_{B19'}^{comp}$	E_{B2}	$E_{B19'}^{tens}$	$E_{B19'}^{comp}$	E_{B2}	$E_{B19'}^{tens}$	$E_{B19'}^{comp}$
theory [34]	81	175	156	110	99	215	45	180	115
MD-MEAM	80.3	132	218	125	159.2	242	31.4	121.3	111.3

3.3.6. EFFECT OF TEMPERATURE

Uniaxial tensile and compressive loading simulations are also performed at 400 K and 450 K, temperatures at which NiTi exhibits pseudo-elastic behavior. Temperature does not affect the transformation mechanism in any of the three tensile or compressive loading directions, but has an effect on the transformation stress, the modulus of the two phases, and the transformation strain. The effect is the same for all the loading directions, and hence only two cases (one in tension and one in compression) are presented in Fig. 3.14. The trend observed here is observed for all other loading directions.

Figure 3.14 shows the variation of the stress-strain curve with temperature for tensile loading along $\langle 111 \rangle$ and compressive loading along $\langle 100 \rangle$. It is known that austenite softens mildly upon cooling, whereas martensite softens upon heating [33]. From Fig. 3.14 it is observed that the MD simulations capture this effect. The influence of temperature on the Young's modulus of the two phases has an effect also on the stress plateau and the transformation strain. The transformation strain along all orientations decreases as the temperature at which the loading is performed increases. The other noticeable trend is the increase in the

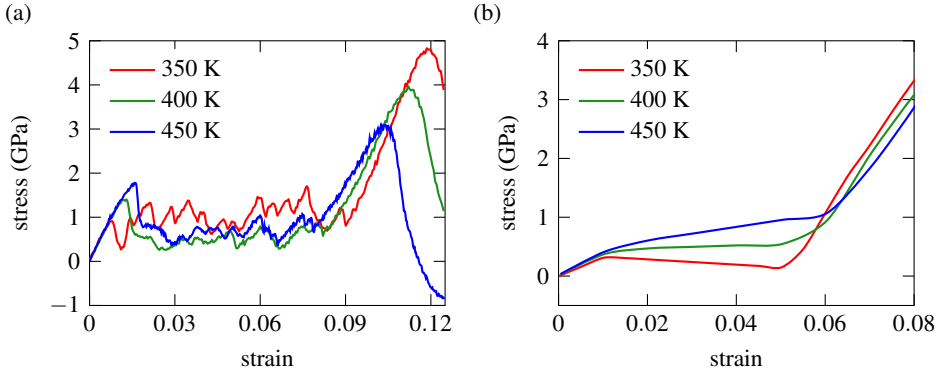


Figure 3.14: Isothermal stress-strain behavior of bulk NiTi under (a) tension along $\langle 111 \rangle_{B2}$ and (b) compression along $\langle 100 \rangle_{B2}$ at different temperatures.

transformation stress with increase in temperature. The temperature-dependent transformation stress obtained through MD simulations can be used as an input for the constitutive modeling of shape-memory alloys based on the phase transformation diagram [39].

3.4. NANO-WIRES UNDER BENDING

In various actuators and other electronic devices, a SMA component is subjected to bending. This type of loading enhances the effect of orientation dependence of the NiTi pseudo-elastic behavior, given that both tensile and compressive loading co-exist. To analyze this orientation dependence on the structural response, three differently-oriented single-crystal B2 nano-wires are chosen as shown in Fig. 3.15(a). These nano-wires are oriented in such a way that their lengths fall along the $\langle 110 \rangle_{B2}$, $\langle 111 \rangle_{B2}$ and $\langle 100 \rangle_{B2}$ directions. Results are shown for a 50 nm long wire with a 10 nm diameter (results similar to those reported here were also observed for larger nano-wires). After an energy minimization and thermal equilibration at 350 K, the wires are subjected to a bending load by imposing forces on atoms at the two ends of the wires (three unit cells) as shown in Fig. 3.15(b). At the end of every step, the force applied is the same on the three nano-wires. The simulations are performed at 350 K where stress-induced transformation occurs.

Figure 3.16 shows a sectional view of the evolution of the axial strain ϵ_{xx} along the length of the wire at five different stages of loading. When the wires are subjected to a bending load, the top part of the wire is stretched while the bottom part is compressed. This causes a stress-induced B2-B19' transformation in dif-

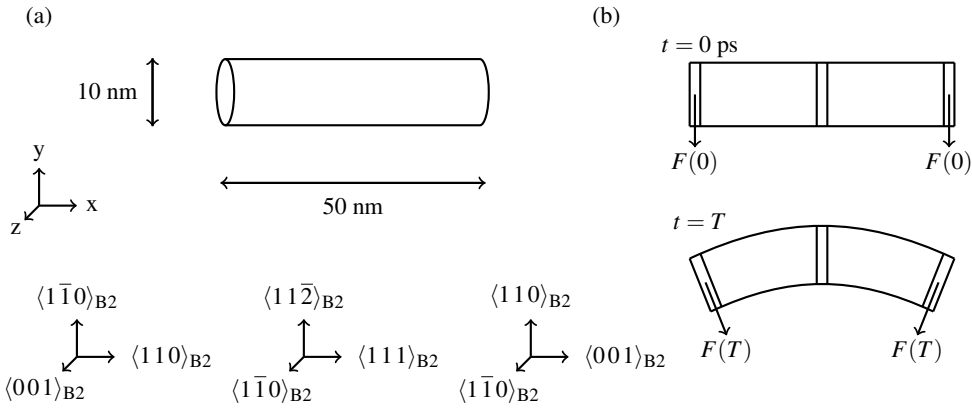


Figure 3.15: (a) Schematic of the $\langle 110 \rangle$, $\langle 111 \rangle$ and $\langle 100 \rangle$ oriented initial B2 nano-wires. (b) Schematic of the bending load applied to the nano-wires cut along the z -plane at the beginning of loading and at time T .

ferent regions of the wires, and the transformation can be identified through a sudden increase (or decrease) in the axial strain ϵ_{xx} that manifests as patches of different phases in Fig. 3.16. As expected, it is observed that the strain evolution is different in differently-oriented nano-wires. For instance, in the $\langle 110 \rangle$ and $\langle 111 \rangle$ oriented nano-wires, the tensile stress-induced transformation in the top part of the wires occurs before there is a transformation in the compressive region of the wire, as opposed to the $\langle 100 \rangle$ oriented nano-wire. This can also be visualized at time $t = t_4$ where a larger part of the $\langle 110 \rangle$ and $\langle 111 \rangle$ oriented wires has undergone tensile stress-induced transformation. Similarly, a very small part of the $\langle 111 \rangle$ oriented wire has undergone a compressive stress-induced transformation.

A few conclusions regarding the orientation dependence on the bending behavior can be drawn by correlating the transformation mechanism in the three wires during bending to the values listed in Tables 3.1 and 3.2. The B19' transformation stress in tension is lower than the transformation stress in compression along the $\langle 110 \rangle$ and $\langle 111 \rangle$ orientations when compared to the $\langle 100 \rangle$ orientation. This is directly mirrored by the strain evolution, where the tensile transformation (red patches) happens before the compressive transformation in the $\langle 110 \rangle$ and $\langle 111 \rangle$ nano-wires. The $\langle 111 \rangle$ oriented nano-wire shows the largest difference between the tensile- and the compressive-transformed parts due to

the pronounced asymmetry in transformation strain and stress under tension and compression along the $\langle 111 \rangle$ orientation as seen in Tables 3.1 and 3.2. From these tables, the compressive transformation stress along $\langle 111 \rangle$ is observed to be the highest among the six cases (three in tension and three in compression) and this is reflected in the strain evolution in the nano-wires, where the $\langle 111 \rangle$ oriented nano-wire is the wire with the least transformed compressed region. It is concluded that the strain evolution and the progression of transformation when single-crystal nano-wires are subjected to bending is a consequence of the orientation dependence of the single-crystal B2-B19' phase transformation.

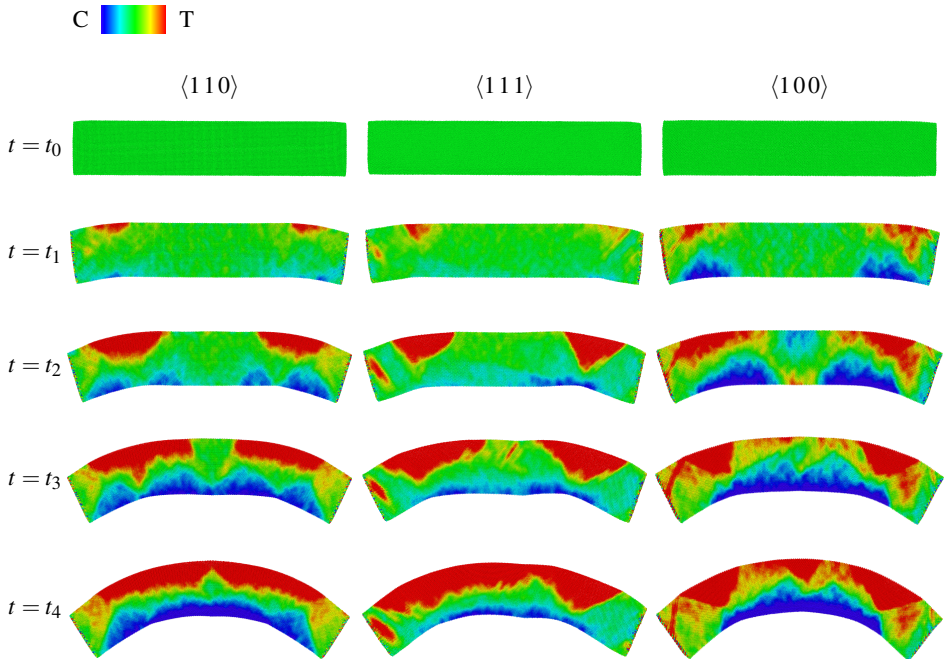


Figure 3.16: Evolution of the axial strain ϵ_{xx} during bending for the three nano-wires at five time steps. The forces are applied at the same rate.

Besides the differences observed in the strain evolution and progression of transformation, each of these nano-wires undergoes tensile and compressive stress-induced transformation in the top and bottom parts when subjected to

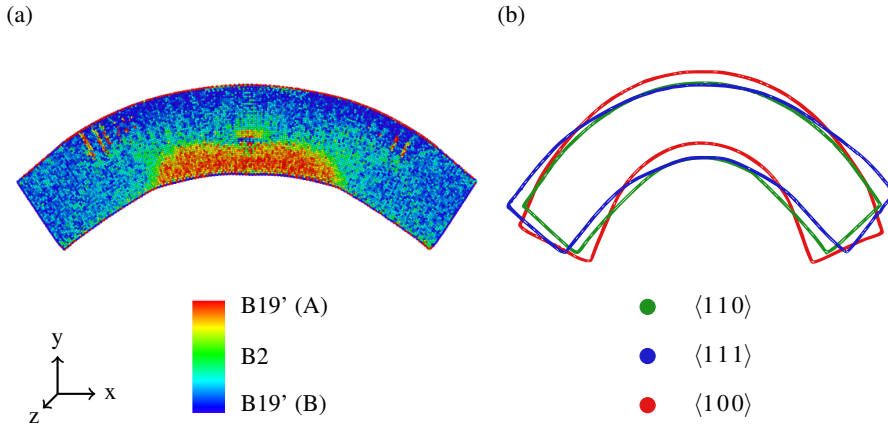


Figure 3.17: (a) Sectional view of the $\langle 110 \rangle_{B2}$ oriented wire during bending cut along the z -plane and coloured according to a local order parameter [31]. (b) Sectional views of the three nano-wires at the same load level cut along the z -plane and colored according to the initial orientation.

bending thus leading to different martensite variants formed in different parts of the wire. This can be further verified by viewing the nano-wires colored according to a local order parameter [31] as shown in Fig. 3.17(a). Here, only the $\langle 110 \rangle$ oriented nano-wire is shown at a particular time step. The blue colored atoms represent a tensile stress-induced variant and the red colored atoms represent a compressive stress-induced variant. A neutral zone is also seen in between these two regions where phase transformation has not occurred yet and the atoms are colored in green (B2). Similar difference in variants are also observed for the different regions in the other two nano-wires.

In this section, MD simulation results have been presented to show the orientation dependence in the bending behavior of NiTi nano-wires. When subjected to the same force (at any time step), the bending angle and the tip deformation of the nano-wire is different and depends on the initial orientation of the nano-wire as shown in Fig. 3.17(b). This is a result of the difference in variants in the tensile and compressive parts of the three wires, the difference in the progression of phase transformation, and eventually a difference in the strain in the top and bottom parts of the three wires. In this particular case, from Fig. 3.17(b), the $\langle 100 \rangle$ oriented nano-wire, which is the orientation along which

the compressive transformation strain is the largest and the tensile transformation strain is the smallest, shows the maximum bending as compared to the other two wires. In comparison, the $\langle 111 \rangle$ oriented nano-wire, which is the orientation with the least compressive transformation strain and the most tensile transformation strain, shows the least bending among the three wires when subjected to the same load. Although the exact values of bending forces and bending angles during different stages of loading have not been presented here, the crucial aspect to note is that the deformation behavior during bending is a direct consequence of the orientation dependence of the B2-B19' phase transformation in single-crystals.

3.5. CONCLUSIONS

In this study, MD simulations of uniaxial tensile and compressive loading of three differently-oriented bulk B2 NiTi have been performed. The results indicate a strong orientation dependence and tension-compression asymmetry arising primarily due to the different orientations of the monoclinic crystal structure of the B19' phase.

The MD results suggest that the production of single crystal NiTi SMAs can be optimised based on the transformation stress and transformation strain that are needed for a particular application. For instance, NiTi actuator devices that require large tensile stress-induced deformations can be made in such a way that the $\langle 111 \rangle$ orientation of the B2 single crystal falls along the loading axis. Similarly, a device that relies on compressive stress-induced transformation would benefit from a $\langle 110 \rangle$ or a $\langle 100 \rangle$ oriented NiTi single crystal. In the case of bending, one should take into account that the deformation does not occur homogeneously, the curvature of the bended crystal is not constant, and the neutral axis is offset from the center because of the tension-compression asymmetry.

This study also lays the basis for a better understanding of polycrystal behavior [19]. When a polycrystal is loaded, the local mechanical behavior will depend on the orientation of the grains. Transformation will begin earlier in favorably-oriented grains, and the evolution of the martensitic transformation will depend on the size and orientation of individual grains and on the way each grain will deform to accommodate the deformation of its neighbors.

The other noticeable difference in behavior for the three orientations is in the nano-structural changes associated with the phase transformation. Earlier MD simulations predicted the formation of Lüders-like B19' bands during pseudo-elastic behavior along the $\langle 110 \rangle$ orientation. In the simulations presented here, the martensitic transformation occurs through the formation of such bands

when the austenitic bulk is loaded both along the $\langle 110 \rangle$ or $\langle 100 \rangle$ orientation, whereas the transformation progresses through the formation of a multi-variant B19' structure and the subsequent reorientation into a single-variant B19' when loaded along the $\langle 111 \rangle$ orientation.

REFERENCES

- [1] P. Srinivasan, L. Nicola, and A. Simone, *Atomistic modeling of the orientation dependent pseudo-elasticity in NiTi: Normal loading and bending*, Computational Materials Science **154**, 25 (2018).
- [2] W.-S. Ko, B. Grabowski, and J. Neugebauer, *Development and application of a Ni-Ti interatomic potential with high predictive accuracy of the martensitic phase transition*, Physical Review B **92**, 134107 (2015).
- [3] C. Frick, S. Orso, and E. Arzt, *Loss of pseudoelasticity in nickel-titanium sub-micron compression pillars*, Acta Materialia **55**, 3845 (2007).
- [4] J. Ye, R. K. Mishra, A. R. Pelton, and A. M. Minor, *Direct observation of the NiTi martensitic phase transformation in nanoscale volumes*, Acta Materialia **58**, 490 (2010).
- [5] J. S. Juan, M. L. No, and C. A. Schuh, *Nanoscale shape-memory alloys for ultrahigh mechanical damping*, Nature Nanotechnology **4**, 415 (2009).
- [6] M. Kohl, *Shape Memory Microactuators* (Springer, 2004).
- [7] K. Bhattacharya and R. D. James, *The material is the machine*, Science **307**, 53 (2005).
- [8] O. Matsumoto, S. Miyazaki, K. Otsuka, and H. Tamura, *Crystallography of martensitic transformation in TiNi single crystals*, Acta Materialia **35**, 2137 (1987).
- [9] R. M. Manjeri, S. Qiu, N. Mara, A. Misra, and R. Vaidyanathan, *Superelastic response of [111] and [101] oriented micropillars*, Journal of Applied Physics **108** (2010).
- [10] K. Gall, H. Sehitoglu, R. Anderson, I. Karaman, Y. I. Chumlyakov, and I. V. Kireeva, *On the mechanical behavior of single crystal NiTi shape memory alloys and related polycrystalline phenomenon*, Materials Science and Engineering **317**, 85 (2001).
- [11] J. Pfetzinger-Micklich, R. Ghisleni, T. Simon, C. Somsen, J. Michler, and G. Eggeler, *Orientation dependence of stress-induced phase transformation and dislocation plasticity in NiTi shape memory alloys on the micro scale*, Materials Science and Engineering A **538**, 265 (2012).

- [12] G. Laplanche, J. Pfetzinger-Micklich, and G. Eggeler, *Orientation dependence of stress-induced martensite formation during nanoindentation in NiTi shape memory alloys*, *Acta Materialia* **68**, 19 (2014).
- [13] T. Saburi, M. Yoshida, and S. Nenno, *Deformation behaviour of shape memory TiNi crystals*, *Scripta Metallurgica* **18**, 363 (1984).
- [14] T. E. Buchheit and J. A. Wert, *Predicting the orientation-dependent stress-induced transformation and detwinning response of shape memory alloy single crystals*, *Metallurgical and Materials transactions A* **27A**, 269 (1996).
- [15] Y. Zhong, K. Gall, and T. Zhu, *Atomistic study of nanotwins in NiTi shape memory alloys*, *Journal of Applied Physics* **110**, 033532 (2011).
- [16] M. Finnis and J. Sinclair, *A simple empirical n-body potential for transition metals*, *Philosophical Magazine A* **50**, 45 (1984).
- [17] B. Wang, G. Z. Kang, Q. H. Kan, K. Zhou, and Y. Chao, *Molecular dynamics simulations to the pseudo-elasticity of NiTi shape memory alloy nano-pillar subjected to cyclic compression*, *Computational Materials Science* **131**, 132 (2017).
- [18] B. Wang, G. Z. Kang, Q. H. Kan, K. Zhou, and Y. Chao, *Atomistic study on the super-elasticity of single crystal bulk NiTi shape memory alloy under adiabatic condition*, *Computational Materials Science* **142**, 38 (2018).
- [19] W.-S. Ko, S. B. Maisel, B. Grabowski, J. B. Jeon, and J. Neugebauer, *Atomic scale processes of phase transformations in nanocrystalline NiTi shape-memory alloys*, *Acta Materialia* **123**, 90 (2017).
- [20] B. Wang, G. Z. Kang, Q. H. Kan, W. P. Wu, K. Zhou, and Y. Chao, *Atomistic study on the super-elasticity of nanocrystalline NiTi shape memory alloy subjected to a cyclic deformation*, *Computational Materials Science* **152**, 85 (2018).
- [21] P. Srinivasan, L. Nicola, and A. Simone, *Modeling pseudo-elasticity in NiTi: Why the MEAM potential outperforms the EAM-FS potential*, *Computational Materials Science* **134**, 145 (2017).
- [22] D. Mutter and P. Nielaba, *Simulation of the shape memory effect in a NiTi nano model system*, *Condensed Matter and Materials Science* **577**, S83 (2013).

- [23] S. J. Plimpton, *Fast parallel algorithms for short-range molecular dynamics*, Journal of Computer Physics **117**, 1 (1995).
- [24] S. Nose, *A unified formulation of the constant temperature molecular-dynamics methods*, Journal of Chemical Physics **81**, 511 (1984).
- [25] W. C. Swope, H. C. Anderson, P. H. Berens, and K. R. A. Wilson, *A computer simulation method for the calculation of equilibrium constants for the formation of physical clusters of molecules: Application to small water clusters*, Journal of Chemical Physics **76**, 637 (1982).
- [26] D. H. Tsai, *The virial theorem and stress calculation in molecular dynamics*, Journal of Chemical Physics **70**, 1375 (1979).
- [27] Y. Zhong, K. Gall, and T. Zhu, *Atomistic characterization of pseudoelasticity and shape memory in NiTi nanopillars*, Acta Materialia **60**, 6301 (2012).
- [28] G. Tan, Y. Liu, P. Sittner, and M. Saunders, *Lüders-like deformation associated with stress-induced martensitic transformation in NiTi*, Scripta Materialia **50**, 193 (2004).
- [29] T. Ezaz, H. Sehitoglu, and H. Maier, *Energetics of twinning in martensitic NiTi*, Acta Materialia **59**, 5893 (2011).
- [30] Y. Liu, Z. Xie, J. V. Humbeeck, L. Delaey, and Y. Liu, *On the deformation of the twinned domain in NiTi shape memory alloys*, Philosophical Magazine A **80**, 1935 (2000).
- [31] D. Mutter and P. Nielaba, *Simulation of thermally induced austenite phase transformation in shape memory alloy*, The European Physics Journal B **84**, 109 (2011).
- [32] T. M. Brill, S. Mittelbach, W. Assmus, M. Mullner, and B. Luthi, *Elastic properties of NiTi*, Journal of Physics: Condensed Matter **3**, 9621 (1991).
- [33] P. Sittner, L. Heller, J. Pilch, C. Curfs, T. Alonso, and D. Favier, *Young's modulus of austenite and martensite phases in superelastic NiTi wires*, Journal of Materials Engineering and Performance **23** (2014).
- [34] M. F.-X. Wagner and W. Windl, *Lattice stability, elastic constants and macroscopic moduli of NiTi martensites from first principles*, Acta Materialia **56**, 6232 (2008).

- [35] S. Qiu, B. Clausen, S. A. P. II, R. D. Noebe, and R. Vaidyanathan, *On elastic moduli and elastic anisotropy in polycrystalline martensitic NiTi*, *Acta Materialia* **59**, 5055 (2011).
- [36] S. Mao, J. Luo, Z. Zhang, M. Wu, Y. Liu, and X. Han, *EBSD studies of the stress-induced B2-B19' martensitic transformation in NiTi tubes under uniaxial tension and compression*, *Acta Materialia* **58**, 3357 (2010).
- [37] T. Saburi, Y. Watanabe, and S. Nenno, *Morphological characteristics of the orthorhombic martensite in shape memory Ti-Ni-Cu alloy*, *ISIJ International* **29**, 405 (1989).
- [38] J. Turley and G. Sines, *The anisotropy of Young's modulus, shear modulus and Poisson's ratio in cubic materials*, *Journal of Physics D: Applied Physics* **4**, 264 (1971).
- [39] S. Marfia and R. Rizzoni, *One-dimensional constitutive SMA model with two martensite variants: Analytical and numerical solutions*, *European Journal of Mechanics - A/Solids* **40**, 166 (2013).

4

A NEW POTENTIAL FOR NICKEL-TITANIUM

The reference-free version of the MEAM (RF-MEAM) potential provides more flexibility for fitting than the 2NN-MEAM because it also describes the pair potential as an explicit function. Here, we present a methodology to fit RF-MEAM potentials to DFT data. We then evaluate the performance of the fitted potential by comparing MD simulations with experimental and DFT data. The methodology is applied to a binary and a quaternary alloy, namely NiTi and NbMoTaW. For NiTi, our attention focuses on designing a potential that properly captures its mechanical behavior, given that the existing potentials fail to predict elastic constants in agreement with experiments. To reach our aim, we included the stress tensors of different high-temperature configurations in the fitting database. The obtained RF-MEAM outperforms existing EAM and MEAM potentials in predicting the lattice and elastic constants of austenitic and martensitic phases as well as the corresponding transformation temperatures. To demonstrate the suitability of this methodology also for more complex systems, a RF-MEAM potential is fitted to model the multi-component NbMoTaW high-entropy alloy. Validation is achieved through comparison between observables obtained through the MD output and ab initio data.

This chapter has been published in *Modelling and Simulation in Materials Science and Engineering* **27**, 6 (2019) [1]

4.1. INTRODUCTION

Interatomic potentials that reproduce *ab initio* data accurately are the most crucial ingredient of any molecular dynamics (MD) simulation. It is therefore of great importance to design potentials that satisfy this requirement. In this work, we have developed reference-free modified MEAM (RF-MEAM) potentials for the nickel-titanium (NiTi) shape-memory alloy and the NbMoTaW high-entropy alloy. We have then tested their performance by comparing results from MD simulations to data obtained through density functional theory (DFT) and experiments.

Since DFT simulations are restricted to a few hundred atoms due to the heavy computational burden, larger systems are usually modeled using molecular dynamics (MD) simulations, relying on interatomic potentials fitted to DFT data. The performance of an MD simulation clearly depends on the quality of the employed interatomic potential. Out of the many potential functions that have been developed, parametrized, and used to perform MD simulations of metals and metal alloys, the most recent and widely used formalisms are the embedded-atom method (EAM) [2] and the modified embedded-atom method (MEAM) [3, 4] interatomic potentials.

Parameters of any potential function are optimized by fitting them to DFT data. In the original MEAM [3, 4] formalism, which has been parametrized to represent a number of metals and metal alloys accurately, the interatomic potential is tied to a particular equilibrium reference structure. The pair interaction energy is calculated from known values of the total and embedding function energies in an equilibrium reference structure, with the total energy obtained analytically from the zero-temperature Rose universal equation of state [5]. In the RF-MEAM formalism, the potential is no longer bound to the Rose equation, and the pair interaction is instead defined as an explicit function, with parameters that can be optimized during the fitting process. The energies of any structure can hence be reproduced by fitting those parameters. This formalism is therefore termed the reference-free MEAM [6, 7] formalism because the dependency on the reference structure is removed.

In this work, we use *MEAMfit v2* [8], the latest version of the optimization code *MEAMfit* [9, 10] to perform the fitting. The optimized potential can then be directly used to perform MD simulations in LAMMPS. The fitting methodology to develop RF-MEAM potentials is applied to two systems: the equi-atomic nickel-titanium shape-memory alloy (SMA), and the multi-component niobium molybdenum tantalum tungsten (NbMoTaW) high-entropy alloy.

The NiTi SMA has been modeled so far either through the EAM Finnis-

Sinclair (EAM-FS) potential [11, 12] or the 2NN-MEAM [13–19] potential. The 2NN-MEAM potential was developed because of the difficulties in describing the complex B19' martensitic structure using the simple potential parametrization in the EAM formalism. The parameters for the 2NN-MEAM potential by Ko et al. [13] were obtained by fitting them to a database consisting primarily of properties related to the unary Ni and Ti systems with the addition of 0 K NiTi B2 and B19' structures. In Chapter 2, we have shown that the 2NN-MEAM performs better than EAM-FS in capturing the overall NiTi phase transformation since lattice and elastic constants of both phases are in better agreement with experimental data. There is however still room for improvement as some of the elastic constants of the martensitic phase differ by up to 300% (C_{35} and C_{46} in table 4.3) from experimental data. Since each elastic constant differs by a different percentage from the corresponding experimental data, this implies that the potential cannot predict the correct mechanical response in complex systems such as polycrystals. Moreover, the transformation temperatures (martensitic start M_s and austenitic finish A_f) are not captured accurately, and the structural energy differences predicted by DFT cannot be reproduced.

Here, we are interested in developing a potential that models the mechanical behavior of the B2 and B19' phases more accurately, in addition to predicting the reversible phase transformation. This can be achieved thanks to the flexibility of the RF-MEAM potential, where a broader dataset can be used for fitting, compared to the one used for 2NN-MEAM. The database used in this work comprises results of extensive DFT simulations of the B2 and B19' phases. In addition to the 0 K energies, finite temperature energies, atomic forces and stress tensors of 120 different configurations of B2 and B19' are included. It is mostly the addition of the stress tensors to the database that leads to a better prediction of the mechanical behavior of NiTi. Indeed, the newly developed RF-MEAM potential considerably improves the prediction of most of the 0 K lattice and elastic constants, and cohesive energies of both B2 and the B19' phases. We then perform MD simulations using the new RF-MEAM potential to model pseudo-elasticity and shape-memory behavior in single-crystal NiTi. The 0 K results are compared to the *ab initio* data used for fitting. The transformation temperatures, transformation strains, and elastic moduli of the two phases predicted by the RF-MEAM potential are compared to those predicted by the 2NN-MEAM potential. These results, along with the fitting details used for NiTi, are reported in Section 4.3.

The fitting methodology to build a potential, described in Section 4.2, can also be extended to a multi-component system. This is demonstrated in Section 4.4 for a NbMoTaW high-entropy alloy where observables from DFT are

compared with the MD output for a sample fitting set and a sample testing set. Improvements in *MEAMfit v2*, the LAMMPS implementation of the RF-MEAM potential and instructions on how to download the corresponding computer subroutines can be found in Appendix 4.A.

4.2. METHODOLOGY

4.2.1. THE RF-MEAM POTENTIAL

Reference-free versions of the MEAM potential have been developed and used earlier for Si by Timonova and Thijsse [7] and for Al-O by Lazic and Thijsse [6]. Scopece and Thijsse [20] also performed MD simulations for Al-O using the RF-MEAM potential. According to the formalism, the total energy of an N -atom system is given by

$$E = \sum_{i=1}^N E_i^{\text{emb}}(\rho_i) + \frac{1}{2} \sum_{i \neq j}^N \phi_{i,j}(r_{ij}), \quad (4.1)$$

where $E_i^{\text{emb}}(\rho_i)$ is the embedding energy function, ρ_i is the fictitious electron density at site i and $\phi_{i,j}(r_{ij})$ is the pair potential between atoms i and j separated by a distance r_{ij} . The embedding term is described as a function of the fictitious partial electron densities. The partial electron densities and the pair potentials are written as

$$f_i^{(l)}(r) = \sum_{n=1}^{N_1} a_i^{(n,l)} \left(r_i^{(n,l)} - r \right)^3 \theta \left(r_i^{(n,l)} - r \right), \quad (4.2)$$

and

$$\phi_{i,j}^{(l)}(r) = \sum_{n=1}^{N_2} b_{i,j}^{(n)} \left(s_{i,j}^{(n)} - r \right)^3 \theta \left(s_{i,j}^{(n)} - r \right). \quad (4.3)$$

Here, $a_i^{(n,l)}$, $b_{i,j}^{(n)}$, $r_i^{(n,l)}$, and $s_{i,j}^{(n)}$ ($l = 0, 1, 2, 3$) are parameters to be optimized. The number of terms in the summation (N_1 and N_2) should be chosen so that there are sufficient data-points per parameter to avoid over-fitting the potential. Fitting to larger datasets with higher N_1 and N_2 values results in more accurate potentials overall, but the fitting will take a longer time due to the greater number of parameters to optimize as well as the higher number of fitting points. In addition, choosing high N_1 and N_2 values also results in slower MD simulations since more calculations are involved per step. For instance, for both systems discussed in this article where we choose $N_1 = N_2 = 3$, a MD step using the RF-MEAM takes approximately twice the time per atom in comparison to a MD step using the 2NN-MEAM potential with the same cut-off.

4.2.2. FITTING METHODOLOGY INCLUDING STRESS TENSORS

Fitting is performed using *MEAMfit v2* [8], a potential optimization code that uses a conjugate-gradient minimizer paired with a genetic algorithm to obtain the best set of parameters [9]. As an example, the fitting database can be chosen to consist of energies, atomic forces and stress tensors of various configurations. The optimization function to be minimized during the fitting run is therefore given as

$$R^2 = \frac{\sum_n w_n \left(E_{\text{pot}}^{(n)} - E_{\text{DFT}}^{(n)} \right)^2}{\sum_n w_n \left(E_{\text{DFT}}^{(n)} - E_{\text{DFT}}^{\text{avg}} \right)^2} + \frac{\sum_{n,i,\beta} w_n \left(F_{\beta,\text{pot}}^{(n,i)} - F_{\beta,\text{DFT}}^{(n,i)} \right)^2}{\sum_{n,i,\beta} w_n \left(F_{\beta,\text{DFT}}^{(n,i)} - F_{\beta,\text{DFT}}^{\text{avg}} \right)^2} \quad (4.4)$$

$$+ \frac{\sum_n \sum_{\gamma} w_n \left(\sigma_{\gamma,\text{pot}}^{(n)} - \sigma_{\gamma,\text{DFT}}^{(n)} \right)^2}{\sum_n \sum_{\gamma} w_n \left(\sigma_{\gamma,\text{DFT}}^{(n)} - \sigma_{\gamma,\text{DFT}}^{\text{avg}} \right)^2},$$

where n runs over all structures in the fitting database. The subscript ‘pot’ (respectively ‘DFT’) refers to values calculated using the potential (respectively DFT). The quantities E , F_{β}^i , σ_{γ} , and w_n are the energies, the β component of the force on the i th atom, the γ component of the stress tensor, and the weight factors, respectively. Further details about the formalism and the fitting procedure can be found in reference [9].

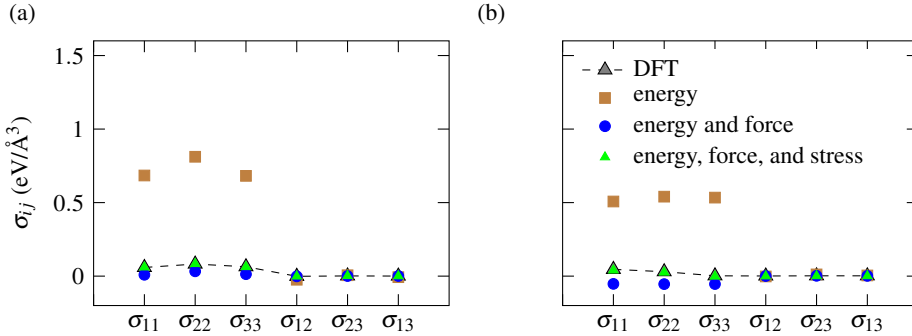


Figure 4.1: Comparison between DFT and predicted values of the stress tensor of the 54-atom NiTi (a) 500 K fitted B2 structure and (b) 300 K test B2 structure. The vertical axis indicates the value of every component of the stress tensor marked on the horizontal axis. The dashed line serves as visual aid to identify the DFT values.

Adding stress tensors to the fitting database is a key addition to the latest

version of the optimization code, the benefits of which are demonstrated in Figs. 4.1(a) and (b) that show stress tensor values of a 500 K B2 structure and a 300 K B2 structure predicted by potentials that are fitted only to energies, to energies and forces, and to energies, forces, and stress tensors of a 500 K B2 structure. The energies and forces predicted by the three potentials are found to be very close to the DFT values. The stress tensor is also predicted accurately for both fitted and test structures, however only by the potential for which the stress tensor was included in the fitting set. This example calculation, along with further details about Fig. 4.1, including a comparison of the energies and forces predicted by the potentials to the DFT values, is described in Appendix 4.B.

The result validates the importance of adding stress tensors to the fitting database to accurately capture the overall mechanical behavior. This procedure is followed in the development of the new RF-MEAM potential for NiTi as described in the next section.

4.3. A NEW RF-MEAM FOR NiTi

4.3.1. CONSTRUCTING THE DFT DATABASE

The DFT database built for fitting the RF-MEAM potential contains properties related to both the B2 and the B19' phases. The configurations include a 128-atom 0 K perfect B2 structure, a 108-atom 0 K perfect B19' structure, 60 500 K *ab initio* MD configurations each of 54-atom B2 and 32-atom B19', and 60 1,000 K *ab initio* MD configurations each of 54-atom B2 and 32-atom B19'. Configurations related to different temperatures for these phases are chosen to ensure transferability of the potential to predict B2 and B19' behavior as accurately as possible. DFT simulations are run using VASP [21] within the Perdew-Burke-Ernzerhof (PBE) generalized gradient approximation (GGA) [22] for the exchange correlation function. A cut-off energy of 450 eV for the plane wave basis set and the Methfessel-Paxton smearing method with a width of 0.1 eV is used. The chosen cut-off energy is a converged value above which the difference in stress tensors is less than 10^{-4} eV/Å³. A $23 \times 23 \times 23$ *k*-point mesh is selected for the B2 primitive unit cell and the same *k*-point density is used for other structures. Magnetism is included by considering spin-polarized calculations. *Ab initio* MD simulations are performed to obtain configurations at finite temperatures. In the first step, low convergence parameters are used to sample the configuration space effectively. MD runs with a single *k*-point are performed for 10,000 steps with a time step of 1.5 fs corresponding to ionic temperatures of 500 K and 1000 K. In the next step, 60 uncorrelated snapshots from each of these runs are extracted

and recalculated with the previously mentioned high convergence criteria and a denser k -point mesh, thereby providing more accurate values of energies, atomic forces, and stress tensors. This procedure generates 120 configurations each for B2 and B19'. The use of low parameters to efficiently sample the phase space, with subsequent higher parameters to obtain accurate observables, is identical to the upsampling approach within the “upsampled thermodynamic integration using Langevin dynamics” (UP-TILD) [23] method.

4.3.2. OPTIMIZATION OF THE RF-MEAM PARAMETERS

For the fitting procedure, three summation terms are chosen for the partial electron densities and the pair potential; equal weights are then assigned to the energies of the two 0 K structures and to the energies, atomic forces, and stress tensors of the 120, 500 K and 1,000 K configurations. This yields a total of 78 parameters of the RF-MEAM potential fitted to 32,642 data points. The parameters of the best-fitted potential are listed in table 4.C1 in Appendix 4.C and details regarding obtaining and using the best-fitted interatomic potential file for LAMMPS is described in Appendix 4.A.

The optimization function value R (see Eq. (4.4)) for the best-fitted set of parameters is 0.37. The RMS errors in energies, forces, and stresses of the configurations used in the fitting database calculated with the best-fitted set of parameters are 0.019 eV/atom, 0.226 eV/Å and 5.7 meV/Å³, respectively. Next, we report the results of molecular statics and molecular dynamics runs using this potential to verify its performance.

4.3.3. PERFORMANCE OF THE RF-MEAM POTENTIAL

Table 4.1 shows the lattice parameters of the B2 and B19' phases obtained by performing molecular statics calculations at 0 K using the RF-MEAM potential. The table also includes the volume and cohesive energy difference between the two phases. The values are compared to the results from *ab initio* calculations and those predicted by the 2NN-MEAM potential [13]. The percentage error of the values predicted by the RF-MEAM and the 2NN-MEAM is also specified—this is calculated as the difference between predicted and *ab initio* values with respect to the *ab initio* values. The monoclinic angle of B19' and the energy difference between the two phases are more accurately predicted by the newly developed RF-MEAM potential. The predicted value of the other lattice parameters and the volume difference between B2 and B19' are similar to those predicted by the previous 2NN-MEAM potential. Results from experiments [24] are also added to the table to demonstrate the accuracy of the *ab initio* values and the RF-MEAM pre-

dicted results.

Table 4.1: Comparison of lattice parameters of NiTi B2 and B19' (in Å), the monoclinic angle of B19' (in degrees), the atomic volume difference between B2 and B19' (in Å³) and the energy difference between B2 and B19' (in eV/atom) obtained from experiments, from current *ab initio* calculations, from the new RF-MEAM potential, and from the 2NN-MEAM potential. The percentage errors of the values predicted by the potentials ((predicted value – *ab initio* value) / *ab initio* value × 100) are also included in the table.

	experiments [24]	<i>ab initio</i> (this work)	RF-MEAM		2NN-MEAM [13]	
			value	error	value	error
a_{B2}	3.01	3.01	2.988	-0.7%	2.99	-0.7%
$a_{B19'}$	2.909	2.91	2.884	-0.9%	2.878	-1.1%
$b_{B19'}$	4.11	4.06	4.1	-0.98%	4.13	1.7%
$c_{B19'}$	4.657	4.68	4.655	-0.53%	4.659	-0.45%
$\beta_{B19'}$	97.9	98	97.1	-0.9%	99.4	1.5%
$\Omega_{B2} - \Omega_{B19'}$	0.14	0.14	0.13	7.1%	0.17	21.4%
$E_{B19'} - E_{B2}$	0.043	0.042	0.04	-4.8%	0.034	-19%

Tables 4.2 and 4.3 report a comparison between the elastic constants and the percentage error with respect to the *ab initio* values predicted by the RF-MEAM and the 2NN-MEAM potentials and the same quantities obtained from *ab initio* calculations for the B2 and the B19' phases. As evident from the values in the tables, the use of the RF-MEAM potential yields an improvement in terms of the overall prediction of elastic constants for both phases. Next we performed MD simulations with the RF-MEAM potential to analyze temperature- and stress-induced B2-B19' transformations in NiTi.

Table 4.2: Elastic tensor constants of NiTi B2 from *ab initio* calculations, RF-MEAM, and the 2NN-MEAM potential at 0 K and the corresponding percentage errors ((predicted value – *ab initio* value) / *ab initio* value × 100) for the values predicted by the interatomic potentials.

	<i>ab initio</i> [25]	RF-MEAM		2NN-MEAM	
	(GPa)	value (GPa)	error	value (GPa)	error
C_{11}	169	175	4%	145	14%
C_{12}	138	141	2.2%	128	7%
C_{44}	40	47	17.5%	78	95%

In all the MD simulations we have employed periodic boundary conditions, and time integration is performed using the velocity-Verlet algorithm [27] with a time step equal to 0.5 fs. Heating-cooling cycle and uniaxial loading of single-crystal B2 simulations are shown to illustrate temperature- and stress-induced phase transformations, respectively. Each MD simulation described below is re-

Table 4.3: Elastic tensor constants of NiTi B19' from *ab initio* calculations, RF-MEAM, and the 2NN-MEAM potential at 0 K and the corresponding percentage errors ((predicted value – *ab initio* value) / *ab initio* value × 100) for the values predicted by the interatomic potentials.

	<i>ab initio</i> calculations [25]	RF-MEAM		2NN-MEAM	
	(GPa)	value	error	value	error
C_{11}	223	233	4%	211	5%
C_{12}	129	154	19%	64	50%
C_{13}	99	121	22%	101	2%
C_{15}	27	11	22%	50	85%
C_{22}	241	247	2%	235	3%
C_{23}	125	147	18%	108	14%
C_{25}	-9	-8	11%	-17	89%
C_{33}	200	214	7%	194	3%
C_{35}	4	8.5	113%	17	325%
C_{44}	76	65	14%	93	22%
C_{46}	-4	-9	125%	-16	300%
C_{55}	21	46	119%	50	138%
C_{66}	77	71	8%	20	74%

peated five times with different initial random seeds and the results shown are an average of the five different runs.

The initial structure for the cooling-heating simulation is B2, thermally equilibrated at 400 K for 20,000 steps. This is followed by cooling from 400 K to 0 K, and heating to 800 K at 0.01 K/ps. The simulation box is maintained at zero stress, allowing changes in shape and size in all directions. The same simulation is performed on differently-sized cubic simulation boxes with the number of atoms ranging from 2,000 to 512,000. Figure 4.2(a) shows the variation of atomic volume during cooling and heating for a cell with 3,072 atoms. The high-temperature B2 phase (point A) transforms to the B19' martensitic phase on cooling at 335 K (this process is characterized by the sudden increase in atomic volume and shearing of the simulation box). The cooling continues until 0 K (point B) when only the B19' phase remains. Upon heating, a sudden drop in atomic volume is identified at 475 K and the alloy goes back to the high temperature B2 phase up until 800 K (point C). Such a simulation helps us identify the martensitic transformation temperature M_s and the austenitic transformation temperature A_f . Figure 4.2(b) shows the variation of these transformation temperatures with the number of atoms: M_s converges to a value of 328 K when the number of atoms reaches 32,000; A_f converges to 453 K for larger systems. As the number of atoms increases, the initial austenitic structure transforms to a multi-domain multi-variant martensite, with the domain boundaries acting as nucle-

Table 4.4: Comparison of the NiTi martensitic and austenitic transformation temperatures and the transformation strains during tensile and compressive stress-induced B2-B19' phase transformation along different directions calculated using the RF-MEAM and the 2NN-MEAM potentials to known values (experiments from literature and lattice deformation model (LDM) on *ab initio* lattice constants). The percentage errors in the predicted values are calculated with respect to the experimental and LDM (0 K) values for the transformation temperatures and transformation strains.

	experiments [26] (K)	LDM (0K) (%)	RF-MEAM		2NN-MEAM [13]		RF-(0K)-LDM		2NN-(0K)-LDM	
			value (K)	error	value (K)	error	value (%)	error	value (%)	error
M_s	337	3.2	328	-2.7%	270	-21%	3.6	13%	4	25%
A_f	400	3.4	453	13.25%	490	22%	3.5	3%	3.7	9%
$\epsilon_{\text{tens}}^{(100)}$		3.4					3.5	3%	3.7	9%
$\epsilon_{\text{comp}}^{(100)}$		9.4				10	6%	10.2	9%	
$\epsilon_{\text{tens}}^{(110)}$		5.1				4.6	-10%	6	17%	
$\epsilon_{\text{comp}}^{(110)}$		11.4				11.5	1%	12	5%	
$\epsilon_{\text{tens}}^{(111)}$		3.4				3.2	-6%	2.8	-18%	
$\epsilon_{\text{comp}}^{(111)}$										

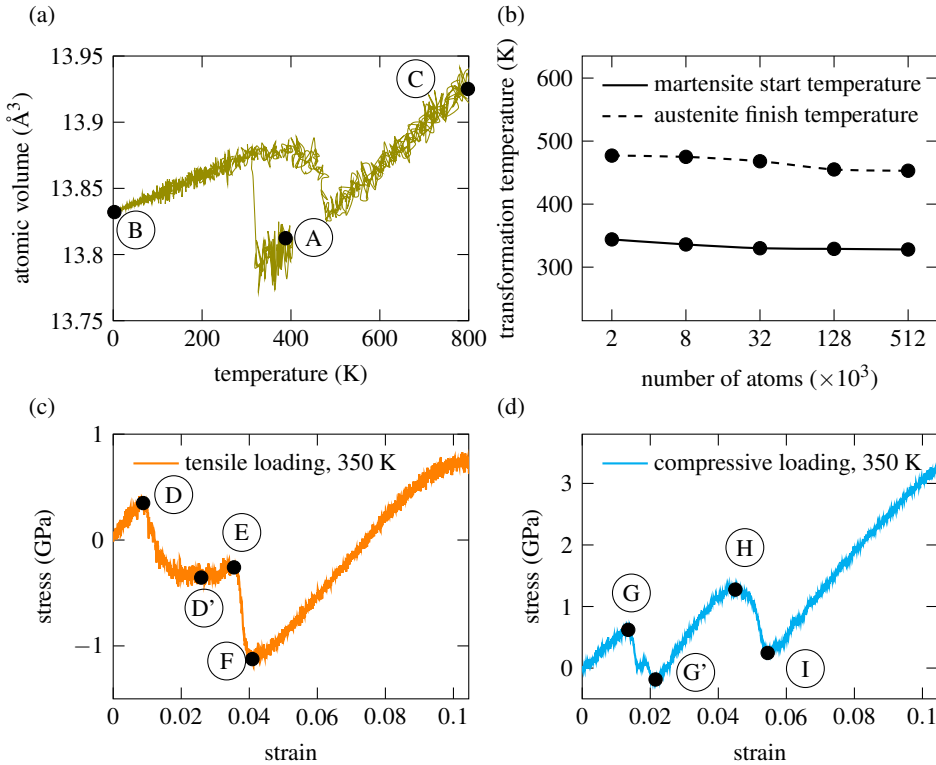


Figure 4.2: (a) Variation of atomic volume with temperature while cooling NiTi B2 from 400 K to 0 K and heating back to 800 K; the sudden change in volume corresponds to the phase transformation. (b) Austenitic and martensitic transformation temperatures plotted as a function of the number of atoms. Isothermal stress-strain behavior of a 73,000-atom B2 structure loaded along $\langle 110 \rangle$ in tension (c) and compression (d). B2 transforms to B19' through the formation of an intermediate B19 phase.

ation sites for the forward transformation from B19' to B2. This size effect has been discussed by Ko et al. [13]. The two transformation temperatures predicted by the RF-MEAM potential are listed in Table 4.4 where they are compared to experimental [26] and 2NN-MEAM [13] values. The RF-MEAM potential predicts the martensitic transformation temperature more accurately than existing potentials. The predicted austenitic transformation temperature, although closer to the experimental value than that predicted by the 2NN-MEAM potential, is still off by around 50 K (13.25%). As discussed in the work of Ko et al. [13], the higher austenitic temperature can be attributed to the fact that MD simulations are performed on a perfectly ideal system whereas experimental values are af-

fectured by defects and grain boundaries in the crystal. This causes A_f to be higher (and the thermal hysteresis larger) than the experimental value in single-crystal MD simulations.

Next, uniaxial loading simulations are performed on an initial B2 structure, thermally equilibrated at 350 K. The results provided here are for a simulation box of size 10.6 nm × 10.6 nm × 10.6 nm. The transformation stresses and strains are unaffected by an additional increase in box size. Strain-controlled tensile and compressive loading simulations are performed at a strain rate of 10^7 /sec. The other sides of the box are maintained at 0 MPa to allow for changes in shape and size. Here, we present the results for the loading of a single-crystal B2 phase along the $\langle 110 \rangle_{B2}$ orientation. Figures 4.2(c) and (d) show the isothermal stress-strain behavior of bulk B2 at 350 K under tension and compression, respectively. In both cases, the initial B2 phase deforms elastically until it reaches the transformation stress (point D in tension and point G in compression). Unlike the temperature-induced martensitic transformation, here the transformation progresses through the formation of an intermediate B19 phase. After point D in tension (and point G in compression), the B2 phase starts transforming into the B19 phase. The intermediate region between D and E (and G and H in compression) corresponds to the progressive B2-B19 transformation until point D' in tension (and G' in compression) followed by the elastic deformation of the B19 phase. Upon further loading, when the strain reaches a value corresponding to point E in tension (and H in compression), the B19 transforms to the B19' phase which is represented by another load drop until point F (and I in compression) after which the structure deforms elastically in the B19' phase. These figures show that the 350 K transformation strain (the strain between a fully relaxed B2 and B19' [28]) under tension and compression is around 7.5% and 5.1%, respectively. As discussed in Chapter 3, the transformation strains are crucial in SMA devices relying on pseudo-elasticity, and they are orientation dependent in single crystal systems. Based on the loading direction, the transformation strains at 0 K can be analytically calculated as a function of the 0 K lattice constants [29]. Hence, based on the lattice constants predicted by the RF-MEAM (Table 4.1), the transformation strains along three directions ($\langle 100 \rangle_{B2}$, $\langle 110 \rangle_{B2}$ and $\langle 111 \rangle_{B2}$, which were reported in Chapter 3 using the 2NN-MEAM [29] potential) under tension and compression are calculated using the RF-MEAM lattice parameters and compared to those calculated using experimental and 2NN-MEAM values in Table 4.4. The new RF-MEAM potential predicts accurate 0 K transformation strain values along various orientations as shown in Table 4.4.

While the methodology used here is generally applicable to any system,

higher order systems (e.g., quaternary, quinary) are considerably more challenging due to the higher-dimensional parameter-space. However, with the efficiency gains due to the analytic derivatives we can now make significant progress in the optimization of such potentials. We present a proof-of-concept for the quaternary case in the next section.

4.4. A RF-MEAM POTENTIAL FOR THE NbMoTaW HIGH-ENTROPY ALLOY

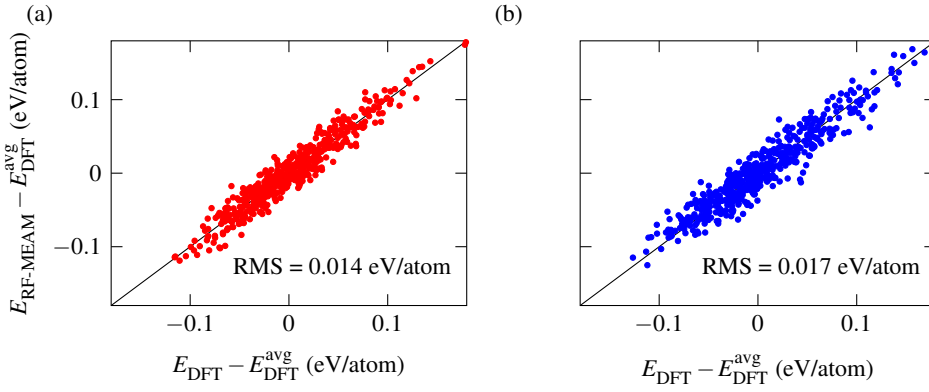


Figure 4.3: Energy difference between the RF-MEAM predicted value and the average DFT energy of the fitted configurations of NbMoTaW plotted against the energy difference between the DFT value and the average DFT energy of the fitted configurations for all MD structures from the fitting set (left) and the testing set (right).

The fitting database for the NbMoTaW alloy is built from 54-atom BCC supercells. The DFT calculations are performed within the PBE-GGA approximation for the exchange-correlation function, with an energy cut-off of 455 eV for the plane wave basis set and the Methfessel-Paxton smearing method with a width of 0.2 eV. A k -point mesh of $2 \times 2 \times 2$ is chosen. 1,000 configurations are generated by randomly repositioning atoms in a sphere with radius 0.025 nm centered at the equilibrium position. The first 500 configurations are used for fitting, and the last 500 are used for testing the fitted potential. A RF-MEAM potential with three pair-wise and three embedding terms is fitted with equal weights assigned to only the energies of the 500 configurations in the fitting set. In total, 180 parameters are fitted to 500 energy data points. We provide a note of caution here: given the number of data-points per parameter, this fitting-set is likely insufficient to avoid over-fitting. Hence, care should be taken before running MD sim-

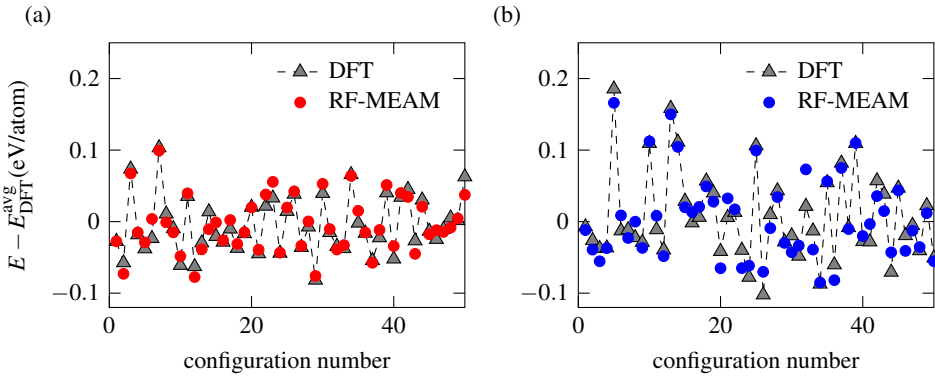


Figure 4.4: Comparison of the NbMoTaW DFT energy difference with the average DFT energy to those obtained using the fitted RF-MEAM potential for 50 configurations taken from the fitting set (left) and the testing set (right).

ulations to first re-optimize using a larger fitting-set. Despite this proviso, we will find that the potential performs surprisingly well when validated against the testing-set.

We obtained an optimization function value $R = 0.16$ for the best-fitted potential. Figure 4.3(a) is a graphical representation of the quality of the fit. The energy difference of the configurations in the fitting database (500 configurations) with the average DFT energy calculated using the RF-MEAM interatomic potential is plotted against the same energy difference obtained from DFT. The RMS error in the energy differences of the fitted dataset is 0.014 eV/atom. The same potential is used on the test dataset (the 500 configurations that were not a part of the fitting database) and yields an optimization function value $R = 0.23$. Figure 4.3(b) compares the energy differences of the 500 configurations in the test set using MD and DFT. The RMS error in the energy differences of the test dataset is 0.017 eV/atom. The close clustering of points near the diagonal line in Fig. 4.3(a) implies the good performance of the fitting procedure and validates the new RF-MEAM implementation in LAMMPS. The scatter is slightly wider near the diagonal line for the test set (Fig. 4.3(b)) in comparison to the fitting database. This is reflected in the optimization function values and the RMS errors in energy differences of the test dataset, which is slightly higher than those for the fitting dataset. Figure 4.4 provides a clearer comparison between predicted and DFT values. Here, the energy difference with the average DFT value of the first 50 configurations from the fitting database and from the test set are

represented. The trends observed by DFT are well reproduced by the RF-MEAM potential, both in the fitted and test sets. While the energy difference of every configuration in the fitted database (Fig. 4.4(a)) is captured accurately, there are a few outliers in the testing set which are also responsible for the wider scatter of points in Fig. 4.3(b). This also suggests that the fitting can be improved further by using more data points (more than 500 energies): more DFT runs and data points corresponding to atomic forces and stresses will improve the accuracy and reliability of the fitted potentials for such high-entropy alloy systems.

The procedure presented in this study and the increasing availability of accurate *ab initio* models for high-entropy and compositionally-complex alloys (see, e.g., reference [30]) allow to fit interatomic potentials that can effectively predict the behavior of these complex materials.

4.5. CONCLUDING REMARKS

RF-MEAM potentials, by virtue of their reference-free formalism, are well suited to be fitted in a feasible time to broad DFT data sets. In this work we have demonstrated that for NiTi the use of a RF-MEAM potential leads to prediction of the pseudoelastic and shape-memory behavior of the alloy that are in better agreement with experimental results when compared with existing potentials. For this specific application, the inclusion of the stress tensor in the fitting database improved the quality of the potential. In general, the fitting database can be altered and broadened based on the target properties that need to be captured. A RF-MEAM potential was also developed for a quaternary alloy to demonstrate that the number of components is not a limitation to the feasibility of the methodology. Obviously, with increasing complexity of the alloy there is an increase in the time required for fitting. Herein, recent advances in machine learning techniques [31, 32] will complement the fitting and modeling of such complex systems.

The implementation of the RF-MEAM potential in LAMMPS and the compatibility with *MEAMfit v2* offer this methodology to a wide community of users. (<https://github.com/PrashanthSri/RF-MEAM-LAMMPS-sub-routines>)

APPENDIX

4.A. USING RF-MEAM IN LAMMPS

4.A.1. IMPROVEMENTS TO *MEAMfit*

MEAMfit v2 has three key improvements in comparison to the previous version of the code *MEAMfit v1.02* [10]. The RF-MEAM potential formalism is implemented as a ‘pair style’ in LAMMPS and is made compatible with *MEAMfit v2* (discussed in Appendix 4.A.2). Stress tensors can now be fitted in addition to energies and atomic forces of configurations. Stress tensor fitting was included in the RF-MEAM developed for NiTi that was discussed in the article. Adding stress tensors has some benefits that are illustrated in Appendix 4.B. Lastly, the derivatives of the optimization function are calculated analytically during fitting (instead of numerically, as in the previous version) improving the efficiency by an order of magnitude in the presently tested systems. In terms of running time, the *MEAMfit v2* code was run on a single Intel Xeon X5650 (2010) core for one week before obtaining the parameters for the NiTi potential, and for one day for the proof-of-concept NbMoTaW HEA potential.

4.A.2. LAMMPS IMPLEMENTATION OF THE RF-MEAM POTENTIAL

New subroutines are written to use the RF-MEAM potential as a part of LAMMPS. Once LAMMPS is re-compiled with the new subroutines, ‘rfmeam’ can be used as a *pair_style* in the input script. The LAMMPS implementation is also compatible with the *MEAMfit v2* code. When a RF-MEAM potential is selected, the code produces interatomic potential files of the form *library.rfmeam.XY_#*, where *X* and *Y* are elements of the system. Files of this form can be used directly in the *pair_coeff* command as the corresponding RF-MEAM interatomic potential file. The new LAMMPS subroutines are not part of the *MEAMfit v2* distribution. They can be downloaded, along with a manual discussing its usage and the interatomic potential files for NiTi and NbMoTaW, from <https://github.com/PrashanthSri/RF-MEAM-LAMMPS-sub-routines>.

4.B. BENEFITS OF STRESS TENSOR FITTING: EXAMPLE USING B2 NiTi

Adding weights to stress tensors during fitting increases the capability of the fitted potential to predict accurate structural behavior. This is demonstrated here through a very simple example. Two structures are chosen for the fitting set: a 0 K 128-atom perfect B2 NiTi structure, and a randomly generated 500 K 54-atom B2 NiTi structure. The computational settings for running the DFT simulations

Table 4.B1: RMS errors in energy, atomic forces in the x , y and z directions, atomic force magnitude and the stress tensor of the 500 K B2 structure (which is a part of the fitted database) as predicted by the three best-fitted potentials fitted only to energies (E fitted), to energies and forces (E, F fitted), and to energies, forces, and stresses (E, F, σ fitted).

RMSE	E (eV/atom)	F_x (eV/Å)	F_y (eV/Å)	F_z (eV/Å)	F (eV/Å)	σ_{ij} (eV/Å ³)
E fitted	0.003	3.76	4.27	3.68	5.99	0.47
E, F fitted	0.017	0.08	0.09	0.09	0.097	0.04
E, F, σ fitted	0.023	0.24	0.23	0.24	0.33	0.001

Table 4.B2: RMS errors in energy, atomic forces in the x , y and z directions, atomic force magnitude and the stress tensor of the 300 K B2 test structure as predicted by the three best-fitted potentials fitted only to energies (E fitted), to energies and forces (E, F fitted), and to energies, forces, and stresses (E, F, σ fitted).

RMSE	E (eV/atom)	F_x (eV/Å)	F_y (eV/Å)	F_z (eV/Å)	F (eV/Å)	σ_{ij} (eV/Å ³)
E fitted	0.001	4.11	3.88	4.21	5.82	0.36
E, F fitted	0.01	0.18	0.17	0.2	0.21	0.06
E, F, σ fitted	0.014	0.31	0.42	0.45	0.5	0.003

are the same as those reported in Section 4.3.1. An *ab initio* MD simulation is performed for the 500 K configuration. In the first step, low convergence parameters are used. MD run with a single k -point is performed for one step. This random snapshot is chosen and recalculated with a high convergence criteria and a denser k -point mesh (Section 4.3.1), providing more accurate values of energies, atomic forces and stress tensors. Atomic forces and stresses for the perfect B2 structure are zero. The energies of the two structures, and the atomic forces and stress tensor of the 500 K configuration calculated from DFT are used in the fitting database. RF-MEAM potentials are fitted with two pair-wise and three embedding terms. Three different fitting runs are performed: in the first case, only energies of the two structures are fitted; in the second case, energies and atomic forces of the 500 K configuration are fitted; and in the third case, energies, atomic forces, and the stress tensor of the 500 K configuration, each with the same weight, are fitted. In the three cases, a total of 56 RF-MEAM parameters are fitted to two, 164 and 170 data points. After each of these fitting runs, interatomic potentials of the form `library.rfmeam.NiTi_#` are produced. The best-fitted RF-MEAM interatomic potential (`library.rfmeam.NiTi_1`) in each of the three fitting runs is used for further simulations.

Figure 4.B1 shows the comparison between the DFT data used for fitting, and

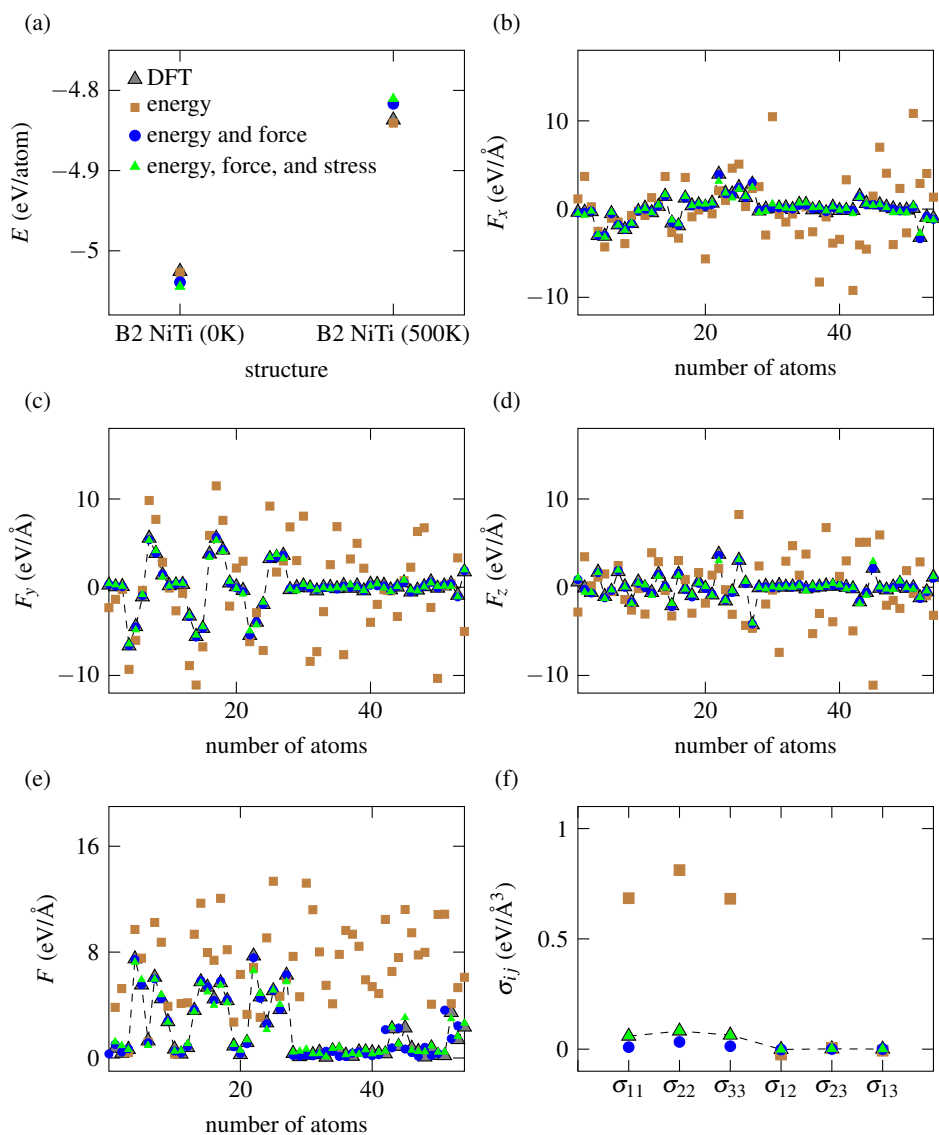


Figure 4.B1: Comparison of fitted data and DFT data: (a) energy of B2 NiTi at 0 K and 500 K; (b), (c), (d) and (e) atomic forces in the x , y and z direction and the force magnitude on each atom of a 54-atom 500 K B2 structure; and (f) stress tensor of the 54-atom 500 K B2 structure, obtained from DFT and from the RF-MEAM potentials fitted to energies, to energies and atomic forces, and to energies, atomic forces, and stress tensor of two B2 structures (at 0 K and 500 K).

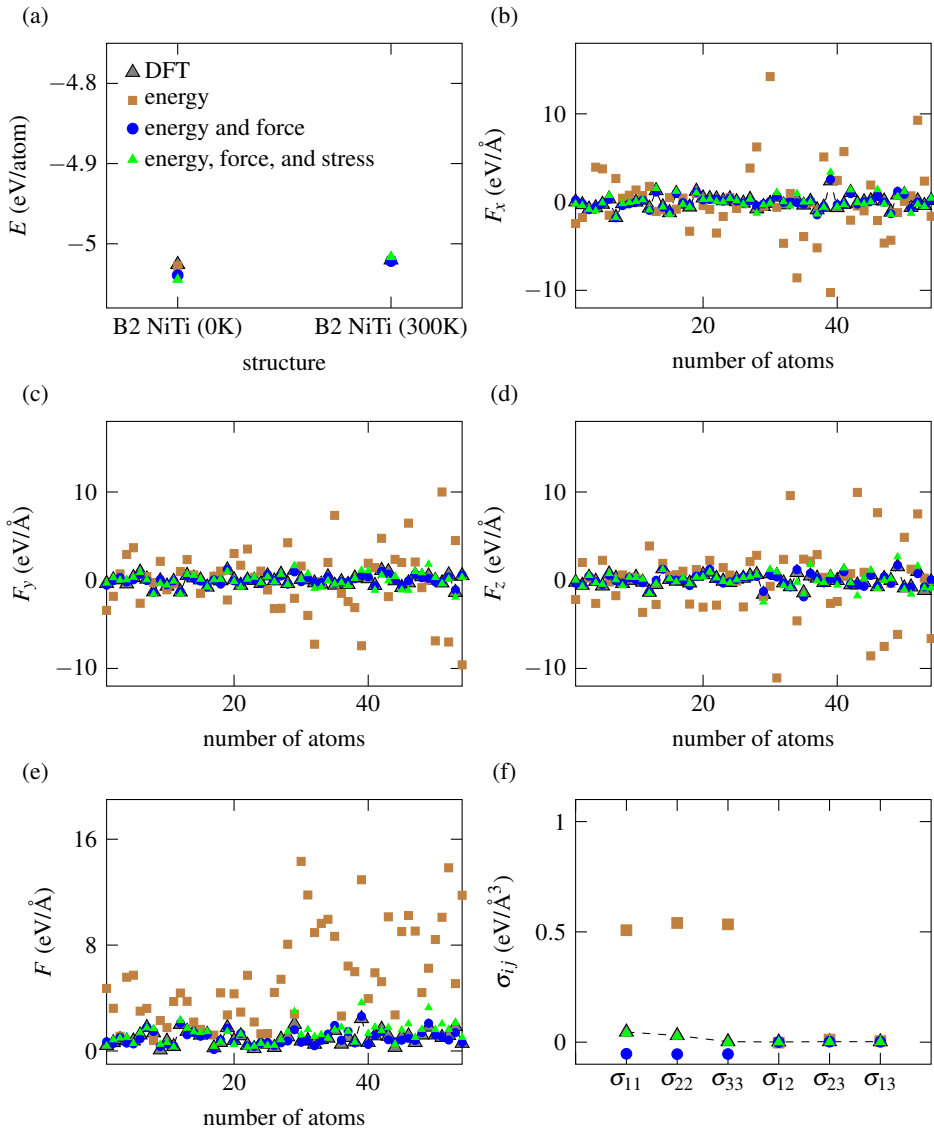


Figure 4.B2: Comparison of test data and DFT data: (a) energy of B2 NiTi at 0 K and 300 K; (b), (c), (d) and (e) atomic forces in the x , y and z direction and the force magnitude on each atom of a 54-atom 300 K B2 structure; and (f) stress tensor of the 54-atom 300 K B2 structure, obtained from DFT and from the RF-MEAM potentials fitted to energies, to energies and atomic forces, and to energies, atomic forces, and stress tensor of two B2 structures (at 0 K and 500 K).

the values predicted by the three best-fitted RF-MEAM potentials fitted only to energies, fitted to energies and forces, and fitted to energies, forces, and stresses. From Fig. 4.B1(a), it is seen that the energy of the two structures used for fitting is captured accurately in all three cases. The largest deviation of around 25 meV/atom from the DFT value happens for the potential fitted to energies, forces, and stress. The deviation from the DFT value increases as the number of data points increase, since other properties apart from the energies are considered in the fitting process. Figures 4.B1(b) to (e) are a comparison of the atomic forces (in the x , y and z direction and the magnitude, respectively) on the 54-atom 500 K B2 structure predicted by the three best-fitted potentials to the DFT data. The x -axis is the number of the atom. The forces predicted by the potential fitted only to the energies of the two structures (brown marks) are completely off from the DFT data, whereas the forces predicted by the other two potentials (blue and green marks) are almost identical to the DFT data. Although most of the forces are captured accurately, the potential fitted to energies, forces, and stress (green marks) shows a few outliers to the DFT data. Finally, Fig. 4.B1(f) compares the stress tensor values of the 500 K structure predicted by the three potentials are compared to the DFT values of the stress on the 500 K structure. The values of the stress components σ_{11} , σ_{22} and σ_{33} predicted by the first potential (brown marks) are way off from DFT data. The second potential, although able to predict atomic forces accurately, fails to capture reasonable values of these stress tensor components (blue marks). Only the potential in the third case predicts these stresses accurately. DFT values of σ_{12} , σ_{23} and σ_{13} on the 500 K structure are very close to zero. Hence the differences between the DFT and fitted data for the first two cases do not appear to be as pronounced as those observed for the other three stress tensor components. The above results are also reflected in Table 4.B1 which compares the RMS error in the predicted values of energy, forces and stress using the three potentials. The first best-fitted potential has a large RMS error in forces and stress. Although the second best-fitted potential predicts energies and forces with a small error, the error on the stress is 40 times that of the potential that is fitted to energies, forces, and stress tensor.

A similar trend in the predictive capabilities of the three potentials is also observed on a test set, which is another randomly configured 54-atom 300 K B2 NiTi structure which is not a part of the fitting database. The same three best-fitted RF-MEAM potentials are now used to calculate the energy, the atomic forces and stress tensor of this 300 K structure. Figures 4.B2(a)-(f) are a comparison of values of the 300 K test structure between DFT and using the three potentials. The first best-fitted potential predicts only the energy of the test structure accurately,

the second one predicts both energy and atomic forces of the test structure, and the best-fitted potential to energies, forces, and stress tensor is able to capture the energy, atomic forces and the stress tensor of the 300 K test structure as well. These are also reflected in Table 4.B2 which shows the RMS error in the predicted values of the test structure using the three potentials. Increasing the weights on the stress tensors might lead to a slightly larger deviation in energy and atomic force values, but would improve the prediction of stresses in the structure and hence can be used to fit potentials that predict the overall structural behavior more accurately.

4.C. NiTi RF-MEAM POTENTIAL PARAMETERS

Table 4.C1: Parameterization of the RF-MEAM potential for NiTi (refer to main text and reference [9] for function definitions and descriptions).

embedding functions						
	E_0	E_1	E_2			
$E_{\text{Ni}}^{\text{emb}}$	-1.50781	8.606×10^{-5}	-4.575×10^{-7}			
$E_{\text{Ti}}^{\text{emb}}$	-0.13549	3.382×10^{-5}	-9.66×10^{-9}			
electron-density prefactors						
	$t^{(1)}$	$t^{(2)}$	$t^{(3)}$			
Ni	0.220111	-2.331485	2.215592			
Ti	-38.754749	-23.844329	-38.529352			
pairwise functions						
	$a^{(1)}$	$r^{(1)}$	$a^{(2)}$	$r^{(2)}$	$a^{(3)}$	$r^{(3)}$
$f_{\text{Ni}}^{(l=0)}$	2.73273	2.37155	11.04081	3.31965	3.23471	3.67209
$f_{\text{Ni}}^{(l=1)}$	-8.91729	2.12621	-2.02712	3.58399	-2.90947	2.16009
$f_{\text{Ni}}^{(l=2)}$	5.41242	3.01173	1.68361	3.70743	-0.97233	1.76718
$f_{\text{Ni}}^{(l=3)}$	12.73072	3.79512	-6.42158	4.19503	1.00650	1.59983
$f_{\text{Ti}}^{(l=0)}$	-5.64898	2.05601	4.73058	3.89254	0.31689	3.00349
$f_{\text{Ti}}^{(l=1)}$	6.22296	2.94493	-1.67552	4.07866	-7.24271	1.60043
$f_{\text{Ti}}^{(l=2)}$	-4.73706	3.52877	-1.60920	2.58967	-1.44040	3.35093
$f_{\text{Ti}}^{(l=3)}$	-1.16063	1.61003	-1.81689	1.67634	-3.19299	1.60121
	$b^{(1)}$	$s^{(1)}$	$b^{(2)}$	$s^{(2)}$	$b^{(3)}$	$s^{(3)}$
$\phi_{\text{Ni-Ni}}$	5.78169	1.81509	-6.76055	1.61758	2.48934	3.31568
$\phi_{\text{Ni-Ti}}$	6.04425	2.32639	-2.03307	1.99486	0.72335	3.54558
$\phi_{\text{Ti-Ti}}$	-1.99631	4.30029	5.63538	2.23451	2.27144	4.23924

REFERENCES

- [1] P. Srinivasan, A. I. Duff, T. Mellan, M. H. F. Sluiter, L. Nicola, and A. Simone, *The effectiveness of reference-free modified embedded atom method potentials demonstrated for NiTi and NbMoTaW*, *Modelling and Simulation in Materials Science and Engineering* **27**, 065013 (2019).
- [2] M. S. Daw and M. I. Baskes, *Embedded-atom method: Derivation and application to impurities, surfaces, and other defects in metals*, *Physical Review B* **29**, 6443 (1984).
- [3] Y.-M. Kim, B.-J. Lee, and M. I. Baskes, *Modified embedded-atom method interatomic potentials for Ti and Zr*, *Physical Review B* **74**, 014101 (2006).
- [4] B.-J. Lee, *A modified embedded-atom method interatomic potential for the Fe-C system*, *Acta Materialia* **54**, 701 (2006).
- [5] J. H. Rose, J. R. Smith, F. Guinea, and J. Ferrante, *Universal features of the equation of state of metals*, *Physical Review B* **29**, 2963 (1984).
- [6] I. Lazić and B. J. Thijsse, *An improved molecular dynamics potential for the Al-O system*, *Computational Materials Science* **53**, 483 (2012).
- [7] M. Timonova and B. J. Thijsse, *Optimizing the MEAM potential for silicon*, *Modeling and Simulation in Materials Science and Engineering* **19**, 015003 (2010).
- [8] *MEAMfit2 is an interatomic potential optimization package which can be obtained from STFC's Daresbury laboratory via the website <https://www.scd.stfc.ac.uk/Pages/MEAMfit-v2.aspx>, .*
- [9] A. I. Duff, M. W. Finnis, P. Maugis, B. J. Thijsse, and M. H. F. Sluiter, *Meamfit: A reference-free modified embedded atom method (RF-MEAM) energy and force-fitting code*, *Computer Physics Communications* **196**, 439 (2015).
- [10] A. I. Duff, *MEAMfit: A reference-free modified embedded atom method (RF-MEAM) energy and force-fitting code*, *Computer Physics Communications* **203**, 354 (2016).
- [11] Y. Zhong, K. Gall, and T. Zhu, *Atomistic study of nanotwins in NiTi shape memory alloys*, *Journal of Applied Physics* **110**, 033532 (2011).

- [12] D. Mutter and P. Nielaba, *Simulation of the shape memory effect in a NiTi nano model system*, Condensed Matter and Materials Science **577**, S83 (2013).
- [13] W.-S. Ko, B. Grabowski, and J. Neugebauer, *Development and application of a Ni-Ti interatomic potential with high predictive accuracy of the martensitic phase transition*, Physical Review B **92**, 134107 (2015).
- [14] W.-S. Ko, S. B. Maisel, B. Grabowski, J. B. Jeon, and J. Neugebauer, *Atomic scale processes of phase transformations in nanocrystalline NiTi shape-memory alloys*, Acta Materialia **123**, 90 (2017).
- [15] S. B. Maisel, W.-S. Ko, J. L. Zhang, B. Grabowski, and J. Neugebauer, *Thermo-mechanical response of NiTi shape-memory nanoprecipitates in TiV alloys*, Physical Review Materials **1**, 033610 (2017).
- [16] W.-S. Ko, B. Grabowski, and J. Neugebauer, *Impact of asymmetric martensite and austenite nucleation and growth behavior on the phase stability and hysteresis of freestanding shape-memory nanoparticles*, Physical Review Materials **2**, 030601 (2018).
- [17] M. Wang, S. Jiang, and Y. Zhang, *Phase transformation, twinning, and detwinning of NiTi shape-memory alloy subject to a shock wave based on molecular-dynamics simulation*, Materials **11**, 2334 (2018).
- [18] H.-Y. Lu, C.-H. Chen, and N.-T. Tsou, *The analysis of superelasticity and microstructural evolution in NiTi single crystals by molecular dynamics*, Materials **12**, 57 (2018).
- [19] Y.-K. Kim, H.-K. Kim, W.-S. Jung, and B.-J. Lee, *Development and application of Ni-Ti and Ni-Al-Ti 2NN-MEAM interatomic potentials for Ni-base superalloys*, Computational Materials Science **139**, 225 (2017).
- [20] D. Scopece and B. J. Thijsse, *Comment on: "An improved molecular dynamics potential for the Al-O system"* Computational Materials Science **53**, 483 (2012), Computational Materials Science **104**, 143 (2015).
- [21] G. Kresse and J. Hafner, *Ab initio molecular-dynamics simulation of the liquid-metal-amorphous-semiconductor transition in germanium*, Physical Review B **49**, 14251 (1994).
- [22] J. P. Perdew, K. Burke, and M. Ernzerhof, *Generalized gradient approximation made simple*, Physical Review Letters **78**, 3865 (1996).

- [23] B. Grabowski, L. Ismer, T. Hickel, and J. Neugebauer, *Ab initio up to the melting point: Anharmonicity and vacancies in aluminum*, Physical Review B **79**, 134106 (2009).
- [24] S. D. Prokoshkin, A. V. Korotitskiy, V. Brailovski, S. Turenne, I. Y. Khmelevskaya, and I. B. Trubitsyna, *On the lattice parameters of phases in binary Ti-Ni shape memory alloys*, Acta Materialia **52**, 4479 (2004).
- [25] M. F.-X. Wagner and W. Windl, *Lattice stability, elastic constants and macroscopic moduli of NiTi martensites from first principles*, Acta Materialia **56**, 6232 (2008).
- [26] J. Frenzel, E. P. George, A. Dlouhy, C. Somsen, M. F.-X. Wagner, and G. Eggeler, *Influence of Ni on martensitic phase transformations in NiTi shape memory alloys*, Acta Materialia **58**, 3444 (2010).
- [27] W. C. Swope, H. C. Anderson, P. H. Berens, and K. R. A. Wilson, *A computer simulation method for the calculation of equilibrium constants for the formation of physical clusters of molecules: Application to small water clusters*, Journal of Chemical Physics **76**, 637 (1982).
- [28] P. Srinivasan, L. Nicola, and A. Simone, *Modeling pseudo-elasticity in NiTi: Why the MEAM potential outperforms the EAM-FS potential*, Computational Materials Science **134**, 145 (2017).
- [29] P. Srinivasan, L. Nicola, and A. Simone, *Atomistic modeling of the orientation dependent pseudo-elasticity in NiTi: Normal loading and bending*, Computational Materials Science **154**, 25 (2018).
- [30] Y. Ikeda, B. Grabowski, and F. Körmann, *Ab initio phase stabilities and mechanical properties of multicomponent alloys: A comprehensive review for high entropy alloys and compositionally complex alloys*, Materials Characterization **147**, 464 (2019).
- [31] A. V. Shapeev, *Moment tensor potentials: A class of systematically improvable interatomic potentials*, Multiscale Modeling and Simulation **14**, 1153 (2016).
- [32] B. Grabowski, Y. Ikeda, F. Körmann, C. Freysoldt, A. I. Duff, A. V. Shapeev, and J. Neugebauer, *Ab initio vibrational free energies including anharmonicity for multicomponent alloys*, arXiv preprint arXiv:1902.11230 .

5

INFLUENCE OF DEFECTS ON PHASE TRANSFORMATION

We study the influence of various defects on the reversible martensitic-austenitic phase transformation in equi-atomic and almost equi-atomic nickel-titanium. Vacancies, anti-site defects, compositional defects and grain boundaries (GBs) in NiTi are modeled and studied using molecular dynamics (MD). MD simulations are performed using the RF-MEAM potential. Martensitic and austenitic transformation temperatures decrease with increasing vacancies and anti-sites, with the austenitic transformation temperature decreasing more drastically. Increasing the concentration of Ni to more than 50% leads to a decrease in both transformation temperatures. GBs act as nucleation sites for the austenitic transformation thereby affecting the transformation temperature and mechanism. In addition, the effect of free surfaces on the transformation behavior is also analyzed by performing MD simulations on differently sized single-crystal nano-wires.

5.1. INTRODUCTION

Crystallographic defects in SMAs affect the reversible martensitic-austenitic transformation properties. It is crucial to study and understand how such defects alter transformation temperatures and mechanism in such materials. Molecular dynamics (MD) offers a convenient way to analyze this behavior. Here, we perform MD simulations on single-crystal nickel-titanium (NiTi) with the presence of point defects such as anti-sites, vacancies, and compositional defects. We also perform MD simulations on a bi-crystal and compare the result to that of the individual grains that the bi-crystal is composed of, to observe the effect of the grain boundary (GB) on the phase transformation.

NiTi is an ideal candidate for various engineering applications owing to its super-elasticity and shape-memory behavior. These properties arise due to its ability to undergo a reversible diffusionless transformation between two phases: the high temperature parent phase (B2 austenite) and the low temperature product phase (B19' martensite). The transformation can be achieved through an external load or heating and cooling. In literature, the material has been investigated through experiments [1–3] and computational techniques [4–8]. One of the common computational techniques that has been used to study NiTi is molecular dynamics (MD). Various studies describe the stress-induced and temperature-induced reversible martensitic transformation in NiTi using different interatomic potentials like the Lennard-Jones potential [9], the embedded-atom method - Finnis Sinclair (EAM-FS) potential [6, 7, 10], the second nearest neighbor - modified embedded-atom method (2NN-MEAM) potential [8], and the reference free - modified embedded-atom method (RF-MEAM) potential [11]). All these works focus on perfect, defect-free single-crystal equi-atomic NiTi.

Experimental and first principle studies have shown that vacancies and anti-site defects are energetically favorable in NiTi. Lu *et al.* [12] used first-principle calculations to suggest the formation of Ti-rich domains in stoichiometric NiTi, and the presence of considerable amount of vacancies in Ti-rich NiTi at high temperatures. Weber *et al.* [13] examined NiTi with vacancies using positron Doppler broadening to calculate the positive vacancy formation enthalpy. Experiments performed by Frenzel *et al.* [14] reported a decrease in the martensitic transformation temperature with an increase in Ni concentration. Besides expecting the presence of such defects in NiTi products, it is also difficult to manufacture perfect single-crystal NiTi structures without the presence of grain boundaries (GBs). A few MD articles in the literature report the effect of such defects on NiTi behavior, but the MD simulations are performed with various older

potentials that do not predict the transformation behavior accurately and hence provide only a qualitative insight into the effect of defects. These studies are also restricted to only some defects in the system. For instance, [Tehrani *et al.* \[15\]](#) reported a decrease in the phase transformation temperatures with an increasing concentration of vacancies and anti-sites in the system using the EAM-FS potential. [Ko *et al.* \[16\]](#) simulated a poly-crystal behavior using the 2NN-MEAM potential to study the effect of GBs on stress-induced and temperature-induced reversible phase transformation. Their MD simulations revealed that the martensitic transformation begins in the bulk of the grain and progresses towards GBs whereas the GBs acted as a nucleation site for the forward transformation to the austenite phase. [Lai and Liu \[17\]](#) modeled anti-site defects using the EAM-FS potential to understand the crystalline to amorphous transition of NiTi.

Earlier works [8, 18] have reported the benefits of using the MEAM potential over the EAM-FS potential to study NiTi behavior arising mainly due to the directional dependency in bonding in the MEAM formalism. As a result, lattice and elastic constants are predicted more accurately. In chapter 4, we have demonstrated the superior performance of a newly developed reference free version of the MEAM potential. Besides capturing accurate values of lattice and elastic constants, the potential also predicts transformation temperatures closer to experimentally known values in comparison to the other potentials. Hence, here we use the RF-MEAM potential described in more detail in the next section.

Although the newly developed RF-MEAM potential predicts transformation temperatures closer to experimentally known values in comparison to other potentials, the austenitic transformation temperature is still higher. The reason was attributed to the fact that the simulations were performed on ideal single-crystal systems [8, 11]. In this work, by introducing defects to the initial structure, we make the simulations more realistic and compare the transformation temperatures and transformation strains to experimental values. Besides validating the values to experimental values, we also demonstrate the effect that the defects have on the phase transformation. The parameters for the RF-MEAM potential were optimized by fitting it to a density functional theory (DFT) database consisting only of equi-atomic configurations. Hence, the predictive power of the RF-MEAM is also demonstrated in this work by performing simulations on non-equiatomic defective structures.

The work presented here focuses on four different defects: vacancies, anti-site defects, compositional defects and grain boundaries; MD runs of stress- and temperature-induced phase transformations on initial structures with such defects are performed using the RF-MEAM potential, and results about transforma-

tion temperatures and strains are presented in Section 3. The results show that the B19'-B2 transformation temperature is the most affected (decreases drastically) with an increasing presence of vacancies and anti-sites in the initial structure. An increase in Ni content (more than 50%) also lowers the transformation temperatures as observed experimentally [14]. The role of grain boundaries in the transformation behavior is demonstrated through a simple bi-crystal simulation. The GB acts as a nucleation site for the B19'-B2 transformation thereby considerably reducing the austenitic start temperature. Additionally, simulations on single-crystal nano-wires are also included to study the role of free surfaces on the phase transformation, which, although not related to defects, affect the transformation behavior similarly to GBs. The simulations, summarised in the last section, highlight the effect of different defects on transformation properties in NiTi and provide an understanding on how defects affect the structural transformation.

5

5.2. MODELING DETAILS

MD simulations are performed using LAMMPS [19]. The newly developed RF-MEAM potential [11, 20] for NiTi is used as the interatomic interaction model. According to the RF-MEAM formalism, the total energy of an N-atom system is given as

$$E = \sum_{i=1}^N E_i^{emb}(\rho_i) + \frac{1}{2} \sum_{i \neq j}^N \phi_{i,j}(r_{ij}),$$

where $E_i^{emb}(\rho_i)$ is the embedding energy function, ρ_i is the fictitious electron density at site i and $\phi_{i,j}(r_{ij})$ is the pair potential between atoms i and j separated by a distance r_{ij} . The embedding function is described as a function of the partial electron densities, and the partial electron densities and the pair-potentials are written as sums over cubic terms as

$$f_i^{(l)}(r) = \sum_{n=1}^{N_1} a_i^{(n,l)} (r_i^{(n,l)} - r)^3 \theta(r_i^{(n,l)} - r), \text{ and}$$

$$\phi_{i,j}^{(l)}(r) = \sum_{n=1}^{N_2} b_{i,j}^{(n)} (s_{i,j}^{(n)} - r)^3 \theta(s_{i,j}^{(n)} - r),$$

respectively. Here, $a_i^{(n,l)}$, $b_{i,j}^{(n)}$, $r_i^{(n,l)}$ and $s_{i,j}^{(n)}$ ($l = 0, 1, 2, 3$) are parameters listed in the previous chapter. The parameters have been optimized by fitting to 0 K and high-temperature equi-atomic NiTi data. The fitting database does not contain configurations with defects. The 0 K lattice parameters and elastic constants

and the cohesive energies of the B2 and the B19' phases of an equi-atomic NiTi predicted by the RF-MEAM are in chapter 4. The results shown in this work for systems with defects demonstrate the power and predictive capabilities of the RF-MEAM potential.

Periodic boxes are employed for all simulations. The effect of the simulation box size on the transformation temperature was shown in chapter 4. Here, we choose a 10 nm × 10 nm × 10 nm box. This is a converged box size beyond which the effect on transformation properties is negligible. The cooling-heating simulations are performed at 0.01 K/ps during which the simulation box is maintained at zero stress, allowing the box to change shape and size in all dimensions. The strain-controlled loading simulations are performed at 10⁷/sec during which other sides of the box are maintained at 0 MPa to allow for changes in shape and size. Temperature and pressure control is done using the Nose-Hoover thermostat algorithm [21] and the Parrinello-Rahman method, respectively. Time integration is performed using the velocity-Verlet algorithm [22] using a time step of 0.5 fs. Visualization is done using OVITO software [23]. All the results shown in this work are an average of the results obtained using five different random initial seeds. The details of the initial structure with various defects are mentioned in the corresponding subsections. Similarly, the details of the nano-wire simulations are described in Section 3.6.

5.3. RESULTS AND DISCUSSION

5.3.1. TRANSFORMATION IN PERFECT NiTi

Before studying the effect of defects, we show the MD results of an ideal single-crystal equi-atomic NiTi using the RF-MEAM potential as an aid for the comparisons in following subsections. More details on the perfect crystal behavior can be found in the previous chapter. Results of temperature- and stress-induced phase transformation are shown here. Both simulations start with a perfect B2 structure. In the first simulation, the B2 structure is thermally equilibrated at 400 K, after which the system is cooled to 100 K and heated back to 600 K. In the second simulation, a tensile load is applied on the B2 structure at 350 K along $\langle 110 \rangle_{B2}$.

In Fig. 5.1(a), sudden jumps indicate phase transformation; the B2 transforms to B19' on cooling which transforms back to B2 on heating. Non-zero lattice parameters of B2 and B19' and the transformation temperatures (M_s and A_f) are tabulated and compared to experimentally known values in Table 5.1. Figure 5.1(b) demonstrates the stress-induced transformation of B2 to B19'. Two

linear elastic loading regions corresponding to the deformation of the initial B2 and the fully transformed B19' phase are separated by a non-linear region where the phase transformation occurs. Similar behavior is observed for other orientations as well as discussed in chapter 3. In the following subsections, we present the results of such MD simulations on systems with various defects.

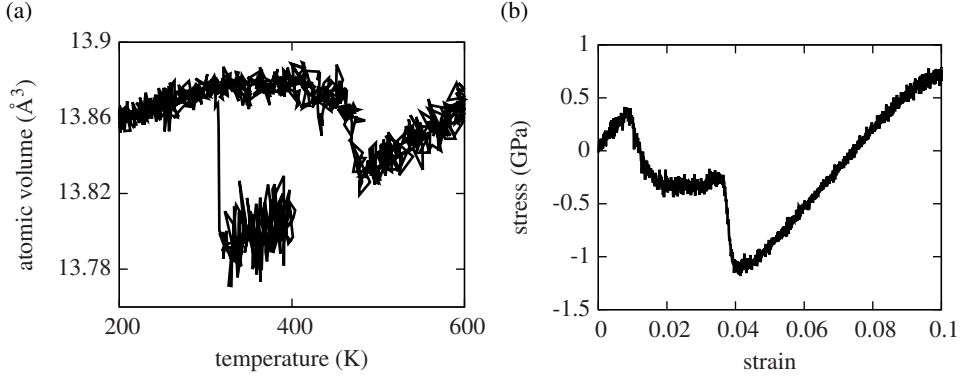


Figure 5.1: (a) Variation of atomic volume with temperature during a cooling-heating cycle from 400 K to 200 K back to 600 K for an initial defect-free single-crystal B2 structure. (b) Isothermal stress-strain behavior of defect-free B2 NiTi loaded in tension along $\langle 110 \rangle_{B2}$ at 350 K.

Table 5.1: Calculated lattice parameters of B2 at 400 K and B19' at 300 K (in Å), the monoclinic angle of B19' at 300 K (in degrees) and the transformation temperatures (in K) compared against previously reported experimental values.

	a_0	a_m	b_m	c_m	γ	M_s	A_f
B2 - MD (400 K)	3.015						
B2 - Expt. (400 K) [24]	3.013						
B19' - MD (300 K)		2.924	4.55	4.177	96		
B19' - Expt. (300 K) [25]		2.909	4.657	4.114	97.9		
B2-B19' - MD						328	463
B2-B19' - Expt. [14]						337	400

5.3.2. INFLUENCE OF ANTI-SITE DEFECTS

Anti-site defects are the most commonly-occurring point defects in NiTi where Ni atoms swap positions with Ti atoms. When NiTi is produced from the melt,

owing to the similar sizes of Ni and Ti atoms, some Ni atoms get trapped in the position of the Ti atom and vice-versa. These can be modeled easily and their effects studied using MD simulations. The initial structure is a equi-atomic B2 crystal where some Ni atoms are swapped with Ti atoms and vice-versa. To study the effect on phase transformation, the concentration of the anti-sites is varied up to 1% of Ni (or Ti) atoms in the structure. Both temperature- and stress-induced transformations are studied in systems with different anti-site defect concentration, by performing the aforementioned cooling-heating and tensile loading simulations.

Swapping of Ni and Ti atoms is done randomly and the results shown below are an average of five different random initial structures. Figure 5.2(a) shows the variation of atomic volume during the cooling-heating cycle for B2 with different anti-site concentration. As the number of anti-sites increase, both M_s and A_f decrease, with A_f decreasing much more rapidly. The trend continues until 0.75% defects. Above 0.75% (for the case of 1%), the entire structure does not transform into B19', hence the atomic volume falls in between B2 and B19' at the end of cooling. When the anti-site defect concentration is high enough ($> 0.25\%$), there are regions in the structure where clusters of Ni or Ti atoms are present that locally inhibit the martensitic transformation. This creates B2-B19' phase boundaries inside the crystal. These phase boundaries within the crystal act as nucleation for the forward transformation during heating. Hence, the transformation to B2 happens earlier as seen in Fig. 5.2(a). The martensitic start temperature M_s and the austenitic finish temperature A_f from Fig. 5.2(a) are plotted against anti-site concentration in Fig. 5.2(b). More data points (defect concentrations) are included in the plot. Figure 5.2(c) shows the stress-strain behavior at 350 K. Results for only 2 defective structures are shown here. It can be observed that the transformation stress increases as the defect concentration increases. The difference in the transformation strain (the non-zero strain at 0 GPa stress) is very small. The transformation strain is a function of the lattice constants of the B2 and B19' phase [18] and anti-site defects of the order of 1% have negligible effect on the lattice constants of both phases.

5.3.3. INFLUENCE OF NI CONTENT

The effect of Ni content on the martensitic transformation temperature in near equi-atomic NiTi has been analyzed in many experimental studies [14, 26, 27]. The martensitic start temperature is known to reduce sharply even when the Ni content increases by just 1%. Here, we run cooling-heating and tensile loading simulations on near equi-atomic NiTi using the RF-MEAM potential. To create

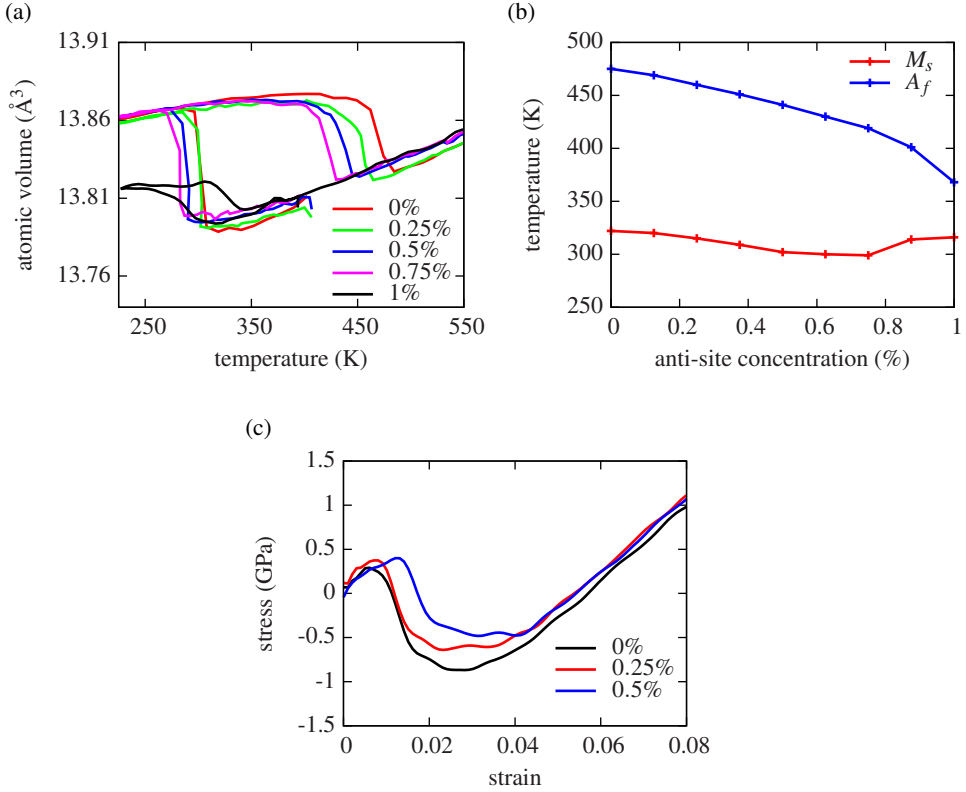


Figure 5.2: (a) Variation of atomic volume with temperature during a cooling-heating cycle from 400 K to 225 K back to 550 K for an initial B2 structure with different anti-site defect concentration. The martensitic start and austenitic finish temperatures from (a) are plotted against defect concentration in (b). (c) Isothermal stress-strain behavior of B2 NiTi with different defect concentration at 350 K.

such structures, either some Ni atoms are replaced with Ti or Ti atoms replaced with Ni depending on the Ni content that is needed. For each Ni content, five such structures are created with randomly replaced atoms and the results below are an average of the five structures.

Figure 5.3(a) shows the variation of atomic volume with temperature for nearly equi-atomic NiTi (various Ni content). The atomic volume (and the lattice constant) of the B2 phase decreases slightly with increase in Ni content. The predicted values of M_s and A_f are plotted as a function of Ni content in

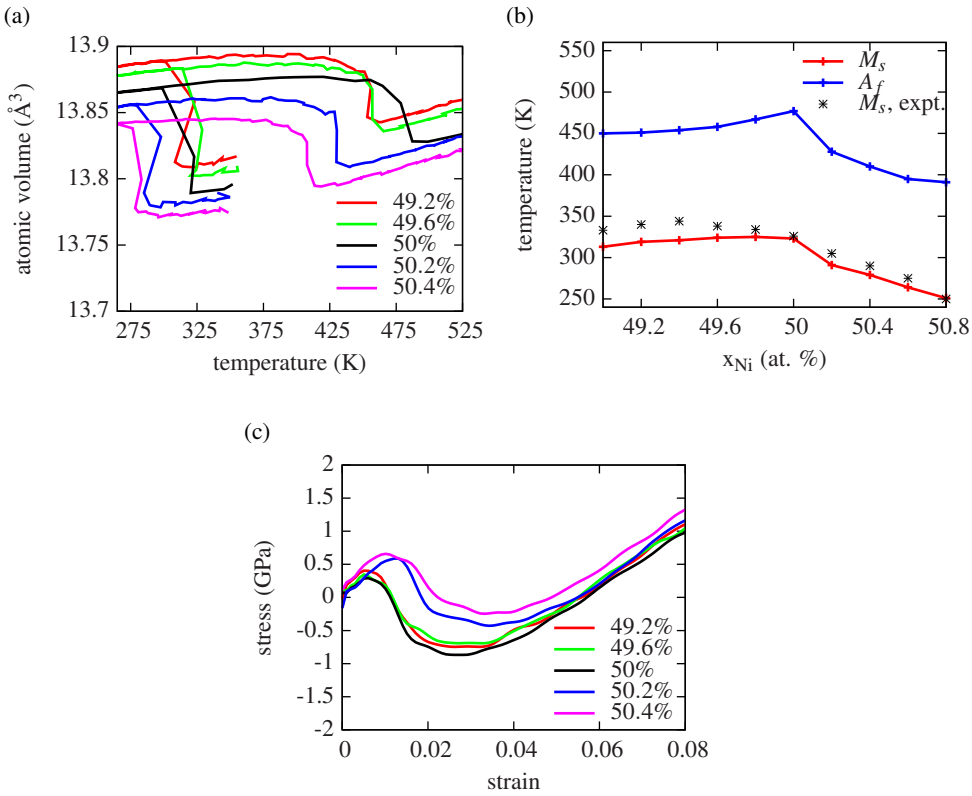


Figure 5.3: (a) Variation of atomic volume with temperature during a cooling-heating cycle from 350 K to 250 K back to 525 K for an initial B2 structure with different Ni content. The martensitic start and austenitic finish temperatures from (a) are plotted against Ni content in (b); the experimental values [14] of M_s are also plotted for comparison. (c) Isothermal stress-strain behavior of B2 NiTi with different Ni content at 350 K.

Fig. 5.3(b). The martensitic start temperature is also compared against experimentally known values [14]. The trend is captured reasonably well by the MD simulations and M_s does not vary by more than 10 K when the Ni content is less than 50% as also observed experimentally. Although M_s does not vary to a great extent, MD predicts that A_f decreases as the Ni content becomes lower than 50%, showing the highest value for a perfectly equi-atomic NiTi structure. When the Ni content is above 50%, both M_s and A_f drop considerably. The drop in M_s has also been observed experimentally. The drop in M_s with increasing Ni

content above 50% has been suggested as a result of the decreasing latent heat of the B2-B19' transformation [14]. The decrease in latent heat is a result of the stabilization of B2 where the formation of Ni on Ti lattice positions causes local lattice relaxations in the crystal. Figure 5.3(c) shows the isothermal stress-strain behavior of near equi-atomic B2 NiTi at 350 K. The transformation stress and strain are not affected when the Ni content is less than 50%. Increasing Ni content above 50% mildly increases the transformation stress.

5.3.4. INFLUENCE OF VACANCIES

Vacancy defect is a point defect in any crystal where atoms are missing from their lattice site. Schottky-type vacancies are modeled in equi-atomic NiTi by removing an equal number of Ni and Ti atoms from the perfect crystal. To study the effect that it has on the transformation behavior, the concentration of vacancies is varied up to 0.5% of the total number of atoms in the system. Again, the vacancies are created randomly and the results below are an average value of five different initial structures. Both temperature- and stress-induced transformations are studied in same-sized systems with different vacancy concentration by performing the aforementioned cooling-heating and tensile loading simulations.

In Fig. 5.4(a), the atomic volume of structures with different vacancy concentration is plotted against temperature. A few notable features arise due to the additional vacancies in the structure. The atomic volume of the initial B2 phase increases as the vacancy percentage increases. The total volume of the system does not change much with the presence of vacancies. The atomic volume is calculated as the system volume divided by the number of atoms in the system. As the vacancy concentration increases, the number of atoms decrease leading to an increase in the atomic volume. The next notable feature is the decrease in the martensitic and austenitic transformation temperatures with increasing vacancy which is also observed in Fig. 5.4(b). The values of M_s and A_f in Fig. 5.4(b) are obtained from Fig. 5.4(a). Many similarities can be noticed between the trends observed here in comparison to the effect of anti-site defects in Figs. 5.2(a) and (b). For instance, the drop in A_f is much more drastic in comparison to the drop in M_s , which was also observed in systems with anti-site defects. Above 0.5% vacancy concentration, M_s no longer drops since the martensitic transformation is locally restricted inside the crystal due to the presence of vacancies. In such cases, the forward transformation to B2 starts earlier. As the vacancy concentration increases, the B19'-B2 transformation becomes more and more gradual as seen in Fig. 5.4(a). The vacancies act as nucleation sites where the phase transformation begins and gradually grows through the rest of the crystal. The decrease

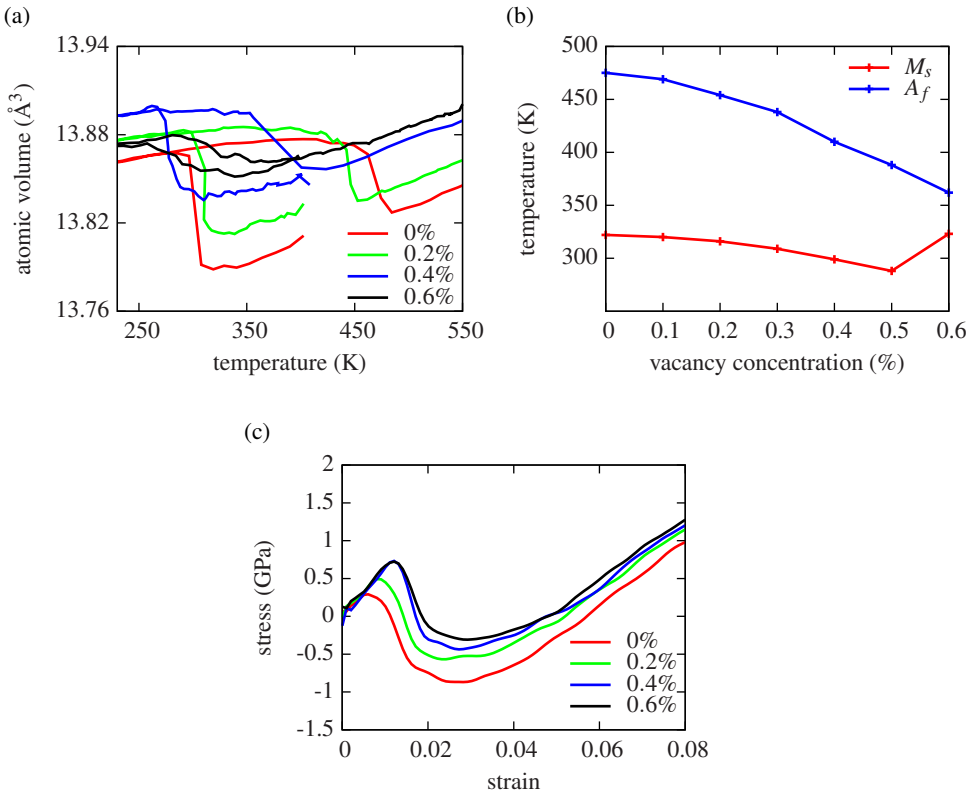


Figure 5.4: (a) Variation of atomic volume with temperature during a cooling-heating cycle from 425 K to 225 K back to 550 K for an initial B2 structure with different vacancy concentration. The martensitic start and austenitic finish temperatures obtained from (a) are plotted against vacancy concentration in (b). (c) Isothermal stress-strain behavior of B2 NiTi with different vacancy concentration at 350 K.

in A_f (and the eventual decrease in M_s) can also be explained as suggested in Ref. [15]. Introducing vacancies increases the configurational entropy [9]. This favours the austenitic phase over the martensitic phase [28] and a greater driving force is required for the martensitic transformation. The system favors the austenitic phase thereby reducing both M_s and A_f . Figure 5.4(c) is the isothermal stress-strain behavior of B2 with different vacancy concentration at 350 K. As the number of vacancies increase, the transformation stress also increases. The presence of vacancies mildly affects the lattice constants of both phase. Hence, a

15% decrease in the transformation strain (which is a function of the lattice constants of B2 and B19') is also noticed as vacancy concentration increases from 0% to 0.6%.

5.3.5. SIMULATING BI-CRYSTAL BEHAVIOR

Besides point defects, 2D defects in the form of grain boundaries (GBs) also affect phase transformation behavior. *Ko et al.* [8] studied the effect of GBs on phase transformation using the 2NN-MEAM potential by simulating poly-crystals with differently-sized grains. In small-sized grains, the B2-B19' transformation began in the interior of the grains and eventually grew outwards towards the GBs. The GBs acted as nucleation sites for the forward transformation of B19'-B2, starting at the GB and growing through the interior of the crystal. Here, we perform MD simulations using the RF-MEAM potential to analyze the effect of GBs on phase transformation. We do so by simulating cooling-heating and tensile loading simulations on a simple bi-crystal with a GB and comparing the results to that of a single-crystal.

A random mixed grain GB is created by choosing a bi-crystal with two stacked grains, the first grain oriented along $[100]_{B2}$, $[010]_{B2}$ and $[001]_{B2}$ and the second grain oriented along $[110]_{B2}$, $[1\bar{1}0]_{B2}$ and $[001]_{B2}$. Atoms at the GB that lie within half the lattice constant of B2 (1.5 nm) are removed and a 0 K energy minimization is performed on the bi-crystal. The simulation box is periodic in all directions, which makes all the GBs identical. The size of each grain is $10\text{ nm} \times 10\text{ nm} \times 10\text{ nm}$. This is chosen such that the GBs do not interact with each other and the effect of the GB on the phase transformation can be studied independently. Following a thermal equilibration at 350 K, cooling-heating and tensile loading simulations are performed. Figure 5.5(a) shows the variation of atomic volume with temperature during the cooling-heating cycle for the bi-crystal in comparison to that of a single-crystal. The GB does not affect M_s but A_f reduces by around 70 K. The presence of the GB also makes the transformations more gradual than in a single-crystal. This is attributed to the aforementioned reason wherein the martensitic transformation begins in the grain interior and progresses to the GB, and the austenitic transformation nucleates at the GB and progresses through the entire grain. The effect of the GB on making the phase transformation more gradual can also be validated by visualizing the bi-crystal during the cooling-heating cycle as shown in Fig. 5.5(c). Here, atoms are colored according to the common neighbor analysis (CNA) pattern that differentiates atoms in the B2 phase (blue colored) from the other atoms (red colored). Labels A to C correspond to the cooling stage at 375 K, 280 K and 225 K respec-

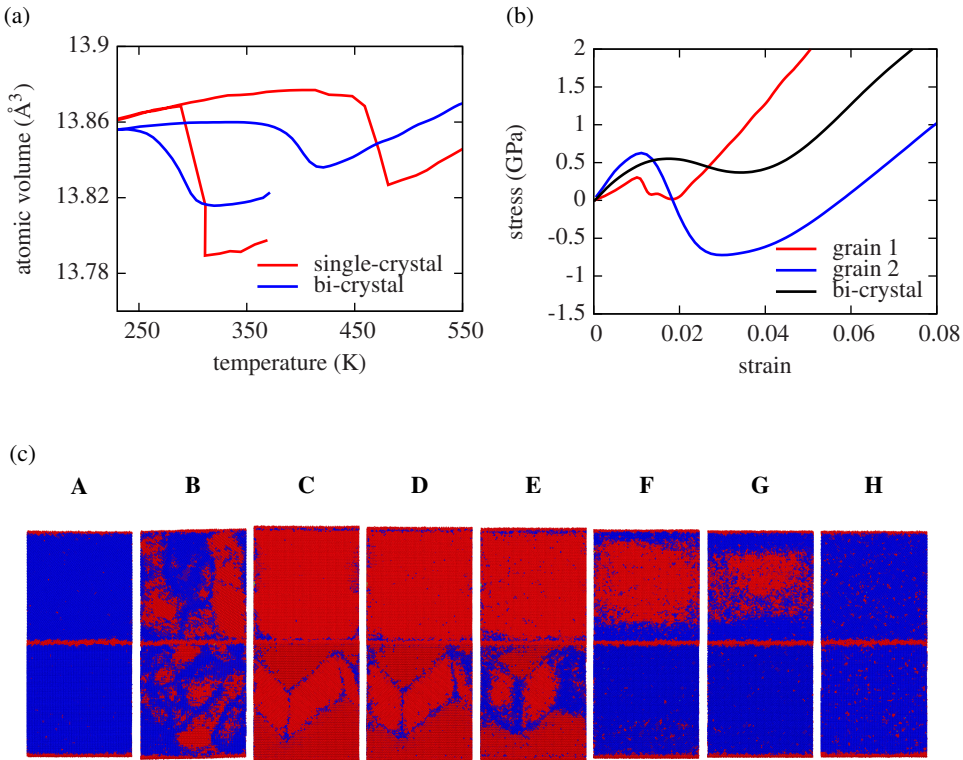


Figure 5.5: (a) Variation of atomic volume with temperature during a cooling-heating cycle from 375 K to 225 K back to 550 K for the bi-crystal and a single-crystal. (b) Isothermal stress-strain behavior of the bi-crystal loaded perpendicular to the GB plane and the corresponding single-crystals at 350 K. (c) Evolution of the phase transformation in the bi-crystal during cooling (A to C) and heating (D to H). Atoms are colored according to the common neighbor analysis (CNA) pattern; blue colored balls represent atoms in the B2 (BCC) structure and the red colored balls represent atoms not in the B2 phase (atoms at the GB and the transformed B19' inside the grains). Figures E to F illustrate that the martensitic domain boundaries and the GB acts as nucleation for the austenitic transformation.

tively. In A, the GBs are distinctly seen as lines of red colored balls. Since the simulation box is periodic, the GBs are identical. As the system is cooled, red patches are observed in the interior of the grains indicating the transformation to the B19' phase. In C, the martensitic transformation is complete. In the grain on top, it can be seen that a single domain of B19' is formed at the end of cooling, whereas in the grain below, multiple domains of B19' are formed with untrans-

formed B2 as the domain boundaries between them. Figs. D to H correspond to the heating stage at 400 K, 440 K, 450 K, 465 K and 500 K respectively. It is observed that the forward transformation to the parent B2 phase is nucleated either from the domain boundaries (bottom grain) or the GBs (top grain) and then progresses through the rest of the grain, thereby initiating the transformation earlier and making the transformation more gradual in comparison to a single-crystal. Figure 5.5(b) shows the isothermal stress strain behavior of the bi-crystal loaded perpendicular to the GB in comparison to the two individual grains loaded along $\langle 100 \rangle_{B2}$ and $\langle 110 \rangle_{B2}$ at 350 K. The modulus of both the B2 and B19' phases and the transformation strain of the bi-crystal falls in between that of the individual single crystals.

5.3.6. TRANSFORMATION IN CYLINDRICAL NiTi NANO-WIRES

5

Apart from crystalline defects in the system, transformation properties and the transformation mechanism are also affected by the presence of free surfaces which is especially true in nano-scaled structures with a high surface area-volume ratio. To investigate this, we perform MD simulations using the RF-MEAM potential on differently sized cylindrical nano-wires. In earlier works [8, 11], the effect of the simulation box size of a fully periodic system on the transformation temperature was studied. As the box size increased, a multi-variant martensitic structure was formed upon cooling austenite. The variant boundaries act as nucleation sites for the forward transformation thereby reducing the transformation temperature. Here, we study the effect of size on non-periodic nano-wire systems to also include the effect of free surfaces on the phase transformation.

The initial B2 nano-wires are periodic along the axis, aligned in the $\langle 110 \rangle_{B2}$ direction. Nano-wires ranging from $d = 5$ nm to $d = 24$ nm are chosen. The length of the simulation box along the axis is 32 nm, above which the results are not affected by the periodic length of the box. After thermal equilibration at 400 K, the nano-wires are cooled to 200 K and heated back to 500 K. The pressure along the face of the nano-wires is maintained at 0 Pa to allow for change in length during the cooling-heating process. The axial strain in the nano-wire is plotted against temperature. Figure 5.6(a) shows the variation of the axial strain with temperature for three differently-sized nano-wires. The first wire with $d = 5$ nm does not show a phase transformation, i.e., there is no sudden change in the axial strain. There is no transformation observed until $d = 8$ nm. Above this diameter, the wires start showing phase transformation as observed for the $d = 12$ nm, $d = 20$ nm and $d = 24$ nm wires. As the diameter of the wires in-

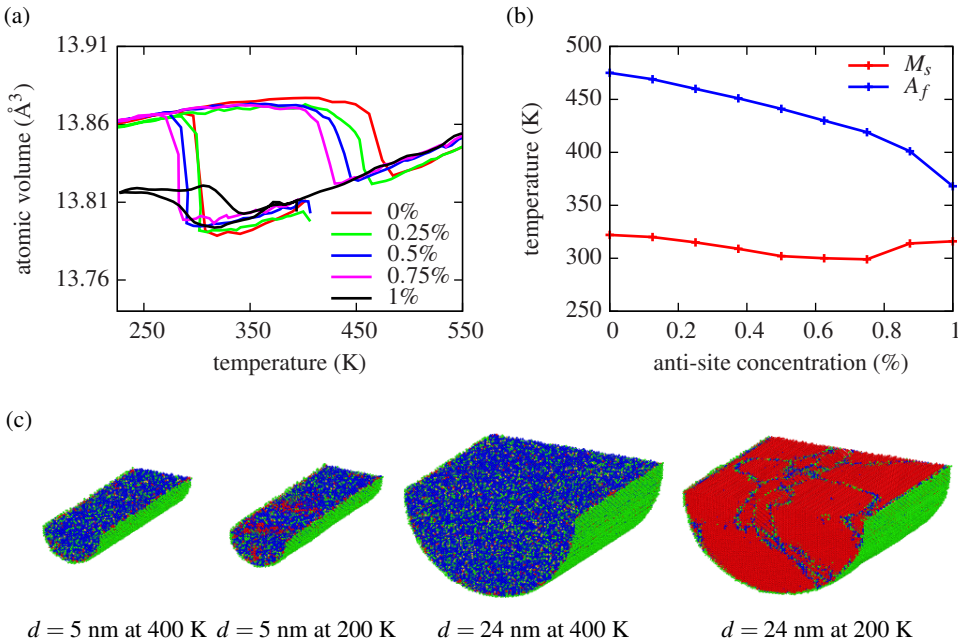


Figure 5.6: (a) Initial structure and orientation of a $d = 8$ nm B2 cylindrical nano-wire. (a) Variation of the axial strain with temperature during a cooling-heating cycle from 400 K to 200 K back to 500 K for four differently-sized nano-wires. (b) Martensitic and austenitic start and finish temperatures plotted against the diameter of the nano-wires. (c) Two cylindrical nano-wires (5 nm and 24 nm) at 400 K and 200 K cut along their length and colored according to the common neighbor analysis (CNA) pattern. Blue colored balls represent atoms in B2, red colored balls represent atoms in B19' and green colored balls represent atoms at the free surface of the nano-wires.

crease, M_s starts decreasing until it converges to a value of 330 K; the transformation becomes less gradual with a decrease in the temperature difference between the start and end of the transformation. During the forward transformation to austenite, as the diameter of the wires decrease, the transformation starts earlier and becomes more gradual. These results are summarized in Fig. 5.6(b) which also includes data points of nano-wires not included in Fig. 5.6(a). Both M_s and A_f converge close to the values of a bulk single-crystal after a size of $d = 24$ nm and the slope of the transformations (difference between M_s and M_f and A_s and A_f) also converge, suggesting that the effect of free surfaces on the transformation in thick nano-wires is negligible. The wires are also visualized according to a CNA pattern as shown in Fig. 5.6(c) where blue colored balls represent atoms

in B2 and red colored balls represent atoms in B19'. Atoms at the free surfaces are in green. Here, two wires with diameters of 5 nm and 24 nm are shown at 400 K and 200 K. It can be observed that the thinner 5 nm diameter wire shows only very limited phase transformation to martensite upon cooling whereas the thicker 24 nm diameter wire transforms into a multi-domain martensite structure with some untransformed B2 acting as domain boundaries. In nano-wires lesser than $d = 8$ nm, it becomes difficult to accommodate a phase transformation inside the wire. The energy required for the transformation to happen inside the wire is higher than the energy needed to axially strain them. Hence, they prefer to stay in the parent phase and not show any phase transformation. Above $d = 8$ nm, the size of the wire is sufficient to accommodate a martensitic transformation that is energetically favorable. In wires as thick as the $d = 24$ nm wire, accommodating multiple domains of B19' inside the wire becomes more favorable than forming a single domain of B19' that strains the wire to a greater extent. In the forward transformation to B2, the role of the free surfaces and the domain boundaries is similar to that of a GB in a bi-crystal. The free surfaces act as nucleation sites for the forward transformation and the effect is more pronounced in smaller diameter wires where the surface area-volume ratio is higher. Hence, as the size of the wires decrease, the austenitic transformation begins earlier and the transformation is more gradual. The effect becomes weaker as the size increases and eventually the transformation temperatures converge to those of a bulk single-crystal.

5

5.4. CONCLUSION

The RF-MEAM potential was not able to capture accurate austenitic transformation temperature: the predicted value was 60-80 K higher than experimentally known values and the reason was attributed to the presence of defects in the specimens used in experiments. Here, we have tested possible defects that could arise in NiTi SMAs and we have studied the effect that they have on the phase transformation temperature using the RF-MEAM potential. Although the martensitic transformation temperature and transformation strains (properties that were compared to experiments in chapter 4) decrease slightly with increasing defect concentration, the austenitic finish temperature is drastically reduced by the presence of any of the afore-mentioned defects, bringing it much closer to the experimentally-known value. Hence, this validates the predictive capability of the RF-MEAM potential to model the NiTi system by making the comparison to experiments much more realistic.

Point defects such as anti-sites and vacancies reduce the transformation

temperatures. The drop in A_f is much sharper. Both anti-sites and vacancies create local inhibitions to the martensitic transformation. The effect of Ni content on the phase transformation is compared and validated with experimental data. Both M_s and A_f drop when Ni content is more than 50%. 2D defects (GB) are also studied by simulating a mixed GB bi-crystal. The GB acts as a nucleation site for the forward austenitic transformation, causing it to start earlier and making it more gradual as the temperature increases. A similar effect is also produced by free surfaces on the phase transformation; this is analyzed by performing cooling-heating simulations on differently sized nano-wires.

REFERENCES

- [1] O. Matsumoto, S. Miyazaki, K. Otsuka, and H. Tamura, *Crystallography of martensitic transformation in TiNi single crystals*, *Acta Materialia* **35**, 2137 (1987).
- [2] S. Mao, J. Luo, Z. Zhang, M. Wu, Y. Liu, and X. Han, *EBSD studies of the stress-induced B2-B19' martensitic transformation in NiTi tubes under uniaxial tension and compression*, *Acta Materialia* **58**, 3357 (2010).
- [3] J. M. Jani, M. Leary, A. Subic, and M. A. Gibson, *A review of shape memory alloy research, applications and opportunities*, *Materials and Design* **56**, 1078 (2014).
- [4] X. Huang, G. J. Ackland, and K. M. Rabe, *Crystal structures and shape-memory behaviour of NiTi*, *Nature Materials* **2**, 307 (2003).
- [5] O. Kastner, G. Eggeler, W. Weiss, and G. Ackland, *Molecular dynamics simulation study of microstructure evolution during cyclic martensitic transformations*, *Journal of the Mechanics and Physics of Solids* **59**, 1888 (2011).
- [6] D. Mutter and P. Nielaba, *Simulation of the shape memory effect in a NiTi nano model system*, *Condensed Matter and Materials Science* **577**, S83 (2013).
- [7] Y. Zhong, K. Gall, and T. Zhu, *Atomistic study of nanotwins in NiTi shape memory alloys*, *Journal of Applied Physics* **110**, 033532 (2011).
- [8] W.-S. Ko, B. Grabowski, and J. Neugebauer, *Development and application of a Ni-Ti interatomic potential with high predictive accuracy of the martensitic phase transition*, *Physical Review B* **92**, 134107 (2015).
- [9] O. Kastner, *Molecular-dynamics of a 2D model of the shape memory effect*, *Continuum Mechanics and Thermodynamics* **15**, 487 (2003).
- [10] G. Ren and H. Sehitoglu, *Interatomic potential for the NiTi alloy and its application*, *Computational Materials Science* **123**, 19 (2016).
- [11] P. Srinivasan, A. I. Duff, T. Mellan, M. H. F. Sluiter, L. Nicola, and A. Simone, *The effectiveness of reference-free modified embedded atom method potentials demonstrated for NiTi and NbMoTaW*, *Modelling and Simulation in Materials Science and Engineering* **27**, 065013 (2019).

- [12] J. Lu, Q. Hu, L. Wang, Y. Li, D. Xu, and R. Yang, *Point defects and their interaction in TiNi from first-principles calculations*, Physical Review B **75** (2007).
- [13] M. Weber, T. Ablekim, and K. Lynn, *Vacancies in NiTi shape memory alloys*, Journal of Physics: Conference Series **505** (2014).
- [14] J. Frenzel, E. P. George, A. Dlouhy, C. Somsen, M. F.-X. Wagner, and G. Eggeler, *Influence of Ni on martensitic phase transformations in NiTi shape memory alloys*, Acta Materialia **58**, 3444 (2010).
- [15] A. M. Tehrani, H. Shahrokhshahi, N. Parvin, and J. Brgoch, *Influencing the martensitic phase transformation in NiTi through point defects*, Journal of Applied Physics **118** (2015).
- [16] W.-S. Ko, S. B. Maisel, B. Grabowski, J. B. Jeon, and J. Neugebauer, *Atomic scale processes of phase transformations in nanocrystalline NiTi shape-memory alloys*, Acta Materialia **123**, 90 (2017).
- [17] W. Lai and B. Liu, *Lattice stability of some NiTi alloy phases versus their chemical composition and disordering*, Journal of Physics: Condensed Matter **12**, L53 (2000).
- [18] P. Srinivasan, L. Nicola, and A. Simone, *Modeling pseudo-elasticity in NiTi: Why the MEAM potential outperforms the EAM-FS potential*, Computational Materials Science **134**, 145 (2017).
- [19] S. J. Plimpton, *Fast parallel algorithms for short-range molecular dynamics*, Journal of Computer Physics **117**, 1 (1995).
- [20] M. Timonova and B. J. Thijsse, *Optimizing the MEAM potential for silicon*, Modeling and Simulation in Materials Science and Engineering **19**, 015003 (2010).
- [21] S. Nose, *A unified formulation of the constant temperature molecular-dynamics methods*, Journal of Chemical Physics **81**, 511 (1984).
- [22] W. C. Swope, H. C. Anderson, P. H. Berens, and K. R. A. Wilson, *A computer simulation method for the calculation of equilibrium constants for the formation of physical clusters of molecules: Application to small water clusters*, Journal of Chemical Physics **76**, 637 (1982).

- [23] A. Stukowski, *Visualization and analysis of atomistic simulation data with OVITO—the open visualization tool*, Modeling and Simulation in Materials Science and Engineering **18**, 015012 (2010).
- [24] P. Sittner, P. Lukas, D. Neov, V. Novak, and D. Toebbens, *In situ neutron diffraction studies of martensitic transformations in NiTi*, J. Phys. IV France **112** (2003).
- [25] S. D. Prokoshkin, A. V. Korotitskiy, V. Brailovski, S. Turenne, I. Y. Khmelevskaya, and I. B. Trubitsyna, *On the lattice parameters of phases in binary Ti-Ni shape memory alloys*, Acta Materialia **52**, 4479 (2004).
- [26] W. Tang, B. Sundman, R. Sandstrom, and C. Qiu, *New modelling of the B2 phase and its associated martensitic transformation in the Ti–Ni system*, Acta Materialia **47**, 3457 (1999).
- [27] T. Waitz, D. Spisak, J. Hafner, and H. Karthaler, *Size-dependent martensitic transformation path causing atomic-scale twinning of nanocrystalline NiTi shape memory alloys*, Europhysics Letters **71**, 98 (2005).
- [28] R. Elliott and D. Karls, *Entropic stabilization of austenite in shape memory alloys*, Journal of the mechanics and physics of solids **61**, 2522 (2013).

6

CONCLUSIONS

Every science has a beginning but no end.

Anton Chekhov

THE objective of the thesis was to perform MD simulations of equi-atomic NiTi systems and obtain their thermo-mechanical behavior. During the course of the study, the necessity to build a reliable and robust interatomic potential was realized. To this end, a new reference-free MEAM potential has been developed for NiTi by optimizing the parameters to *ab initio* data, and its performance is better than existing potentials. Along with predicting accurate thermo-mechanical behavior along different orientations, the quality of the potential is also demonstrated by performing simulations on systems with point and line defects. Next, a chapter-wise summary of results and conclusions is provided.

The drawbacks of the EAM-Finnis-Sinclair potential, one of the earlier developed potentials for NiTi, were highlighted in Chapter 2. The 2NN-MEAM interatomic potential predicts more accurate values of lattice and elastic constants in comparison to experimental/*ab initio* data than the EAM potential. Hence, the transformation strain and the modulus of the austenitic and martensitic phases, which are functions of the lattice and elastic constants, are better captured by the MEAM potential. This was demonstrated by showing results of a uniaxial loading simulation along $\langle 100 \rangle_{B2}$ on a single-crystal bulk, which were then compared to a lattice deformation model. At this stage, it was concluded that the MEAM potential is the most suited potential for a study of pseudo-elasticity in NiTi, especially in poly-crystals with grains along different orientations.

In Chapter 3 the predictive power of the 2NN-MEAM was highlighted by showing MD simulation results of the orientation-dependent martensitic transformation in single-crystal NiTi nano-wires during normal loading and bending. The transformation strain varies along different loading directions, since a different final variant of martensite is formed at the end of the transformation. Loading along $\langle 111 \rangle_{B2}$ showed the highest transformation strain in tension out of the three orientations chosen for the study. Similarly, loading along $\langle 110 \rangle_{B2}$ and $\langle 100 \rangle_{B2}$ showed the highest transformation strain in compression. Besides stress-strain behavior, there is also a difference in the martensitic phase transformation mechanism based on the orientation, with some orientations transforming through the formation of Lüders-like bands whereas some orientations preferring the formation of a multi-variant martensite followed by reorientation to a single variant. The orientation dependence and tension-compression asymmetry affects the transformation in differently sized and shaped NiTi systems with different boundary conditions. This was demonstrated by comparing the difference in curvature upon bending of three differently oriented nano-wires.

The need to build an even more robust potential was considered in Chapter 4. The 2NN-MEAM lacks predictive capabilities because it estimates inaccurate transformation temperatures and martensitic elastic constants in comparison to experiments. A reference-free version of the MEAM potential provides an opportunity to fit to an even broader dataset by virtue of its reference-free formalism of the pair potential term. The methodology was described in Chapter 4 where a new parametrization of the RF-MEAM for NiTi was developed by also fitting to stress tensors of configurations in addition to energies and atomic forces. The RF-MEAM predicts thermo-mechanical properties in closer agreement to experiments in comparison to existing potentials. The methodology was also extended and results compared for a four-component NbMoTaW high entropy alloy. The methodology provides a way to build accurate potentials for complex systems with large fitting datasets. The fitting code is also compatible with MD packages which makes it convenient to build models and perform MD simulations for such systems.

The predicted value of the austenitic transformation temperature by using the RF-MEAM potential in single-crystal NiTi bulk is approximately 80 K higher than the experimentally known value. The reason was attributed, in Chapter 4, to the presence of small defects in the experimental specimens whereas MD runs were performed on ideal defect-free single crystals. To verify this, the effect of various defects on the phase transformation behavior was investigated in Chapter 5. The austenitic transformation temperature reduces drastically due to the presence of various defects in the system, bringing the value much closer to the experimental one. Presence of anti-sites and vacancies in the system create local inhibitions to the martensitic transformation during cooling. Excessive Ni content reduces both the transformation temperatures and this trend is compared and validated with experimental results. Grain boundaries in crystals and free surfaces in NiTi nano-wires act as a nucleation site for the austenitic transformation, thereby initiating it at a much lower temperature.

The validity of an interatomic potential for a particular system under certain boundary conditions is very crucial before performing any analysis. Once the applicability of a potential is exhibited, the predictive powers of MD simulations using that particular potential can be used to optimize and fine-tune the manufacturing and production of devices for different applications. In this thesis, a new RF-MEAM potential is developed and tested for NiTi, the capabilities of which can be exploited in the future.

6.1. OUTLOOK

This thesis discussed two main topics: interatomic potential fitting and MD simulations. With a continual increase in computing power, the scope for both these topics is vast.

Firstly, more accurate interatomic potentials can be fit for various systems by broadening the database for fitting. Potentials can be tailored for a particular phase space focusing more on accuracy rather than robustness. Similarly, interatomic potentials can also be fit for highly complex multi-component systems with several fitting parameters. In either case, extensive computing power enables access to a highly complex phase space with several local minima and helps in efficiently navigating through this to reach a satisfactory point (parameter set) that would best describe the material for a particular application. Different potential formalisms have their own merits and demerits. Analytical forms of the energy as a function of interatomic distance as in the case of EAMs and MEAMs, although robust and amenable to optimization for small systems, do not describe the exact physics (e.g., bond formation and breaking). Another form of potentials, the bond order potentials (BOPs), are derived from *ab initio* equations that describes the physics, but these are limited in terms of the database that can be used for fitting and the complexity of the fit. More recently, several machine learning based interatomic potentials have been developed where basis functions are defined based on atomic environments present in the fitting database. These potentials can capture a large part of the phase space accurately and efficiently, thereby enabling its usage to even several multi-component systems. Through active learning, configurations that the potentials are not familiar with can be learnt on the fly hence improving their robustness. Choosing an interatomic potential for a study hinges on several factors: the robustness that is needed, the complexity of the system, time taken for fitting, and eventually time taken to perform MD runs using the fitted potential.

Once the right interatomic potential is chosen for a study, large-scale MD runs can be performed with relatively affordable computing resources. MD simulations of poly-crystals of the order of hundreds of nanometers, simulations of accurate dislocation motion with crystals, high temperature simulations of large-sized multi-component systems etc. can be performed to understand the material behavior in more detail. Large-scale simulation results can also be used for obtaining parameters for a meso-scale model, facilitating the multi-scale modeling of any system. With respect to the equi-atomic NiTi system, MD runs can be performed for further investigation of the effect of various GBs and dislocation motion, twin formation and twin boundary effects on the phase transformation,

effect of precipitates on the physical and transformation properties etc. Since the RF-MEAM potential (and the 2NN-MEAM potential) is applicable across various orientations to predict transformation behavior, MD simulation results on NiTi nano-wires can be used to develop stress-temperature-size phase diagrams. Based on this, constitutive models for NiTi nano-wires can be parametrized and used for the meso-scale modeling of much larger NiTi systems.

ACKNOWLEDGEMENTS

This thesis, and my PhD, would not have been possible without the guidance, help and support of a lot of people. Firstly, I would like to thank Angelo and Lucia, my two supervisors, for their support, critical analysis and perfectionism. They provided me with a lot of freedom with regards to my project for which I am thankful. I would like to thank Bert, my promoter, and Barend for introducing me to molecular dynamics. I am also grateful to Peter Klaver, who, along with Barend, taught me the basics of MD and LAMMPS, which eventually became the core of my work. My thanks also goes out to Marcel and Andy who were involved in the later part of my PhD, for their collaboration, insights and knowledge sharing. The PhD topic wouldn't have reached a satisfying conclusion without their assistance. This project would not have been possible without the funding provided by Shell and FOM/NWO and I would like to thank all people involved in the construction and development of the FOM-Shell PhD75 program for hiring, funding, assisting and supporting me during the course of my PhD. For the last year or so, I have been working as a researcher in the 3ME department, in close collaboration with the Max Planck Institute in Dusseldorf. I have gained valuable knowledge during this time, and it has also helped to further tune my results that I have obtained towards the end of my PhD and for this, I am grateful to Fritz. A special thanks also to Anneke, Annette and Maria, who helped me before and during my move to the Netherlands, eased my arrival considerably and assisted with all the non-technical aspects and paper work associated with the university.

My years in the Netherlands have been the best years of my life so far and it wouldn't have been the same without mentioning these friends, colleagues and comrades; Ashwath, Wilco, Siddharth and Danilo for all the good times - Delft wouldn't have been the same otherwise; Erik, Kai and Marcelo, for all the conversations over coffee and being my first office mates; other colleagues in Civil including Wouter, Luiz, Mohsen, Fariborz, YaoLu, Anupam, Mani, Tao, Liting, Mehdi, Richard, Lu, Dongyu, Tiziano, Adriaan, Davide, Ali, Jafar, MZ, Sanaz, Osvalds, Behrouz, Jaap, Rafit, Frank, Frans, and others that I might have missed; colleagues in 3ME - Casper, Kelvin, RJ, Astrid, Neha, Mohsen, Nilgoon, Ann-sophie, Alexandra, Biswanath, Poulumi, Mathias, Jan, Sorosh, Farnaz, Geeske and others that I might have missed; Locus people - Walter, Vikram, Adarsha, Nico, Jim,

Tjarky and the list goes on; Concordia, where I played cricket for 3 seasons - Sid, Charan, Tiggy, Menon, Shukla, Manu Bhai, Aggu, Reddy, Adi, Hari and other Concordians for your passion for the game; Chilli and Pottan for the social networking, and JP, Dhev, Psych, Seef, and other insti junta; KS, Sudha, Daga, Shreya, Dericae, Ajay, Khaba, Sindu, Padaf, Deb, Akshay and a bunch of aforementioned and unmentioned people with whom I travelled and explored Europe over the last 5 years; Attila, Tob, Kerim, Sai, Piero, and all the others that I have missed out - a big thank you. My sincere apologies if I have missed anyone here. I have met a lot of interesting people from different walks of life over the last 5 years in the Netherlands and Europe in general, through travelling, hiking, going to conferences etc., all of whom have directly or indirectly affected me in some small way or the other, and all of which wouldn't have been possible without my pursuit for a PhD.

Last but not the least, I would like to thank Amma and Appa, for all the support, encouragement and toleration. The thesis is an outcome of 5 years of research in TU Delft, and hence my final thanks goes to the TU and to the city of Delft, my second home.

CURRICULUM VITÆ

Prashanth SRINIVASAN

08-08-1991 Born in Chennai, India.

EDUCATION

1998–2008 Senior Secondary School
D.A.V Mogappair, Chennai

2008–2013 B. Tech in Civil Engineering and M. Tech in Applied Mechanics
Indian Institute of Technology, Madras
Thesis: Large Deflections of Shape Memory Alloys: 3D
Wire Forms Analysis

2013-2018 PhD. in Civil Engineering
Delft University of Technology
Thesis: Atomistic Simulations of Nickel-Titanium
Shape Memory Alloys

LIST OF PUBLICATIONS

5. **P. Srinivasan, A.I. Duff, M.H.F. Sluiter, L. Nicola, A. Simone**, *Effect of defects on phase transformations in NiTi studied using molecular dynamics simulations*, in preparation.
4. **P. Srinivasan, A.I. Duff, T. Mellan, M.H.F. Sluiter, L. Nicola, A. Simone**, *The effectiveness of reference-free modified embedded atom method potentials demonstrated for NiTi and NbMoTaW*, *Modelling and Simulation in Materials Science and Engineering* **27**, 6 (2019).
3. **P. Srinivasan, L. Nicola, A. Simone**, *Atomistic modeling of the orientation dependent pseudo-elasticity in NiTi: normal loading and bending*, *Computational Materials Science* **154**, 25-36 (2018).
2. **P. Srinivasan, L. Nicola, A. Simone**, *Modeling pseudo-elasticity in NiTi: Why the MEAM potential outperforms the EAM-FS potential*, *Computational Materials Science* **134**, 145-152 (2017).
1. **P. Srinivasan, L. Nicola, B.J. Thijsse, A. Simone**, *Molecular dynamics simulations of the two-way shape-memory effect in NiTi nanowires*, *MRS Symposium Proceedings* **1782**, 35-40 (2015).